STUDIES OF SPECTRAL AND SPATIAL ENERGY TRANSFER IN SOLIDS

By

CHRISTOPHER MARK LAWSON

Bachelor of Science
Oklahoma State University
Stillwater, Oklahoma
1976

Master of Science
University of Colorado
Boulder, Colorado
1979

Submitted to the Faculty of the Graduate College
of the Oklahoma State University
in partial fulfillment of the requirements
for the degree of
DOCTOR OF PHILOSOPHY
December, 1981

STUDIES OF SPECTRAL AND SPATIAL ENERGY

TRANSFER IN SOLIDS

Thesis Approved:

Richard C. Bowell
Thesis Adviser

Larry E. Hallibuton

Paul Westhaus

James R. Chiake

Norman N Durham
Dean of the Graduate College

ACKNOWLEDGMENTS

The author wishes to express his gratitude to his thesis adviser, Dr. R. C. Powell for his help and guidance throughout this work. Special thanks and appreciation are also extended to the other Graduate Committee members, Dr. P. A. Westhaus, Dr. L. E. Halliburton, and Dr. J. Choike, for their kind cooperation. Finally, the financial support from the Department of Physics, Oklahoma State University and the U.S. Army Research Office have been appreciated.

TABLE OF CONTENTS

LIST OF TABLES

LIST OF FIGURES

CHAPTER I

INTRODUCTION

In the last few years, laser spectroscopy has been an important tool in the study of the transfer of electronic excitation energy between molecules in a solid. Characterizing energy transfer is particularly important in materials with potential laser applications. Energy transfer can enhance laser performance by increasing the pumping efficiency of the active ions, but energy transfer can also decrease the laser efficiency through concentration quenching mechanisms. Characterizing energy transfer is therefore critically important in developing efficient laser materials.

Techniques

Two important techniques for studying energy transfer in potential laser materials are site-selection spectroscopy and degenerate four wave mixing spectroscopy.

Site selection spectroscopy is a method of studying spectral energy transfer between the active ions in a laser medium. A high resolution tunable dye laser is used to selectively excite impurity atoms in different crystallographic field sites so their transitions can be spectrally resolved. By taking spectral scans of the fluorescence emission at different times after the laser excitation pulse, one can characterize the time dependence of the energy transfer.

Degenerate four wave mixing spectroscopy is a very recent technique

for studying spatial energy migration without spectral transfer of energy.

Degenerate four wave mixing spectroscopy (which studies spatial energy migration) thus compliments site selection spectroscopy (which studies spectral energy transfer) very well. In degenerate four wave mixing spectroscopy, one uses two strong pump beams to "write" a holographic grating in a medium, and a weaker probe beam to "read" this grating. By studying the time evolution of the grating decay, one can obtain important information about spatial energy migration.

Summary of Thesis

The second chapter of this thesis will describe theoretical and numerical work in providing models of energy transfer that better characterize previous sets of data. In the first part of Chapter II, three examples are given of previously published data that have been interpreted using the Yokota-Tanimoto theory: (i) $Tb_3Al_5O_{14}$, (ii) Anthracene in Fluorene, (iii) $Y_{.84}Yb_{.1}Ho_{.06}F_3$. In each case it is shown the Yokota-Tanimoto theory is not valid for the relevant system, and the system is instead described using a more applicable theory. The $Y_{.84}Yb_{.1}Ho_{.06}F_3$ data is characterized using the Chow-Powell theory, the Anthracene in Fluorene data is characterized using the Soos-Powell theory, and the $Tb_3Al_5O_{14}$ data is characterized using the Burshtein theory.

In the second part of Chapter II, the problem of characterizing energy migration among a random distribution of sensitizers is addressed. Most existing energy transfer theories assume a uniform background lattice of sensitizers. This is a bad approximation if the sensitizer ions are a low concentration impurity in the host lattice, such as

$Y_3Ga_5O_{12}:Nd^{3+}$(.25%) or $YVO_4:Nd^{3+}$(3%). These two systems are modeled using a numerical Monte-Carlo approach, and the results are compared to a more standard Burshtein model which assumes a uniform distribution of sensitizers.

Chapter III describes the use of site selection spectroscopy to study spectral energy transfer in $LiNbO_3:Eu^{3+}$. A non-linear least square fit of the time dependence of the energy transfer is then performed to obtain information about the mechanisms of energy transfer in this system.

Chapter IV describes the use of four wave mixing spectroscopy to study spatial energy migration in $Nd_xLa_{1-x}P_5O_{14}$; where x = 0.01, x = 0.1, x = 0.2, x = 0.6, and x = 1.0. Long range energy migration is observed, and the mechanisms of concentration quenching in these materials are examined. Also, the scattering efficiency of the four wave mixing process is derived for the configuration usually used for energy migration studies by modeling the system as a two-level system. Finally, effects arising from a phase mismatch of the pump beams are theoretically characterized.

CHAPTER II

SYNOPSIS OF ENERGY TRANSFER MODELS

Whenever a material is exposed to light, energy may be absorbed through the creation of electronic excited states. The atoms or active ions that absorb this energy are called "sensitizers". Later this energy may be emitted in the form of light or heat by atoms or active ions that are called "activators". The migration of energy from the sensitizers to the activators is called "energy transfer."

"Radiationless energy transfer" may be thought of as a quantum mechanical resonance process involving the exchange of a virtual photon. The transfer mechanism can either be an electromagnetic multipole-multipole interaction or an exchange interaction.

Sometimes the sensitizer in the excited state transfers energy directly to the activator which is called "direct" or "single step" resonant energy transfer. Other times the energy migrates many times between sensitizers before transfer to an activator occurs which is called "multistep" energy transfer.

Single Step Energy Transfer

Whenever the sensitizer concentration is very low or whenever the sensitizer-activator interaction is much stronger than the sensitizer-sensitizer interaction, the energy transfer will be dominated by single step energy transfer. The theory of single step energy transfer was developed by Förster (1) and Dexter (2). Whenever the mechanism of

energy transfer is a multipole-multipole interaction, the energy transfer rate ω_{sa} is given by (1), (2)

$$\omega_{sa} = (\tau_s^o)^{-1} \left(\frac{R_o}{R_{sa}}\right)^m \qquad \text{(II-1)}$$

where τ_s^o is the intrinsic lifetime of the sensitizer, R_{sa} is the sensitizer-activator separation, and R_o is the critical interaction distance which is the sensitizer-activator separation at which the energy transfer rate is equal to the intrinsic decay rate. The power m is equal to 6 for electric dipole-dipole interaction, m = 8 for electric dipole-quadrapole interaction, and m = 10 for electric quadrapole-quadrapole interaction.

For a multipole-multipole interaction, the density of excited sensitizers varies as (1), (2)

$$n_s(t) = n_s(o)\exp\{-\frac{t}{\tau_s^o} - \Gamma(1 - 3/m)\left(\frac{N_a}{C_o}\right)\left(\frac{t}{\tau_s^o}\right)^{3/m}\} \qquad \text{(II-2)}$$

where N_a is the activator concentration and C_o is the critical concentration given as

$$C_o = \left(\frac{4}{3}\pi R_o^3\right)^{-1} .$$

If one assumes hydrogen-like wavefunctions, the energy transfer rate for an exchange interaction is given by (2), (3)

$$\omega_{sa} = (\tau_s^o)^{-1} \exp\{\delta[1 - \frac{R_{sa}}{R_o}]\} \qquad \text{(II-3)}$$

where $\delta = 2R_o/L$ and L is an effective Bohr radius. The density of excited sensitizers for an exchange interaction is given by (3)

$$n_s(t) = n_s(o)\ \exp\{-\frac{t}{\tau_o} - \delta^{-3}\ (\frac{N_a}{C_o})\, g(\ell^{\delta}\ \frac{t}{\tau_o})\} \qquad \text{(II-4)}$$

where

$$g(z) = -\,z \int_o^1 \exp(-zy)\,(\ln y)^3 dy\ .$$

Multistep Energy Transfer

Multistep energy transfer occurs whenever the excitation migrates several times among sensitizers before transfer to the activator. Both the sensitizer-sensitizer interaction and the sensitizer-activator interaction will be either a multipole-multipole interaction or an exchange interaction; although the sensitizer-sensitizer interaction may be different than the sensitizer-activator interaction. Thus characterizing multistep energy transfer involves both describing the sensitizer-sensitizer energy migration and describing the sensitizer-activator energy trapping. This problem can be approached either from a random walk model or a diffusion model (4,5,6,9).

In the random walk model, the excitation or "exciton" (7) is modeled as undergoing a random walk on a three-dimensional lattice of sensitizers before becoming trapped at an activator site. This random walk may be numerically simulated on a computer in a Monte Carlo simulation, as will be discussed later.

An approach developed by Burshtein (8) treated the transfer rate as a random variable in a stochastic hopping process. The density of excited sensitizers is then governed by the equation

$$n_s(t) = \overline{n_s}(t)\,\ell^{-t/t_o} + \frac{1}{t_o}\int_o^t n_s(t-t')\,\overline{n_s}(t')\,\ell^{-t'/t_o}\,dt' \qquad \text{(II-5)}$$

where t_o is the average hopping time and $\overline{n_s}(t)$ is given by Equations (II-2) or (II-4) depending on the interaction mechanism.

The other mathematical approaches for treating multistep energy transfer involve either a diffusion model or modifications of the diffusion model.

The simplest diffusion model is when one takes the sensitizer-activator interaction as equivalent to the sensitizer-sensitizer interaction. If one considers a uniform lattice of sensitizers, the energy transfer rate is given by (1,5,9)

$$\omega_{Diff} = 4\pi D R_t C_t \left(1 + \frac{R_T}{(\pi D t)^{1/2}}\right) \qquad \text{(II-6)}$$

where D is the diffusion coefficient, R_t is the trapping radius around an exciton trap, and C_t is the concentration of non-interacting traps.

The assumptions of the simple diffusion model often prove to be too restrictive to accurately describe the physical situation. The diffusion model has been extended in several theories to account for the trapping properties of the activator in several limiting cases.

Soos and Powell (10) extended diffusion theory to include the effects of trapping regions of various sizes and geometries. This theory is applicable whenever the energy migration is dominated by diffusion among sensitizers. Instead of treating the activators as point traps as simple diffusion theory does, the theory of Soos and Powell treats the trapping region as having a finite size and a geometry associated with it. The exciton is trapped at the activator site whenever it hops onto a distorted region around the activator. This theory is particularly important whenever the activator is much larger than the atom it replaces

causing distortion of the lattice. The energy transfer rate for a simple cubic lattice is given by

$$\omega_{sa}(t) = N_a V_m C\{A\} t_h^{-1} \left[1 + \frac{2C\{A\} V_m t^{-1/2}}{(4\pi D)^{3/2} t_h}\right] \qquad \text{(II-7)}$$

where N_a is the concentration of activator ions, V_m is the volume per molecule on the lattice of sensitizers, $C\{A\}$ is the "capacity" of the random walk which is the number of previously unsampled sites sampled by the exciton on each step of the random walk in the limit of many steps, and t_h is the hopping time among sensitizers.

Another way of accounting for the activator trapping properties is to add a term in the diffusion equation which explicitly takes into account the sensitizer-activator interaction. The diffusion equation then becomes

$$\frac{\partial n_s(\underset{\sim}{r},t)}{\partial t} = -\beta_s n_s(\underset{\sim}{r},t) + D\nabla^2 n_s(\underset{\sim}{r},t) - \sum_i \beta_s \left(\frac{R_o}{r_i}\right)^6 n_s(\underset{\sim}{r},t) \qquad \text{(II-8)}$$

where β_s is the sensitizer intrinsic decay rate and r_i is the separation for a given sensitizer-activator pair.

Yokota and Tanimoto (11) solved Equation (II-8) in the limiting case where the sensitizer-sensitizer interaction is small compared to the strong sensitizer-activator interaction to obtain

$$n_s(t) = n_s(o)\exp\{-\beta_s t - \frac{4}{3}\pi^{3/2} N_a R_o^3 (\beta_s t)^{1/2} \left[\frac{1+10.87x+15.50x^2}{1+8.74x}\right]^{3/4}\} \qquad \text{(II-9)}$$

where $x = D\,\beta_s^{-1/3} R_o^{-2} t^{2/3}$.

Chow and Powell (12) solved Equation (II-8) in the limiting case

where the sensitizer-sensitizer interaction is very large compared to the sensitizer-activator interaction to obtain

$$\omega_{sa}(t) = \omega_{diff}(t) + \frac{4\pi N_a \beta_s R_o^6}{3R_t} + 2\pi N_a R_t^2 \int_{R_t}^{\infty} \frac{\beta_s R_o^6}{r^6} \left[\operatorname{erfc}\left(\frac{r-R_t}{\sqrt{4Dt}}\right)\right]^2 dr$$

$$- 8\pi N_a \int_{R_t}^{\infty} \frac{\beta_s R_o^6}{r^5} \left[\operatorname{erfc}\left(\frac{r-R_t}{\sqrt{4Dt}}\right)\right] dr \qquad \text{(II-10)}$$

where $\omega_{diff}(t)$ is given by Equation (II-6).

Description of Energy Transfer Data Using Migration/Trapping Theories

The theory of Yokota and Tanimoto is a popular theory which is often used to describe data with characteristics such that the limiting assumptions of the Yokota-Tanimoto theory are not valid. In this section, three examples are given of data which have been interpreted using the Yokota-Tanimoto theory, which are more appropriately described by other energy transfer theories.

The limits of validity of the Yokota-Tanimoto theory can be obtained by assuming a uniform lattice of sensitizers so that Equation (II-8) becomes

$$N_s(t) = N_s(o)\ell^{-\beta_s t} \left\{\frac{1}{V}\int_o^{R_v} 4\pi r^2 \exp(tD\nabla_r^2 - \alpha r^{-6} t)\, dr\right\}^{N_a} \qquad \text{(II-11)}$$

where $N_s(t)$ is the total number of excited sensitizers at time t, N_a is the total number of activators, $\alpha = \beta_s R_o^6$, and

$$V = \frac{4}{3}\pi R_v^3$$

is the total volume of the sample.

Since ∇_r^2 and r^{-6} are Hermitian, we may expand the exponent as

$$\exp(tD\nabla_r^2 - \alpha r^{-6}t) = \exp(-\alpha r^{-6}t)\{1 + \sum_{n=1}^{\infty}(-1)^n \int_o^t dt_1 \cdots \int_o^{t_{n-1}} dt_n U(t_1)\cdots U(t_n)\}$$

where $U(t) = \ell^{\alpha t/r^6}(-D\nabla_r^2)\ell^{-t\alpha/r^6}$. Thus Equation (II-11) becomes (13)

$$N_s(t) = N_s(o)\exp\{-\beta_s t - \frac{4}{3}\pi^{3/2} N_a\sqrt{\alpha t}\,[1 + 2.5\,\pi^{-1/2}\,\Gamma(5/6)D\alpha^{-1/3}t^{2/3}$$

$$- 4.45\pi^{-1/2}\,\Gamma(13/6)D^2\alpha^{-2/3}t^{4/3} + 21.66D^3\alpha^{-1}t^2$$

$$- \frac{600}{\pi}\,\Gamma(\tfrac{11}{6})D^4\alpha^{-4/3}t^{8/3} + \cdots]\} \qquad \text{(II-12)}$$

where $N_a = N_a/V$.

The results of Yokota and Tanimota (11) are then obtained by keeping only the first four terms of the expansion from Equation (II-12) and using the (1,2) Padê approximation to obtain Equation (II-9). Notice, however, that neglecting the fifth term in (II-12) is valid only if the magnitude of the fifth term is small compared with the magnitude of the fourth term, which is the same as

$$14.7\ D\ \alpha^{-1/3}t^{2/3} < 1 \qquad \text{(II-13)}$$

which can be thought of as a validity check for the Yokota-Tanimota theory. Notice that (II-13) is a necessary but not sufficient condition for the Yokota-Tanimota theory to be valid. Equation (II-13) will be satisfied whenever the sensitizer-sensitizer interaction is small enough compared to the sensitizer-activator interaction.

As mentioned earlier, the solution to (II-8) in the opposite limit (sensitizer-activator interaction small compared to sensitizer-sensitizer interaction) was given by the Chow-Powell theory as Equation (II-10). This expression will be valid if the direct sensitizer-activator transfer is small compared to the sensitizer diffusion. This will be true if (12)

$$\frac{\pi D R_t^4}{\alpha} > 1 \qquad \text{where} \qquad \alpha = \beta_s R_o^6 \ .$$

YF_3:Yb,Ho

One example where energy transfer data has been interpreted using the Yokota-Tanimoto theory is YF_3:Yb,Ho (14). The luminescence intensity of the Yb^{3+} emission as a function of time at room temperature are as shown in Figure II-1. Fitting this data using Equation (II-9) gave the values (14)

$$D = 2.2 \times 10^{-11} \frac{cm^2}{sec} \text{ and } \alpha = 1.8 \times 10^{-41} \frac{cm^6}{sec} \ .$$

If these values for D and α are substituted into (II-13) along with a typical time of interest t = 200 μs, the validity parameter is given by $14.7\ D\ \alpha^{-1/3} t^{2/3} = 42.2$ which is much greater than one. Thus although the Yokota-Tanimoto theory gives a good fit to this system, the Yokota-Tanimoto model is not valid for this system.

However, when one fits this data using the Chow-Powell theory, one obtains

$$D = 3.96 \times 10^{-11} \frac{cm^2}{sec} \ , \ \alpha = 9.43 \times 10^{-42} \frac{cm^6}{sec} \ ,$$

and $R_t = 2.03\text{Å}$ which corresponds to the solid line shown in Figure II-1.

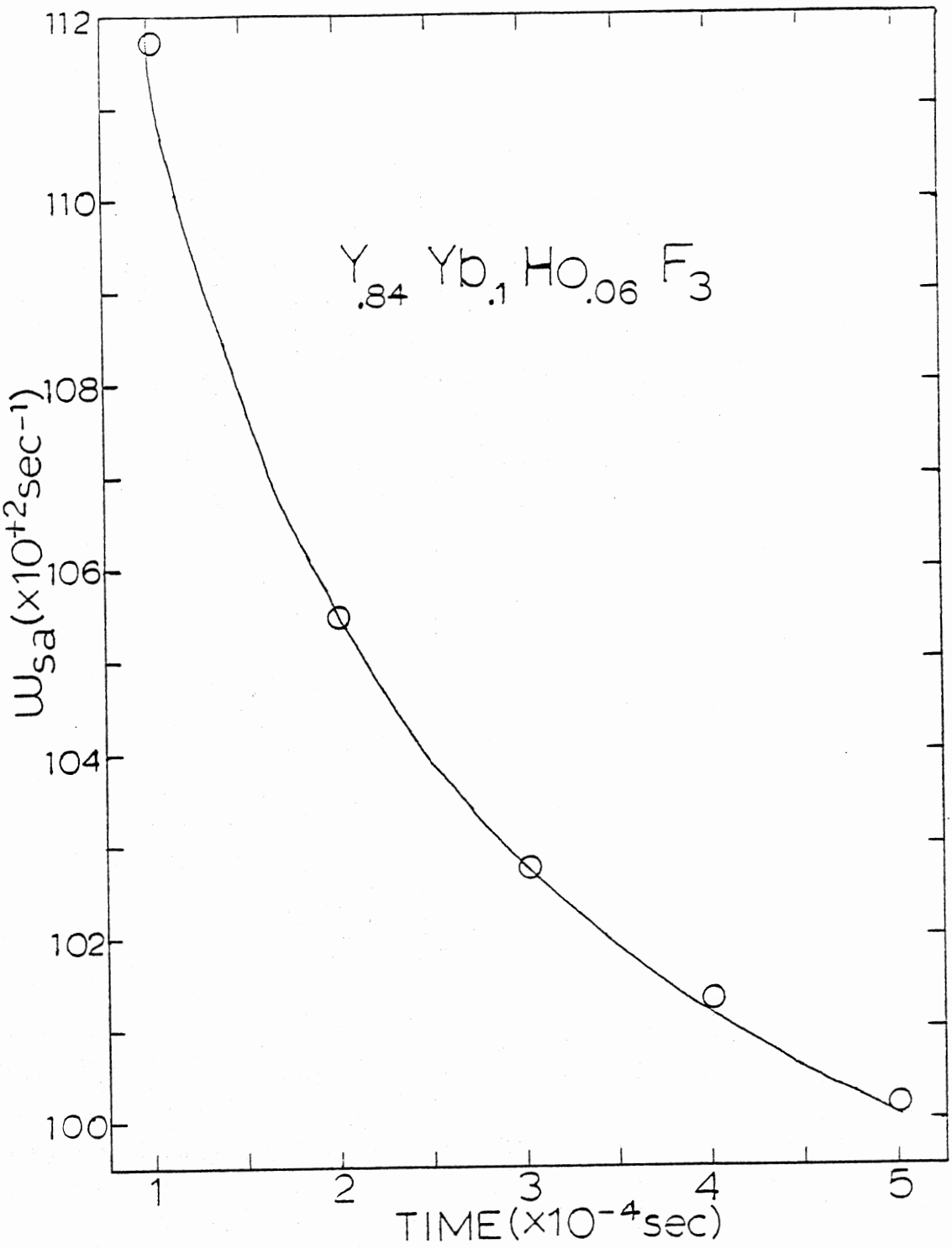

Figure II-1. Time Dependence of the Energy Transfer Rate in $Y_{.84}Yb_{.1}Ho_{.06}F_3$ at Room Temperature. Data From Reference (14) Shown as Circles; See Text for Explanation of Solid Line

One should note that the value for R_t was obtained from the non-linear least squares fit but is also consistent with the scattering length predicted in Ref. (14). These parameters may then be substituted in (II-14) to obtain the validity parameter

$$\frac{\pi D R_t^4}{\alpha} = 2.2$$

which is indeed greater than unity. Thus for this case it is the Chow-Powell theory which is the appropriate model for the system, and the Yokota-Tanimota model results in a factor of two error in the values for D and α.

Anthracene in Fluorene

A second system where the energy transfer has been interpreted using the Yokota-Tanimoto theory is Anthracene doped Fluorene crystals (15). The circles in Figure II-2 show the energy transfer rate from sensitizers to activators as a function of time. The concentration of activator ions is given by $N_a = 2.0 \times 10^{18}\ cm^{-3}$.

A good fit to the data was obtained using the Yokota-Tanimoto theory resulting in values of

$$\alpha = 1.74 \times 10^{-32}\ \frac{cm^6}{sec}, \qquad D = 4.5 \times 10^{-7}\ cm^2/sec.$$

One can then substitute into the Yokota-Tanimoto validity check Equation (II-13) with a typical time of interest t = 10ns to obtain $14.7\ D\alpha^{-1/3} t^{2/3} = 1.2$ showing that the Yokota-Tanimoto theory is not valid for this system.

When a nonlinear least squares fit of the Chow-Powell theory to this

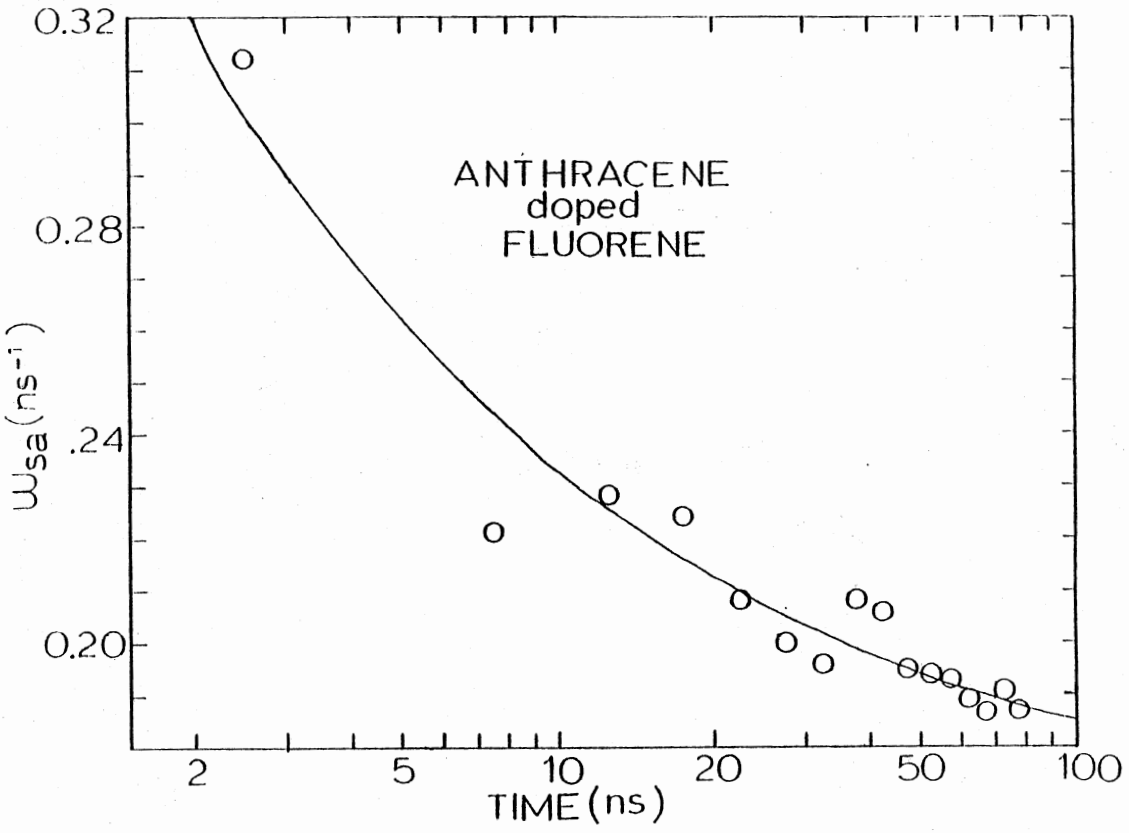

Figure II-2. Time Dependence of the Energy Transfer Rate in Anthracene Doped Fluorene at Room Temperature. Data From Reference (15) Shown as Circles; See Text for Explanation of Solid Line

data is performed, a good fit to the data is obtained with

$$\alpha = 5.28 \times 10^{-31} \frac{cm^6}{sec}, \quad D = 2.86 \times 10^{-3} \frac{cm^2}{sec},$$

and $R_t = 5.9\text{Å}$ which is close to the lattice parameter of the system. However, if these parameters are substituted into the Chow-Powell theory validity check Equation (II-14), $\pi D a^4 \alpha^{-1} = 0.21$ which indicates that the Chow-Powell theory is also not an appropriate way to model the system. Thus energy transfer in this system falls into the intermediate region where neither the sensitizer-sensitizer interaction nor the sensitizer-activator interaction are very small compared to the other.

The appropriate model for this system is the Soos-Powell model. Using the tabulated values for the capacity of trapping regions of various sizes and shapes (10), the data in Figure II-2 was fit using the Soos-Powell theory with values $t_h = 1.6 \times 10^{-9}$ sec and $C\{A\} = 1.5$ which gives $D = 6.5 \times 10^{-7}$ cm^2/sec. These parameters give a good fit to the data shown as the solid line in Figure II-2. The diffusion coefficient is comparable to but slightly larger than that obtained from the Yokota-Tanimoto theoretical fit. The value for the capacity implies a small trapping region as would be expected since the anthracene activator molecules are almost the same size and shape as the sensitizer fluorene host molecules they replace.

$\underline{Tb_3Al_5O_{12}}$

A third system where the energy transfer has been interpreted using the Yokota-Tanimoto theory is the fluorescence of Tb^{3+} ions in $Tb_3Al_5O_{12}$ crystals at 20.2K (16). With $N_a = 10^{19}$ cm^{-3}, a good fit to the data can be obtained from the Yokota-Tanimoto theory yielding values

$$D = 3.76 \times 10^{-10} \frac{cm^2}{sec} \text{ and } \alpha = 1.2 \times 10^{-35} \frac{cm^6}{sec}$$

which implies $R_o = 57\mathring{A}$. Substituting these parameters into the Yokota-Tanimoto validity check (II-13) with a typical time of interest t = 100 μs, yields $14.7\ D\alpha^{-1/3}t^{2/3} = 5.2$. Since this is larger than unity; this shows that although the Yokota-Tanimoto model yields a good fit to the data, it is not a valid way to model the system.

The Chow-Powell model is also not an appropriate way to model this system since it was impossible to obtain a good fit to the data using (II-10). Thus the energy transfer in this system also falls into the intermediate region where neither the sensitizer-sensitizer interaction nor the sensitizer-activator interaction are very small compared to the other.

It is difficult to interpret this data using the Soos-Powell theory because of the unknown nature of the activators.

The appropriate model for this system is the Burshtein model (8). Although no general analytical solution to (II-5) has been obtained, $n_s(t)$ can be obtained by numerical techniques. The i^{th} term $n_s(t_i)$ can be solved by using $n_s(t_{i-1})$ as the initial guess for $n_s(t_i)$ and then interating until convergence is obtained. The integrations we performed using Simpson's rule with Lagrangian interpolation. Because of the iterative process, this method is somewhat slower than the method suggested by Watts (17), but it gives better accuracy with the limited array sizes possible with the LSI-11 computer system used. Figure II-3 shows as shaded circles the sensitizer fluorescence intensity as a function of time, and the solid line is the best fit obtained from a numerical solution of II-5, yielding values

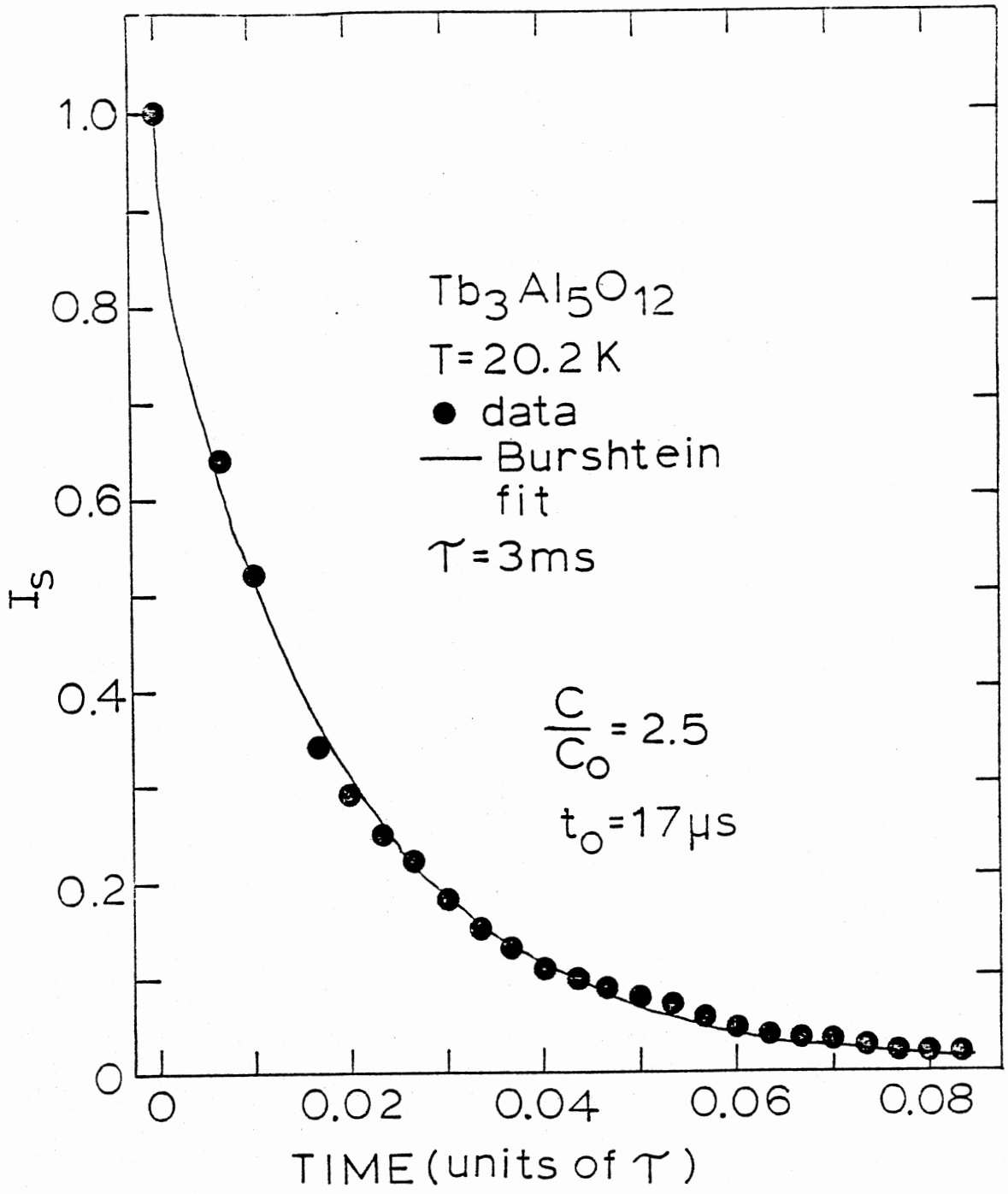

Figure II-3. Time Dependence of the Fluorescence Emission Intensity of $Tb_3Al_5O_{12}$ at 20.2 K. Data From Reference (16) Shown as Circles; See Text for Explanation of Solid Line

$$R_o = 39\text{Å} \text{ and } t_o = 1.71 \times 10^{-5} \text{ sec}$$

which implies $D = 6.6 \times 10^{-12}$ cm^2/sec. These values are significantly smaller than those obtained from the Yokota-Tanimoto fitting. The Burshtein value for R_o is more realistic than the value obtained from the Yokota-Tanimoto model.

Description of Energy Transfer Data Using Monte-Carlo Simulation

All of the analytic models of energy transfer mentioned in Section II-A assume a uniform lattice of sensitizers. One would expect this to be a reasonable approximation in some instances, for example if the sensitizers are part of the host lattice as in host-sensitized energy transfer. However, in other cases, such as whenever the sensitizers are a low concentration impurity in the host, one would expect the uniform lattice approximation to yield unsatisfactory theoretical predictions. It has not yet been possible to treat the problem of energy migration on a random lattice analytically, which has led to numerical approaches (12), (18).

Consider the case where the energy transfer is primarily diffusive with no direct sensitizer-activator interaction present except when the exciton hops onto an activator site. In the limit of many steps, this random walk of an exciton on a sensitizer lattice will become equivalent to a diffusive approach (6). If one neglects back transfer from the activator to the sensitizer, one can treat the energy migration on a random lattice with a Monte Carlo approach similar to that described in Reference (12), with the primary difference arising in the way that fluorescence decay is treated.

In this model, sensitizer excitons are generated, allowed to hop from site to site, and are destroyed when they hop onto an activator site.

The Monte Carlo simulation was implemented as a FORTRAN program running on a LSI-11 computer. As in any Monte Carlo algorithm, the "randomness" of the random number generator is critical. The random number distribution with the most desirable characteristics was produced by a Marsaglia composite type algorithm (19). This algorithm received the standard FORTRAN random number generator as one input and a circular shift register output as another input to produce as an output a "considerably more random" sequence. This algorithm performed satisfactorily with the 5000 excitons used in the Monte Carlo simulation.

The random nature of the lattice is accounted for by using the configuration-averaged distribution of hopping times. To generate this distribution, one takes the uniform distribution of random numbers obtained from the algorithm described above and weights it according to a Hertzian distribution which describes the occupancy of nearest neighbors in a random distribution of available sites in three dimensions (6). The resulting weighted distribution is then weighted a second time with a $(\frac{R_o}{r})^6$ dependence to reflect the variation of energy transfer rate with distance r for electric dipole-dipole interactions.

At each step in the exciton random walk, a number from the doubly weighted distribution described above is randomly chosen as the time for the next hop. One should note that this method allows for the possibility of transferring to any other sensitizer site in the lattice, unlike other numerical methods which often assume nearest neighbor interactions. After the hopping time is generated for a given step in the

random walk, a test is performed to check to see if the exciton has decayed by fluorescence emission during that time. This is done by comparing a uniformly distributed random number to the probability of fluorescence decay over the time interval given by the hopping time. If the exciton has not decayed by fluorescence emission during the time required for a given hop, another test is performed to determine if the exciton has hopped onto and thus been trapped at an activator site. This is done by comparing a uniformly distributed random number to the fractional occupancy of lattice sites by activators. Finally, one counts up the total number of excitons alive at each time t, which will be proportional to the intensity of the sensitizer fluorescence emission.

Interpretation of Energy Transfer in $Y_3Ga_5O_{12}:Nd^{3+}$ (.25%) and $YVO_4:Nd^{3+}$ (3%)

Two examples of systems where energy migrates on a random lattice is the energy migration among Nd^{3+} ions in $Y_3Ga_5O_{12}$ (garnet) and YVO_4 (vandate) host crystals at $100^{o}K$ after excitation by nitrogen laser-pumped dye laser (21,22).

This is site selection spectroscopy data where both the activators and the sensitizers are the Nd^{3+} ion in slightly different crystallographic field sites. It has been shown that the radiative and fluorescence decay rates are the same for both the sensitizer and the activator, and no back transfer from the activator to the sensitizer occurs (20,21). The time evolution of the density of excited states of the sensitizer $n_s(t)$ and the activator $n_a(t)$ are given by the rate equations

$$\dot{n}_s(t) = W_s - \beta\, n_s(t) - \omega_{sa}\, n_s(t) \qquad \text{(II-15)}$$

$$\dot{n}_a(t) = W_a - \beta\, n_a(t) + \omega_{sa}\, n_a(t) \qquad \text{(II-16)}$$

where W_s and W_a are the direct pumping rates of the sensitizer and activator level respectively, β is the intrinsic decay rate (assumed to be the same for the sensitizers and activators), and ω_{sa} is the energy transfer rate. The fluorescence intensities of the activator and sensitizer transitions $I_a(t)$ and $I_s(t)$ will be given by

$$I_a(t) = \beta\, n_a(t) \text{ and}$$

$$I_s(t) = \beta\, n_s(t) \ .$$

One can then solve the rate equations for the ratio of the intensities of the activator and sensitizer emission after a delta-function excitation pulse to obtain

$$\frac{I_a}{I_s}(t) = \left\{ \frac{\frac{n_a(o)}{n_s(o)} + 1}{N(t)} \right\} \ell^{-\beta t} - 1$$

where $N(t)$ is the normalized number of excitons alive at time t (i.e., $N(o) = 1$).

The ratios of the integrated fluorescence intensities of the activator to sensitizer transitions are plotted as solid lines in Figure II-4. The Monte Carlo program outputs the normalized number of excitons alive at a given time $N(t)$, so one can treat R_o and $\frac{n_a(o)}{n_s(o)}$ as adjustable fitting parameters and use Equation (II-17) to fit the data shown in Figure II-4.

The best fit for the garnet host was obtained with values $R_o = 21\text{Å}$ and $\frac{n_a(o)}{n_s(o)} = 0.059$ and is shown as solid circles in Figure II-4.

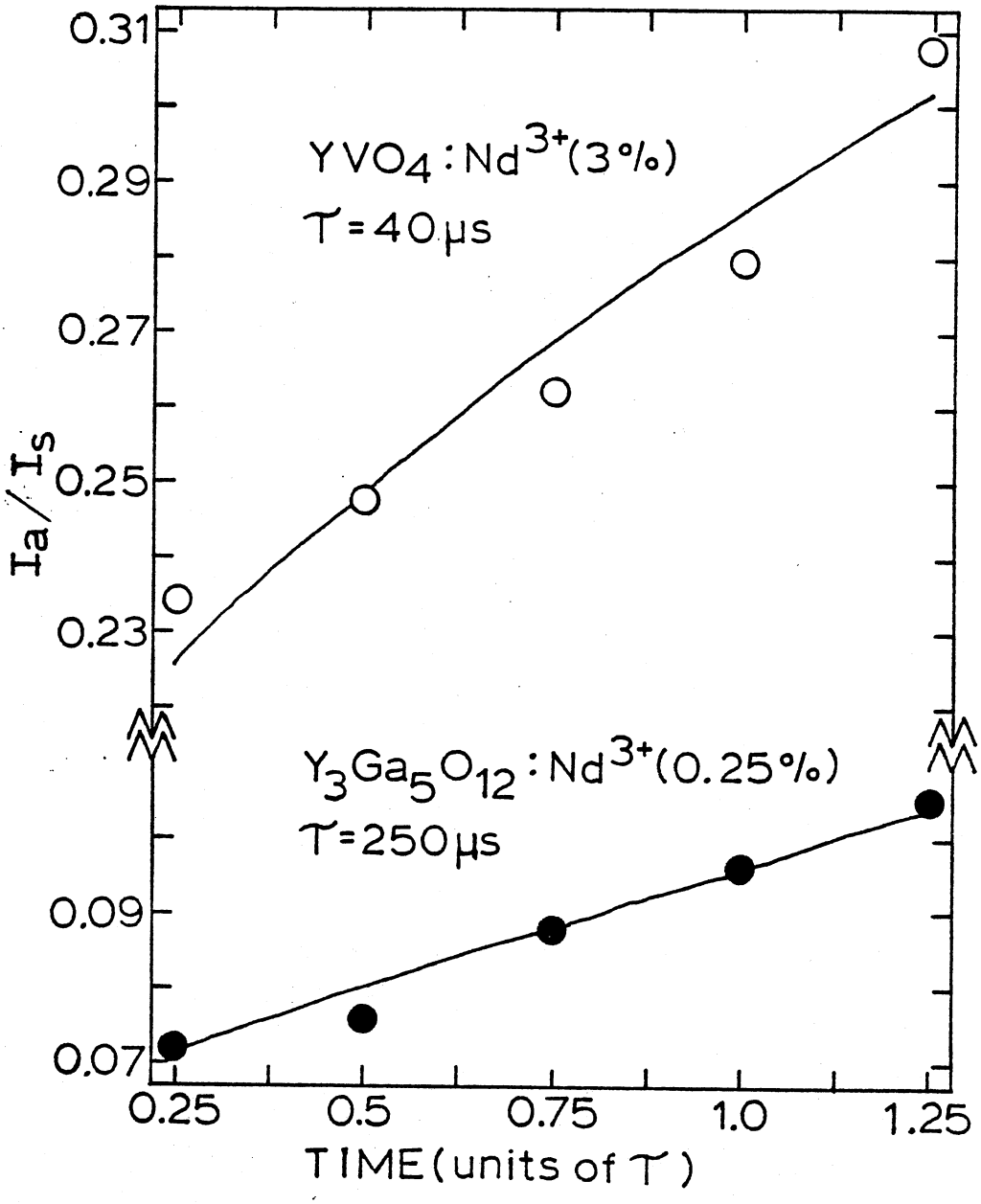

Figure II-4. Time Dependence of the Ratios of the Fluorescence Intensities of Emission from Nd^{3+} Sensitizer and Activator Ions in YVO_4 and $Y_3Ga_5O_{12}$ Crystals at 100 K. Solid Lines Represent the Data From References (20) and (21); the Circles Represent the Monte Carlo Fits to the Data.

The best fit for the vanadate host was obtained with values $R_o = 14\text{Å}$ and $\frac{n_a(o)}{n_s(o)} = 0.202$ and is shown as empty circles in Figure II-4.

The theoretical fit to the data is extremely sensitive to the fitting parameter R_o, and changes in R_o of more than 0.5 angstrom result in a grossly different theoretical curve.

The average exciton hopping time t_o can be calculated from the Monte Carlo results, and it is found to be $t_o = 160$ μs for the garnet host and $t_o = 2.1$ μs for the vanadate host.

It is now important to assess how the randomness of the lattice affects the theoretical predictions. To this end, the above results obtained from the Monte Carlo simulation must be compared to the results obtained from a theory that assumes a uniform lattice of sensitizers.

The appropriate theory is the Burshtein theory assuming dipole-dipole interactions and with the assumption that the sensitizer-sensitizer interaction strength reflected by the average hopping time t_o is the same as the sensitizer-activator interaction strength reflected by R_o.

Since $N(t) = n_s(t)/n_s(o)$, one can numerically solve Equation (II-5) as was described earlier and then use Equation (II-17) to fit the data shown in Figure II-4, where t_o and $\frac{n_a(o)}{n_s(o)}$ are the adjustable fitting parameters.

For the garnet crystal, the best fit was obtained with $n_a(o)/n_s(o) = 0.05$ and $t_o = 7760$ μs which implies a value of $R_o = 11\text{Å}$. For the vanadate data, the best fit was obtained with $\frac{n_a(o)}{n_s(o)} = 0.16$ and $t_o = 133$ μs which gives $R_o = 7\text{Å}$. In both samples, the values for t_o and R_o obtained by fitting the data using the Burshtein theory are significantly smaller than those obtained by fitting the data to a Monte Carlo model. This

implies that to accurately describe these data sets, the Monte Carlo model must assume much stronger interactions than the Burshtein model does.

The reason for the difference in the interaction strength required by the two contrasting models is that the Burshtein theory assumes a uniform lattice of sensitizers, while the Monte Carlo model explicitly takes into account the randomness of the lattice.

Since the Monte Carlo model requires stronger interactions to describe the data than the Burshtein model does, for a given interaction strength the energy transfer from sensitizers to activators predicted by the Burshtein model is much faster than that predicted by the Monte-Carlo model.

To understand the reason for this, one must remember that the excitons must migrate many times among the sensitizers before being trapped at the activator sites. In a uniform lattice of sensitizers, the distance to the nearest sensitizer and thus the hopping time for that step is always the same. In a random lattice, sometimes the nearest sensitizer is closer than it would be in a uniform lattice, and sometimes it is farther away than it would be in a uniform lattice. Whenever the sensitizer is closer than it would be in a uniform lattice, the energy transfer rate (to activators) is not significantly affected since that exciton would have probably made that hop anyway. However, if the nearest sensitizer is farther away than it would be on a uniform lattice, the hopping time which is proportional to $\alpha(R_o/r)^6$ may become very large, and the exciton may become effectively "bottlenecked" at that site, significantly decreasing the transfer rate to activators.

Thus for a given interaction and for a given density of activators N_a, the energy transfer rate predicted by the Monte Carlo model (explicitly taking into account the randomness of the lattice) will be much

smaller than the energy transfer rate predicted by the Burshtein theory (which assumes a uniform lattice). This explains why the values for R_o are larger when the data is interpreted using the Monte Carlo model than they are when the data is interpreted using the Burshtein theory.

CHAPTER III

SITE SELECTION SPECTROSCOPY IN $LiNbO_3:Eu^{3+}$

Experimental Technique and Samples

Site selection spectroscopy is a method of studying spectral energy transfer between the active ions in a crystal. A high resolution tunable dye laser is used to selectively excite impurity ions in slightly different crystallographic field sites so that their transitions can be spectrally resolved. By taking spectral scans of the fluorescence emission at different times after the laser excitation pulse, one can characterize the time dependence of the energy transfer.

The experimental apparatus involved is as shown in Figure III-1. The laser emission from a nitrogen laser pumped tunable dye laser is focused onto the sample which is housed in a refrigeration device. The fluorescence emission of the laser-excited sample is then spectrally resolved through a spectrometer and is then directed onto a photomultiplier tube. One can then obtain the spectra at any time after the laser excitation pulse by using a boxcar integrator and recorder.

The sample studied was a good optical quality single crystal of $LiNbO_3$ doped with 3.7×10^{19} cm^{-3} Eu^{3+} ions. The Eu^{3+} ion can enter the lattice substitionally for either the Li^{+} or Nb^{3+} ions. The method of required charge compensation is not known. Laser time-resolved spectroscopy studies of host-sensitized energy transfer in this crystal are described in Ref. (23). As mentioned in Ref. (23), small amounts of Cr^{3+} impurity ions were found in this crystal, but the Cr^{3+} impurity is not

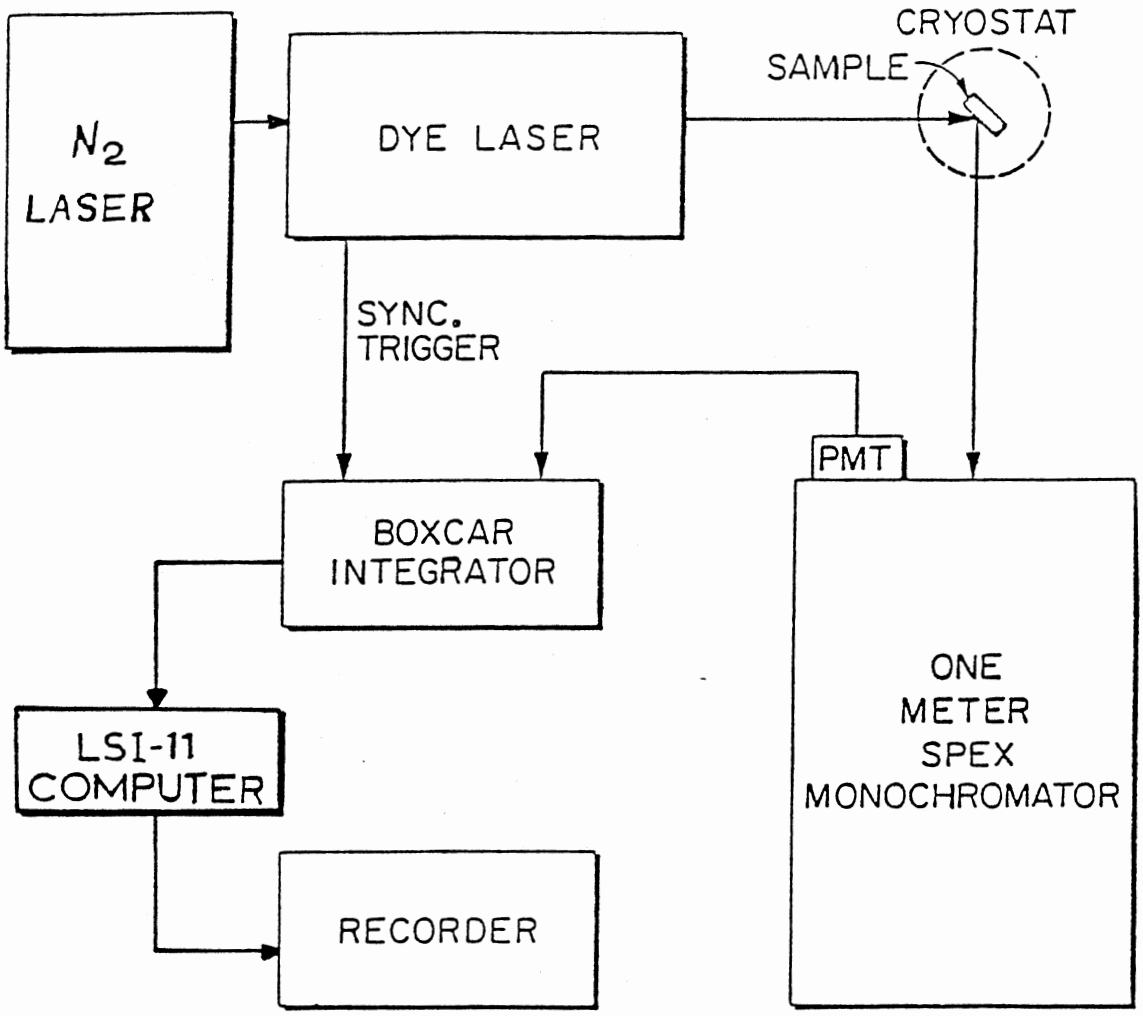

Figure III-1. Time Resolved Spectroscopy Apparatus

thought to play an important role in the site selection spectroscopy experiments described in this chapter since the energy transfer is between Eu^{3+} transitions.

Data

Site selection spectroscopy was used to study spectral energy transfer between transitions of the Eu^{3+} ion in slightly different crystallographic field sites in $LiNbO_3:Eu^{3+}$.

Figure III-2 shows the fluorescence spectrum of the directly pumped Eu^{3+} emission at $9^{o}K$ at short and long times after excitation pulse. The peaks on the left ($^5D_1$ and $^5D_2$ transitions) tend to die away with time and the peaks on the right (^5D_o transitions) grow in. The excitation wavelength is 4665Å, so the initial pumping is above the $^5D_2$ level.

The radiationless relaxation time from the $^5D_2$ levels to the lower $^5D_1$ and ^5D_o levels is very slow, and can be estimated as approximately equal to the rise time of the $^5D_1$ transitions which is about 9.4 μs.

The radiationless relaxation time from the $^5D_2$ and $^5D_1$ levels to the ^5D_o levels (this is probably dominated by relaxation from the $^5D_1$ levels) is also very slow, and can be estimated as approximately equal to the rise time of the ^5D_o transitions which is about 27.0 μs.

Using properties such as the rise and decay time of each line and the relative position of each line, one can identify the observed transitions and list them as shown in Table III-1. Using this information, one can then construct an energy level diagram as shown in Figure III-3. The energy levels are obtained from the observed lines. The energy values are given relative to the ^7F_o level, which are obtained indirectly from the $^5D_1 - {}^7F_o$ reference line.

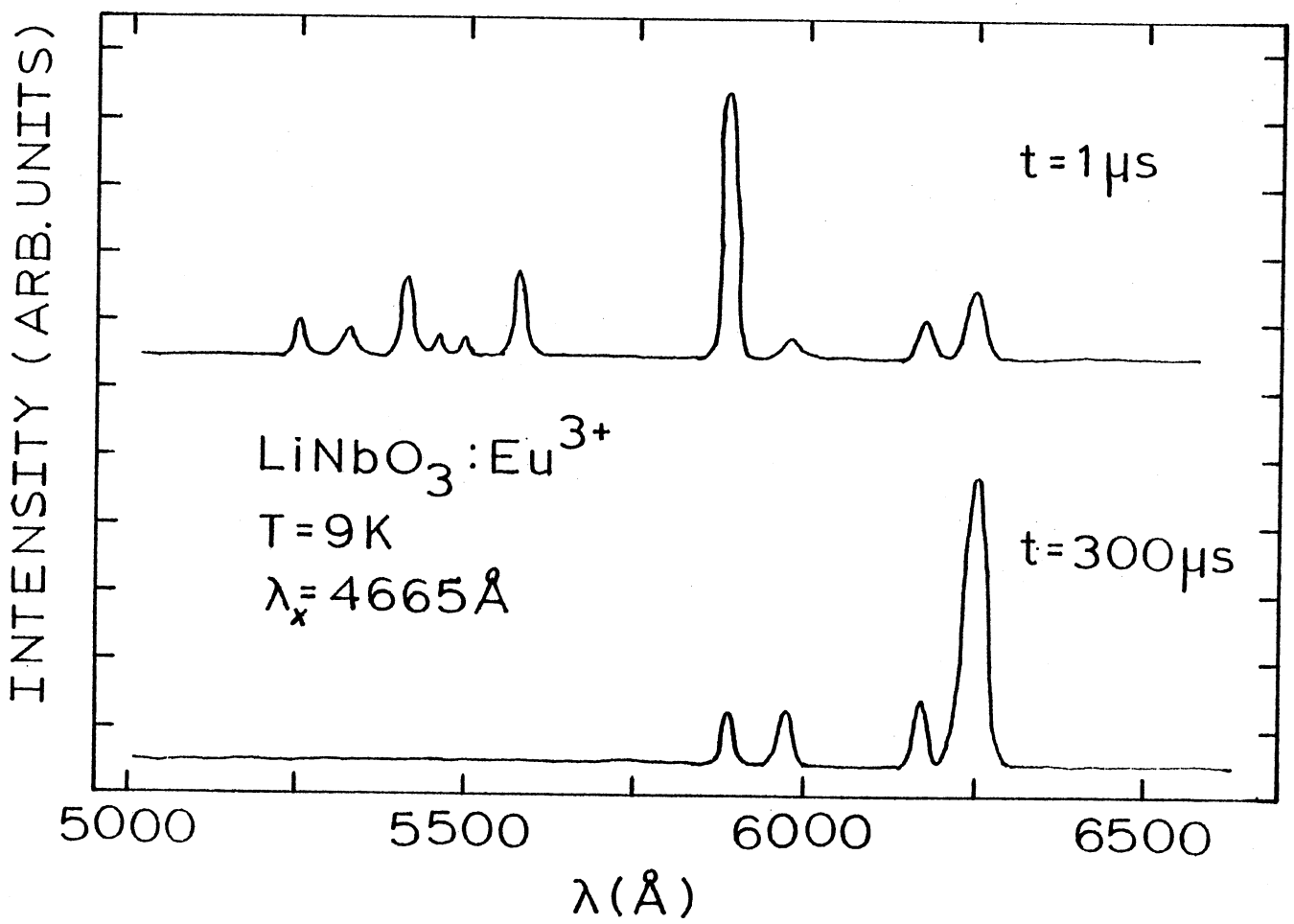

Figure III-2. Fluorescence Spectra of $LiNbO_3:Eu^{3+}$

TABLE III-I

OBSERVED Eu^{3+} TRANSITIONS IN $LiNbO_3$ AT 9°K WITH λ_x = 4665Å

λ Å	cm^{-1}	Width	Strength (1-10)	Identification
5285	18,921	5Å	2	$^5D_1 - {}^7F_0$
5364	18,643	18Å	1	$^5D_2 - {}^7F_4$
5416	18,464	14Å	3	$^5D_2 - {}^7F_4$
5446	18,362	10Å	1	$^5D_2 - {}^7F_4$
5455	18,332	5Å	1/2	$^5D_2 - {}^7F_4$
5480	18,248	10Å	1	$^5D_2 - {}^7F_4$
5573	17,944	15Å	5	$^5D_1 - {}^7F_2$
5582	17,915	7Å	3	$^5D_1 - {}^7F_2$
5635	17,746	5Å	1/2	$^5D_1 - {}^7F_2$
5646	17,712	5Å	1/2	$^5D_1 - {}^7F_2$
5878	17,013	5Å	9	$^5D_1 - {}^7F_2$
5884	16,995	5Å	9	$^5D_1 - {}^7F_2$
5888	16,984	5Å	9	$^5D_1 - {}^7F_2$
5893	16,969	5Å	9	$^5D_1 - {}^7F_2$
5934	16,852	5Å	2	$^5D_1 - {}^7F_2$
5970	16,750	8Å	3	$^5D_0 - {}^7F_1$
5986	16,706	5Å	2	$^5D_0 - {}^7F_1$
6168	16,213	5Å	3	$^5D_0 - {}^7F_2$
6179	16,184	10Å	4	$^5D_0 - {}^7F_2$
6185	16,168	5Å	3	$^5D_1 - {}^7F_4$
6244	16,015	20Å	10	$^5D_0 - {}^7F_2$
6258	15,980	15Å	9	$^5D_0 - {}^7F_2$
6295	15,886	10Å	1	$^5D_1 - {}^7F_4$
6305	15,860	4Å	1/2	$^5D_1 - {}^7F_4$
6340	15,773	6Å	1½	$^5D_1 - {}^7F_4$

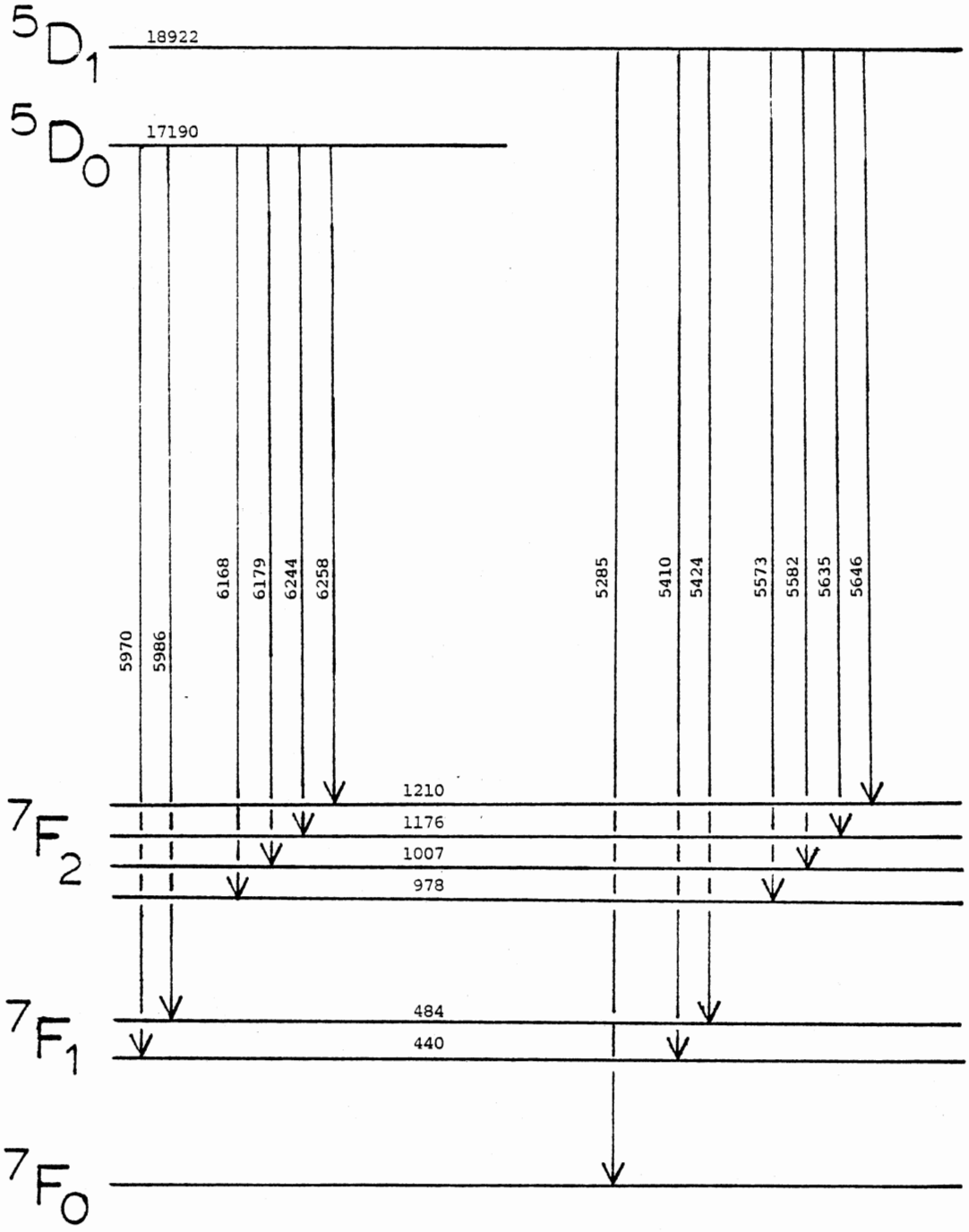

Figure III-3. Energy Levels of Eu^{3+} in $LiNbO_3$ at $9^{o}K$

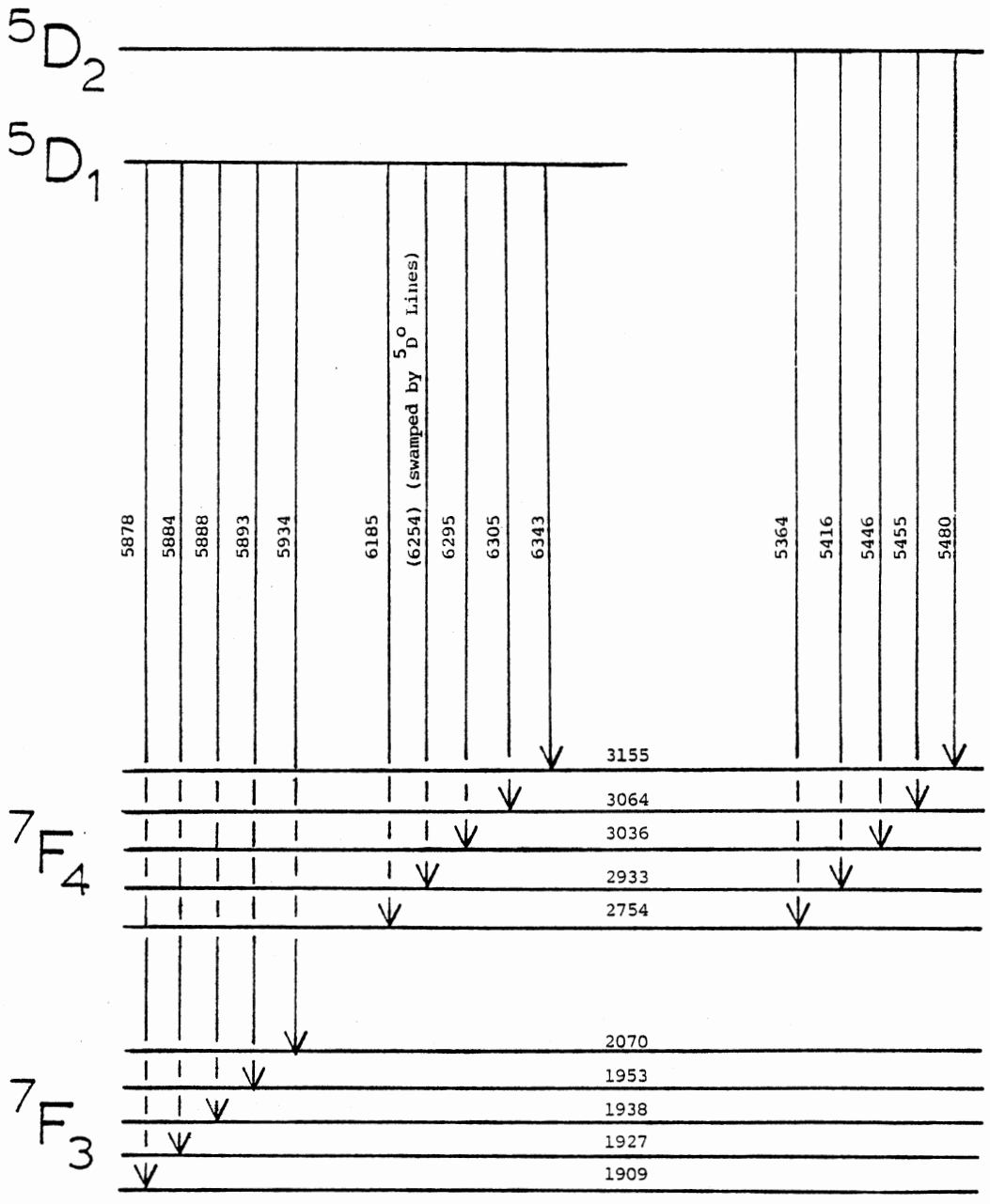

Figure III-3 (Continued)

The fluorescence spectra of Eu^{3+} in $LiNbO_3$ at $9^{\circ}K$ in the region between about 5870Å and 5910Å at 200 μs after laser excitation pulse is shown in Figure III-4 for excitation wavelengths λ_x = 4661.5Å, λ_x = 4663Å, and λ_x = 4665Å. At 200 μs after laser excitation pulse, the lines due to $^5D_1$ transitions and $^5D_2$ transitions have decayed away, and the structure shown in Figure III-4 results from transitions from the ^5D_o level. As can be seen from Figure III-4, the structure of these lines changes significantly with laser excitation wavelength, because the ions are in nonequivalent crystal field sites.

A typical spectrum of the fluorescence emission of the Eu^{3+} ions at $9^{\circ}K$ when excited at wavelength λ_x = 4665Å at two different times after the laser excitation pulse is shown in Figure III-5. It can be seen from Figure III-5 that the high energy (low wavelength) structure decreases with time and the low energy (high wavelength) structure increases with time. Thus Figure III-5 illustrates energy transfer from the "sensitizer" transitions (the high energy structure) to the "activator" transitions (the low energy structure). One can then characterize this transfer by integrating the lineshapes of the activator transitions and dividing this by the integrated line shape of the sensitizer transition to obtain the ratio of the activator to sensitizer intensity at a given time after pulse $\frac{I_a}{I_s}(t)$.

The time dependence of the ratio of the activator to sensitizer intensity at $9^{\circ}K$ and at $300^{\circ}K$ is shown in Table III-2 and Figure III-6. As will be discussed later, one can obtain qualitative and quantitative information about the mechanisms of energy transfer by fitting the data shown in Figure III-6 to various energy transfer theories.

The temperature dependence of the ratio of the activator to sensi-

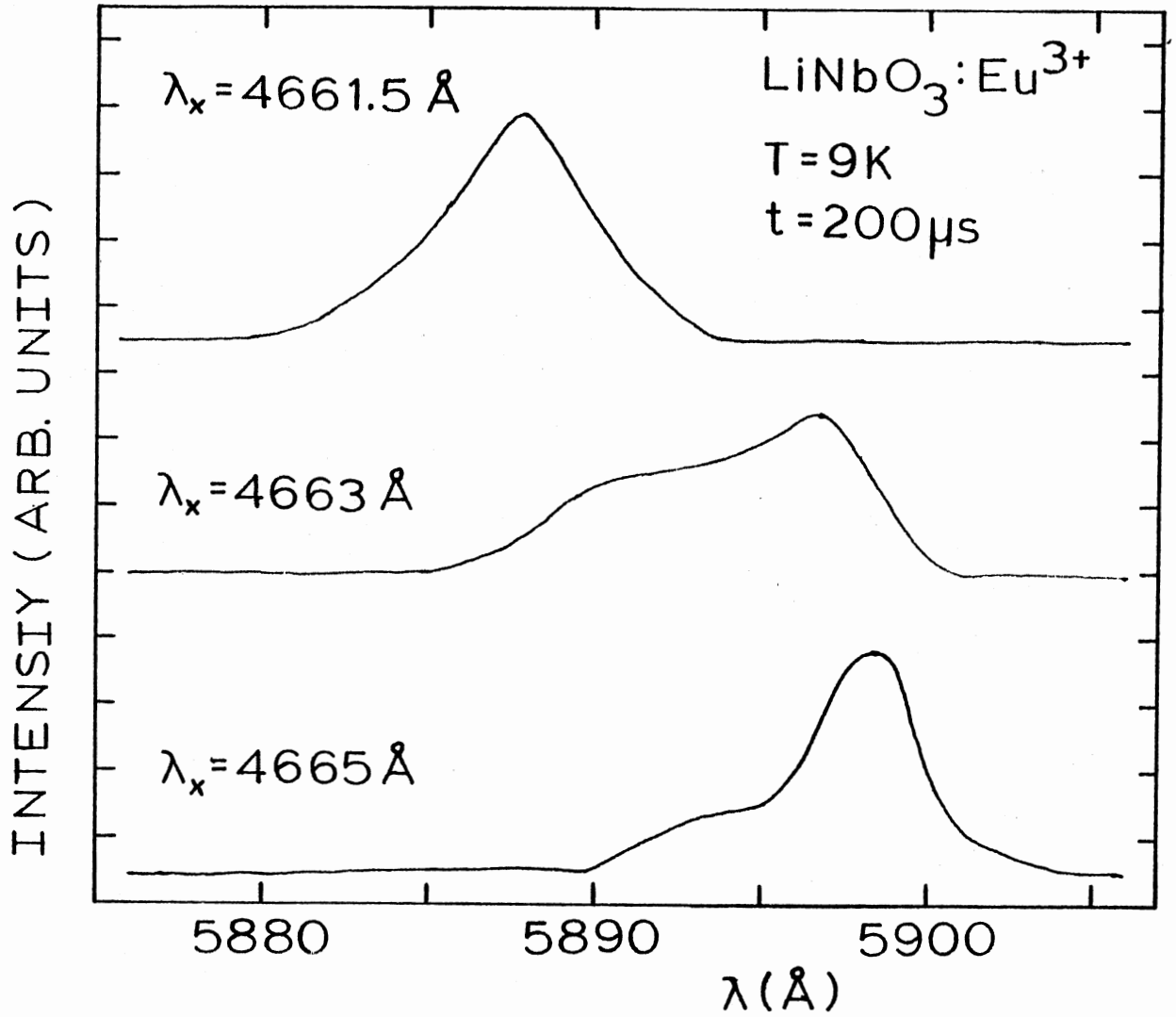

Figure III-4. Fluorescence Spectra of $LiNbO_3:Eu^{3+}$ at λ_x = 4661.5Å, λ_x = 4663Å, and λ_x = 4665Å

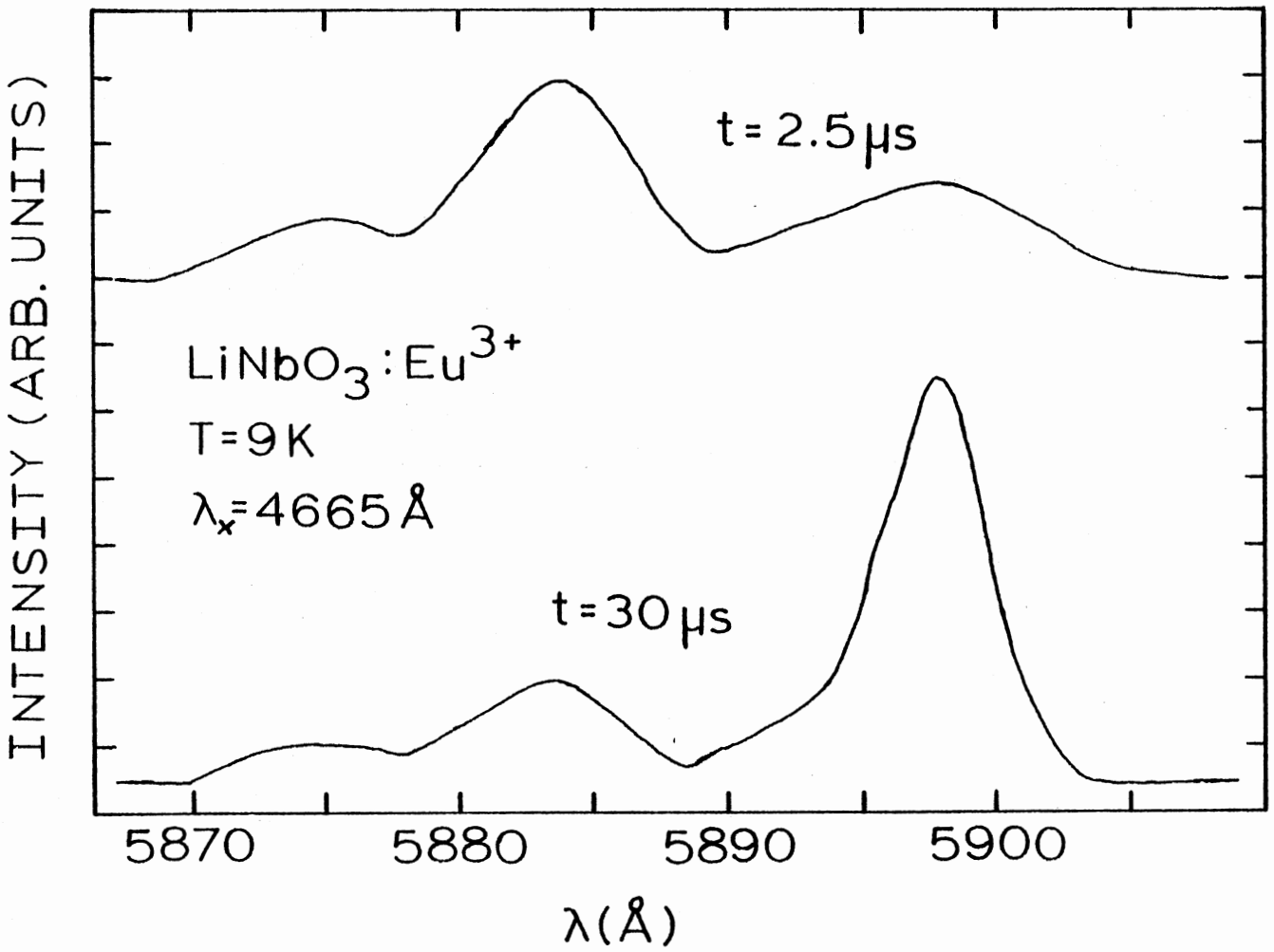

Figure III-5. Time Dependence of Fluorescence Spectra of $LiNbO_3:Eu^{3+}$

TABLE III-2

RATIO OF ACTIVATOR INTENSITY TO SENSITIZER INTENSITY AT DIFFERENT TIMES AFTER LASER EXCITATION PULSE FOR $LiNbO_3Eu^{3+}$ WITH EXCITATION WAVELENGTH 4665Å

$T = 9^{\circ}K$		$T = 300^{\circ}K$	
t(μs)	I_a/I_s	t(μs)	I_a/I_s
0.5	0.515	-----	-----
1	0.507	-----	-----
2.5	0.518	2.5	0.52
5	0.548	5	0.46
7.5	0.620	-----	-----
10	0.616	10	0.596
15	0.757	15	0.710
17.5	0.987	-----	-----
20	1.115	20	0.987
25	1.683	25	1.361
30	2.344	30	2.038
35	3.294	35	2.740

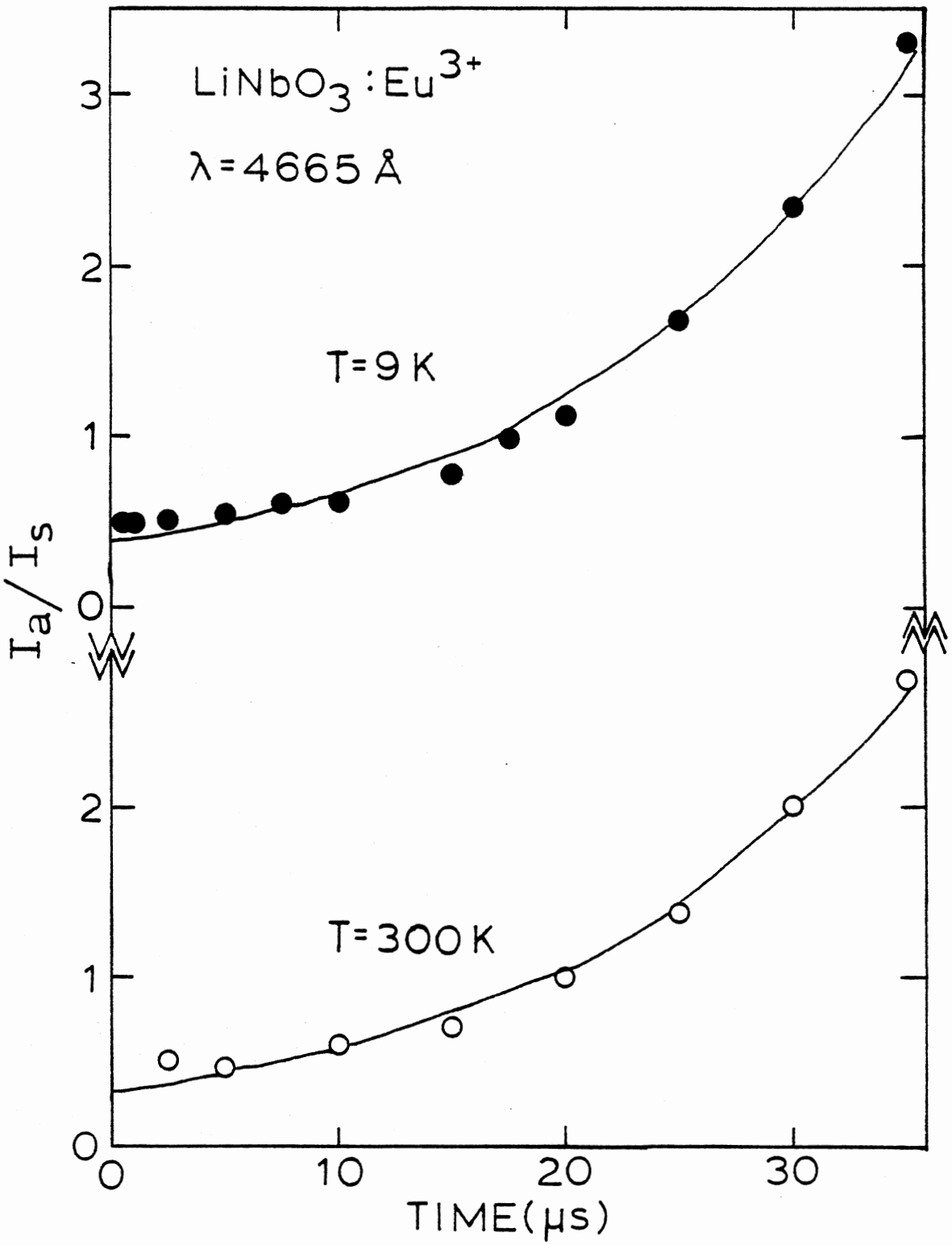

Figure III-6. Time Dependence of the Ratio of the Activator to Sensitizer Intensity at High and Low Temperatures. Solid Circles are Low Temperature Data, Empty Circles are High Temperature Data; See Text for Explanation of Theoretical Lines

tizer intensity at two different times after pulse is shown in Table III-3 and Figure III-7. One sees that $\frac{I_a(t)}{I_s(t)}$ is only weakly temperature dependent.

The temperature dependence of the fluorescence lifetimes of the sensitizer and activator transitions are shown in Table III-4 and Figure III-8. The lifetimes of both transitions are only weakly temperature dependent.

Figure III-6, III-7, and III-8 show that the energy transfer mechanism from sensitizers to activators is only weakly temperature dependent, which implies that phonon assisted energy transfer is probably not critically important.

Assuming no back transfer, one can model the time dependence of the data shown in Figure III-6 as a two level system as is shown in Figure III-9.

$W_s(t)$ and $W_a(t)$ are the pumping rates for the sensitizer and activator levels respectively, $n_s(t)$ and $n_a(t)$ are the populations of the sensitizer and activator levels respectively, β_s and β_a are the fluorescence decay rates of the sensitizer and activator levels respectively in the absence of transfer, and $\omega(t)$ is the energy transfer rate from the sensitizer to activator levels. The rate equation for the upper sensitizer level is

$$\frac{dn_s(t)}{dt} = W_s(t) - (\omega(t) + \beta_s)n_s(t) \qquad \text{(III-1)}$$

and the rate equation for the lower sensitizer level is

$$\frac{dn_a(t)}{dt} = W_a(t) + \omega(t)n_s(t) - \beta_a n_a(t) \ . \qquad \text{(III-2)}$$

TABLE III-3

TEMPERATURE DEPENDENCE OF THE RATIO OF THE ACTIVATOR INTENSITY TO THE SENSITIZER INTENSITY AT SHORT AND LONG TIMES AFTER THE LASER EXCITATION PULSE

$T(^{o}K)$	I_a/I_s (at t = 2.5 μs)	I_a/I_s (at t = 30 μs)
9	0.518	2.344
25	0.567	2.136
52	0.479	2.309
72	0.420	1.867
102	0.564	1.924
150	0.505	1.923
201	0.495	1.963
252	0.560	2.064
300	0.52	2.038

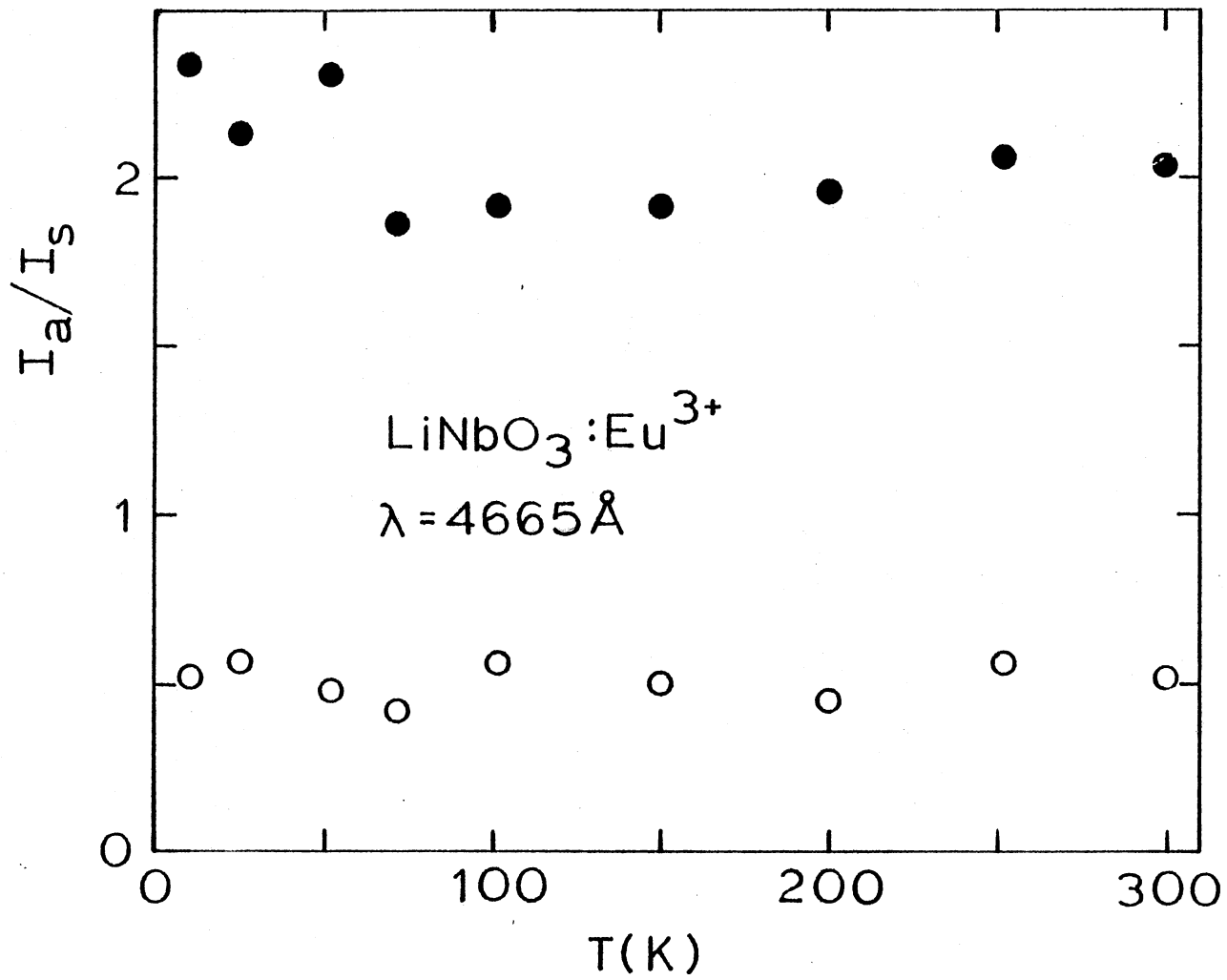

Figure III-7. Temperature Dependence of the Ratio of the Activator Intensity to the Sensitizer Intensity. The Solid Circles are at t = 30 μs; the Empty Circles are at t = 2.5 μs

TABLE III-4

LIFETIMES OF ACTIVATOR AND SENSITIZER
TRANSITIONS VS. TEMPERATURE

T(^{o}K)	Sensitizer Lifetime (μs)	Activator Lifetime (μs)
9	11.6	545.6
50	15.4	562.8
100	16.0	531.9
150	15.5	567.5
200	16.8	551.8
250	14.8	549.7
300	15.3	560.3

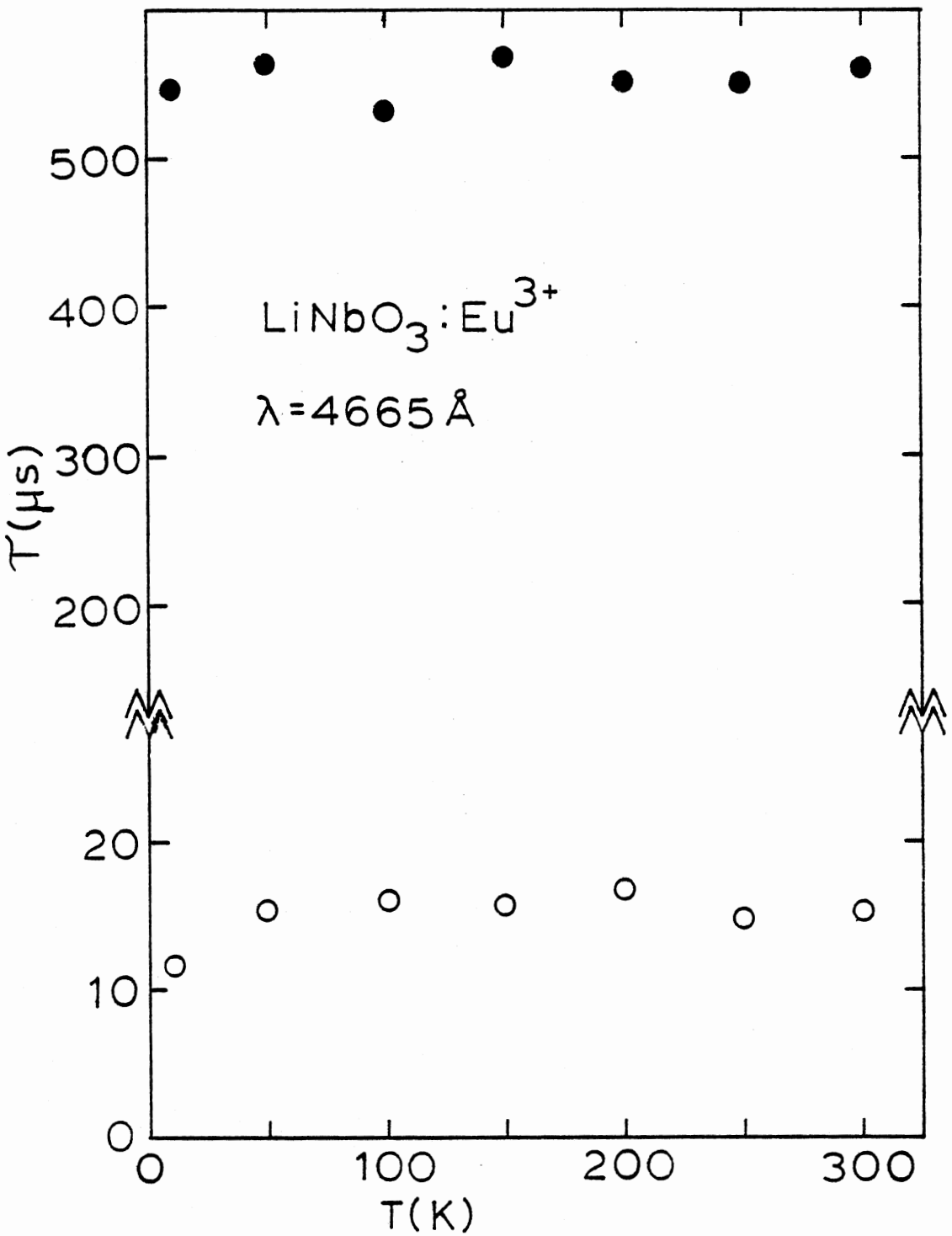

Figure III-8. Fluorescence Lifetimes of the Activator and Sensitizer Transitions Vs. Temperature. Solid Circles are the Activator Lifetimes, Empty Circles are the Sensitizer Lifetimes

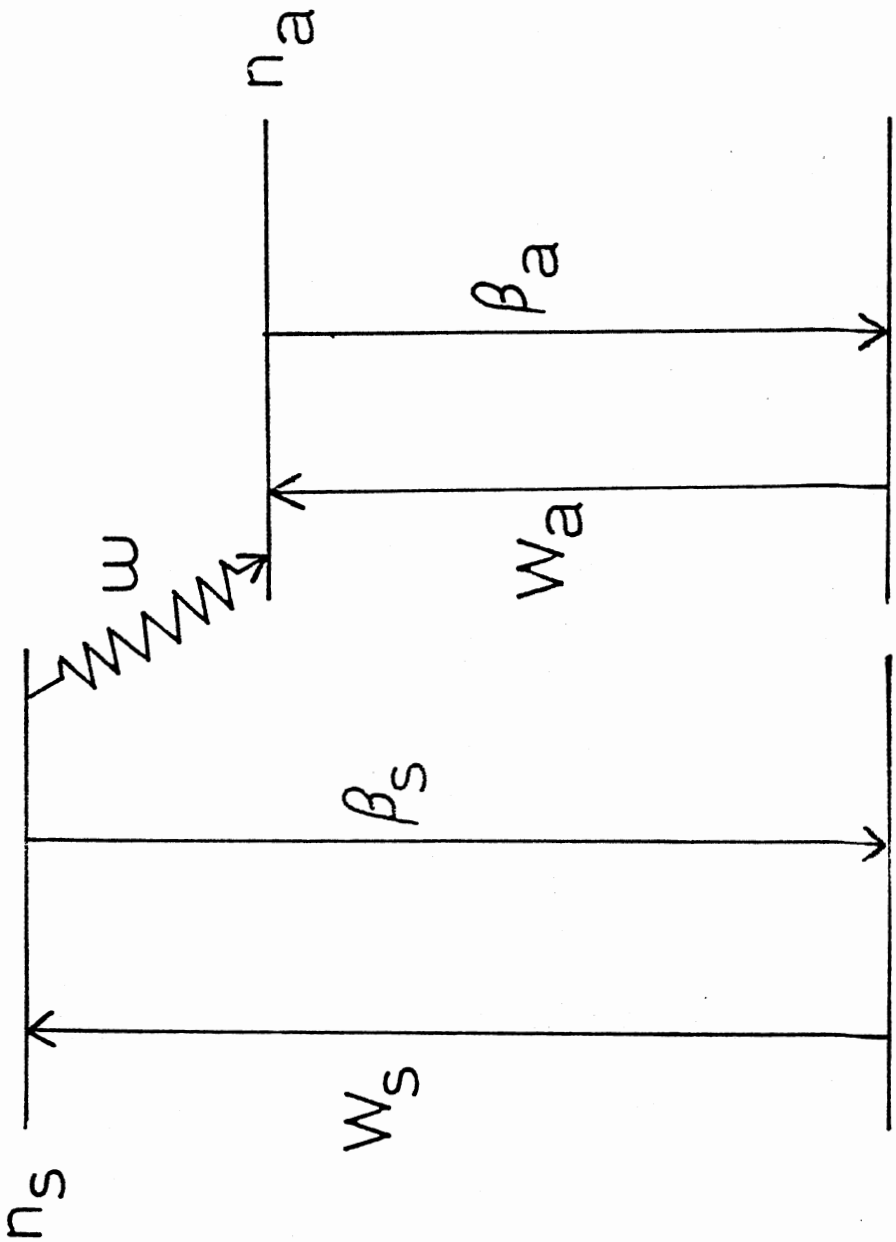

Figure III-9. $LiNbO_3:Eu^{3+}$ Energy Transfer Model

The direct laser excitation is to the $^5D_2$ levels for both the sensitizer and the activator ions. If the assumption is made that the sensitizer ions relax from the directly pumped $^5D_2$ levels to the $^5D_1$ levels with relaxation rate ω_s, then $W_s(t)$ may be written as

$$W_s(t) = A\ell^{-\omega_s t} \tag{III-3}$$

where A is a constant. Similarly, if the assumption is made that the activator ions relax from the directly pumped $^5D_2$ levels to the ^5D_o levels with relaxation rate ω_a, then $W_a(t)$ may be written as

$$W_a(t) = B\ell^{-\omega_a t}$$

where B is a constant. Equations (III-1) and (III-2) then become

$$\frac{dn_s(t)}{dt} + (\omega(t) + \beta_s)n_s(t) = A\ell^{-\omega_s t} \tag{III-5}$$

and

$$\frac{dn_a(t)}{dt} + \beta_a n_a(t) = B\ell^{-\omega_a t} + \omega(t)n_s(t) \; . \tag{III-6}$$

If one assumes a constant transfer rate ω, the solution to Equation (III-5) is

$$n_s(t) = \left(\frac{A}{(\omega+\beta_s)-\omega_s}\right)(\ell^{-\omega_s t} - \ell^{-(\omega+\beta_s)t}) \tag{III-7}$$

and the solution to Equation (III-6) is

$$n_a(t) = \frac{B}{(\beta_a-\omega_a)}\left(\ell^{-\omega_a t} - \ell^{-\beta_a t}\right)$$

$$+ \frac{A\omega}{(\omega+\beta_s-\omega_s)}\left\{\frac{\ell^{-\omega_s t} - \ell^{-\beta_a t}}{\beta_a-\omega_s}\right. \qquad \text{(III-8)}$$

$$+ \left.\frac{\left(\ell^{-\beta_a t} - \ell^{-(\omega+\beta_s)t}\right)}{(\beta_a-\omega-\beta_s)}\right\}$$

The ratio of the activator intensity to the sensitizer intensity $I_a(t)/I_s(t)$ is given by

$$\frac{I_a(t)}{I_s(t)} = \frac{\beta_a^r}{\beta_s^r}\left(\frac{n_a(t)}{n_s(t)}\right) \qquad \text{(III-9)}$$

where β_a^r and β_s^r are the radiative decay rates of the activator and sensitizer transitions, respectively.

The ratio of the integrated intensities of the activator and sensitizer transitions $\frac{I_a(t)}{I_s(t)}$ is then given by

$$\frac{I_a(t)}{I_s(t)} = \frac{\beta_a^r}{\beta_s^r}\left\{(B/A)\,\frac{\left(\ell^{-\omega_a t} - \ell^{-\beta_a t}\right)}{(\beta_a-\omega_a)}\right.$$

$$+ \left(\frac{\omega}{\beta'-\omega_s}\right)\left[\frac{\left(\ell^{-\omega_s t} - \ell^{-\beta_a t}\right)}{\beta_a-\omega_s}\right. \qquad \text{(III-10)}$$

$$+ \left.\left.\frac{\left(\ell^{-\beta_a t} - \ell^{-\beta' t}\right)}{(\beta_a-\beta')}\right]\right\}$$

$$\div \left\{\frac{\ell^{-\omega_s t} - \ell^{-\beta' t}}{\beta'-\omega_s}\right\}$$

where $\beta' = \omega + \beta_s$ is the inverse of the measured sensitizer fluorescence decay time.

Since $I_s = \beta_s^r n_s(t)$, one can obtain the pumping rate ω_s of the sensitizer level by observing that $\left.\frac{dn_s(t)}{dt}\right|_{t=\tau_{rise}^s} = 0$. By numerically solving the resulting equation, one obtains $\omega_s = 129{,}000\ \text{sec}^{-1}$. Using $I_a = \beta_a^r n_a(t)$ and $\left.\frac{dn_a(t)}{dt}\right|_{t=\tau_{rise}^a} = 0$, one can similarly obtain the pumping rate of the activator level to be $\omega_a = 80{,}000\ \text{sec}^{-1}$.

As can be seen from Figure III-8, the sensitizer lifetimes and the activator lifetimes have no noticeable temperature dependence. Averaging these lifetimes, the average sensitizer lifetime $\tau_s = 15.1\ \mu s$ and the average activator lifetimes $\tau_a = 553\ \mu s$.

By assuming B/A = 1 (i.e., the initial pumping of the sensitizer and activator levels is the same) and taking $\beta_a = \frac{1}{\tau_a}$ and $\beta' = \frac{1}{\tau_s}$, one can perform a non-linear least square fit of Equation (III-10) to the data shown in Figure III-6 to obtain the solid theoretical curves shown in Figure III-6. For the low temperature data one obtains $\frac{\beta_a^r}{\beta_s^r} = 0.373$ and $\omega = 7560\ \text{sec}^{-1}$, and for the high temperature data one obtains $\frac{\beta_a^r}{\beta_s^r} = 0.327$ and $\omega = 3148\ \text{sec}^{-1}$. Thus a very good fit to the data is obtained by assuming a constant sensitizer-activator transfer rate ω. If ω was not constant, it would decrease with time causing the theoretical curves shown in Figure III-6 to curve up more slowly with time, giving an inferior fit to the data. Thus one can conclude that the transfer rate is time independent. While the theoretical data fit shown in Figure III-6 is a very good qualitative fit, the transfer rate ω is very sensitive to parameters such as the sensitizer lifetime and pumping rate,

and the values for ω should be considered as order of magnitude estimates.

Two energy transfer mechanisms can lead to a transfer rate ω that is approximately constant. The transfer rate is approximately constant either if the transfer mechanism is exciton diffusion and trapping or if the energy transfer is between sensitizer-activator pairs at a fixed distance.

If the energy transfer mechanism is an exciton diffusion and trapping mechanism the transfer rate can be expressed as (1)

$$\omega = 4\pi D R_t C_E \qquad \text{(III-11)}$$

where D is the diffusion constant, R_t is the trapping radius, and C_E is the concentration of Eu^{3+} ions. Assuming a uniform distribution of Eu^{3+} ions and Eu^{3+} nearest-neighbor trapping radius, the diffusion constant at $9^{o}K$ is given by Equation (III-11) to be equal to 1.7×10^{-11} $\frac{cm^2}{sec}$, and the diffusion constant at $300^{o}K$ is given by Equation (III-11) as 7.0×10^{-12} $\frac{cm^2}{sec}$. The time for each step in the exciton random walk can be approximated by (23)

$$t_h = a^2/6D \qquad \text{(III-12)}$$

where a is the hopping distance. Assuming the hopping distance to be approximately equal to the Eu^{3+} nearest neighbor separation for a uniform distribution, Equation (III-12) gives t_h = 9286 μs at $9^{o}K$ and t_h = 22287 μs at $300^{o}K$. For the diffusion model to be valid, the exciton must take many steps in the random walk before it is destroyed. Thus t_h must be much less than the sensitizer fluorescence lifetime for the diffusion model to be valid. Not only are the calculated values of t_h actually much larger than the sensitizer lifetime, but for the diffusion model to

be valid the transfer rate ω would have to be four or five orders of magnitude larger than was obtained from the theoretical data fit. Thus one can conclude that the constant energy transfer rate is not due to a diffusion and trapping mechanism.

The energy transfer rate ω can also be time independent if there is transfer between sensitizer-activator pairs at a fixed distance apart. Assuming a dipole-dipole interaction, the transfer rate ω is given by

$$\omega = \beta_s \left(\frac{R_o}{R}\right)^6 . \qquad \text{(III-13)}$$

One can estimate the distance R as having a lower bound equal to the closest Nb-Li separation of 3.01Å (23) and an upper bound equal to the average Eu^{3+} separation if the ions are uniformly distributed which is equal to 96.8Å. Using Equation (III-13), one obtains a maximum value for R_o given by $R_o = 58$Å at 300°K and $R_o = 67.3$Å at 9°K; and a minimum value for R_o given by $R_o = 2.1$Å at 9°K and $R_o = 1.8$Å at 300°K.

Since one expects R_o to be somewhere between 1Å and 10Å, one obtains physically reasonable results for R_o by interpreting the constant transfer rate as being due to energy transfer between sensitizer-activator pairs at a fixed distance apart.

CHAPTER IV

FOUR WAVE MIXING SPECTROSCOPY IN $Nd_xLa_{1-x}P_5O_{14}$

Motivation

The Nd ion in various host media has proved to be an excellent active ion for optically pumped lasers (24). Strong absorbsion bands in the near infrared make possible efficient pumping by light emitting diodes.

The dominant laser line at about 1.06Å is an attractive wavelength for fiber optics communication because of the low loss of glass fibers at this wavelength.

When constructing miniature lasers or "mini-lasers", it is important to have a very high Nd concentration (25). However, the Nd ion exhibits strong concentration quenching in most laser host materials. The mechanism for this quenching can either be cross relaxation between ion pairs or energy migration to sinks, depending on the exact position of the energy levels and the separation of the Nd ions.

NdP_5O_{14} is a crystal with high Nd concentration but remarkably low concentration quenching. Thus NdP_5O_{14} is a desirable material for constructing mini-lasers, particularly since the technique for growing these crystals has markedly improved recently (26).

Because of the importance of NdP_5O_{14} lasers, it is important to understand the mechanism of concentration quenching in these materials. There has been much interest and some controversy over the mechanism of concentration quenching in NdP_5O_{14}, with four primary models having

been proposed.

The first mechanism proposed (27,29) is an ion-ion cross relaxation mechanism where one ion in the $^4F_{3/2}$ state and another ion in the $^4I_{9/2}$ state cross relax to the intermediate $^4I_{15/2}$ state, which is the quenching mechanism of Nd^{3+} in most host crystals such as YAG. However, this model predicts that the quenching rate varies quadratically with concentration, and generally has a strong temperature dependence. Both of these predictions are contrary to experimental results (25,27-30,45-48). The quenching rate is actually temperature independent and varies linearly with the concentration. Furthermore, recent studies of the effects of pressure on the lifetimes of $Nd_xY_{1-x}P_5O_{14}$ do not favor the cross relaxation model (49).

A second model for the quenching mechanism is a crystal field overlap model (50), but this model predicts a concentration dependence in the oscillator strengths, and this has been shown to be false (51).

A third model for the quenching mechanism is the migration of energy to randomly distributed "traps" which then dissipate the energy radiationlessly (28,30,31,48). However, site selection spectroscopy indicates that energy transfer between Nd^{3+} ions in nonequivalent crystal field sites is very inefficient (52), which suggests that the traps would have to be a type of impurity or defect. To obtain the required linear dependence of quenching rate with concentration, the assumption must be made that trap concentration is independent of the Nd^{3+} concentration (48).

The fourth model proposed to explain the quenching mechanism is a surface quenching model where the energy migrates to the surface where it is quenched (52). However, this model predicts that the quenching rate should depend on the absorption coefficient and on the sample

surface environment; and experiment has shown these changes in the quenching rate to be only about 10%, which is much less than one would expect if this model is valid.

None of these four models has been conclusively shown to correctly account for all of the concentration quenching properties of $Nd_xLa_{1-x}P_5O_{14}$. One of the most important parameters in determining which of the above theories is most valid is the magnitude of the average exciton migration length, which measures the diffusion strength. Although there has been great interest in determining this migration length, results have been very conflicting, with estimates varying from only a few angstroms to several microns (27-35).

Site selection spectroscopy is a standard technique for determining the diffusion length, but this type of experiment cannot be carried out for $Nd_xLa_{1-x}P_5O_{14}$ because the energy transfer between Nd^{3+} ions in non-equivalent crystal field sites is very inefficient in $Nd_xLa_{1-x}P_5O_{14}$.

One technique for directly determining this migration length involves the use of degenerate four wave mixing (FWM) spectroscopy which is a method for determining the spatial energy migration without spectral transfer in solids (36-39).

This technique has been used to determine the molecular exciton migration length in organic solids (36), but attempts to make similar measurements of the exciton migration length in inorganic materials have resulted only in putting an upper bound on the migration length because of the small migration lengths involved (37-39).

This chapter will describe the successful measurement of the exciton migration length using FWM in $Nd_{.2}La_{.8}P_5O_{14}$, $Nd_{.6}La_{.4}P_5O_{14}$, and the pure crystal NdP_5O_{14}.

Theory of Four Wave Mixing

The four wave mixing process can be thought of as the production and reading out of a holographic index of refraction grating in a non-linear medium. In the four wave mixing configuration generally used to study energy migration, a laser beam is split into two strong "pump" beams of wave vectors $\underset{\sim}{k}_a$ and $\underset{\sim}{k}_b$, and a weaker "probe" beam of wavevector $\underset{\sim}{k}_p$ which counterpropagates against one of the pump beams. The two pump beams establish or "write" the grating and the probe beam "reads" the grating (see Figure IV-1).

The two pump beams interfere in the medium and optical absorption by the active ions creates a spatial distribution of excited states with a sinusoidal pattern of wavevector $\underset{\sim}{k}_g = \underset{\sim}{k}_b - \underset{\sim}{k}_a$. Corresponding to the grating wavevector $\underset{\sim}{k}_g$ is the grating wavelength Λ given by

$$\Lambda = \frac{\lambda}{2 \sin \theta/2}$$

where λ is the laser wavelength and θ is the crossing angle of the two pump beams.

The depth of the grating can then be probed by Bragg diffraction of the probe beam off of the grating. With the probe beam counterpropagating against the second write beam which has wavevector $\underset{\sim}{k}_b$, the Bragg condition requires the Bragg scattered signal beam to have wave vector $\underset{\sim}{k}_s = \underset{\sim}{k}_p + \underset{\sim}{k}_g = - \underset{\sim}{k}_a$, which implies that the signal beam counterpropagate back against the first pump beam.

The theory of FWM has recently been addressed in several papers (36,40-43). Two fundamentally different approaches have been used to model the FWM process.

References (40-42) explicitly consider the non-linear wave equations

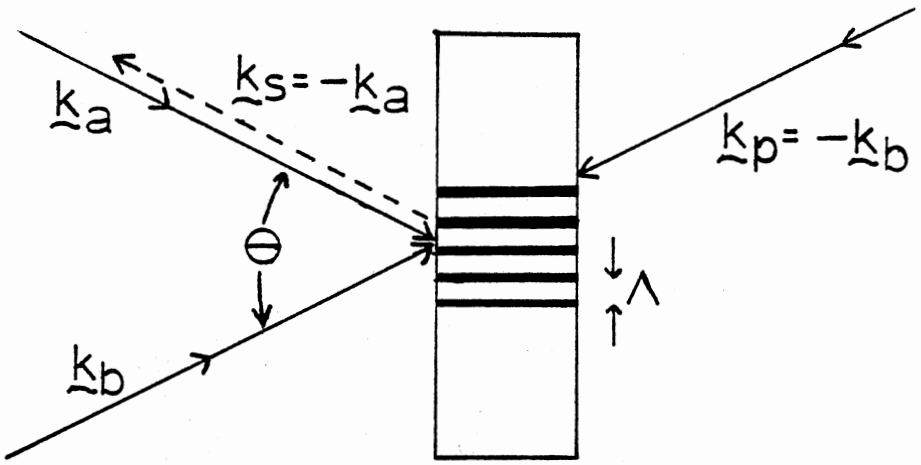

Bragg Condition $\underset{\sim}{k}_s = \underset{\sim}{k}_p + \underset{\sim}{k}_g = -\underset{\sim}{k}_a$

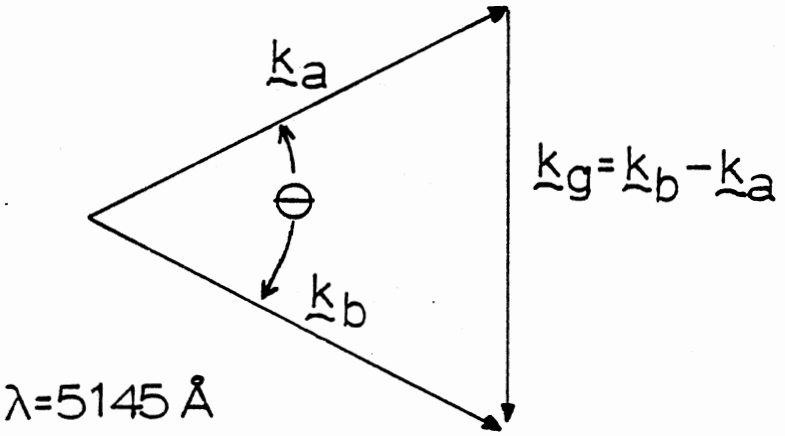

$$\Lambda = \frac{\lambda}{2\sin(\Theta/2)} \approx \frac{\lambda}{\Theta}$$

Figure IV-1. Four Wave Mixing Wavevector Configuration

where the electric fields are coupled by the non-linear susceptibility in the material. Furthermore, (41) and (42) consider the mechanisms creating this non-linear susceptibility by modeling the system as an ensemble of two and three level atoms, respectively.

References (36,43) model the system in a very different way, where the probe beam Bragg diffracts off of a sinusoidally varying complex index of refraction grating. In this type of development, one assumes a spatially varying susceptibility $X(x,y,z)$ which forms a spatially varying holographic grating in the material. This is similar to the approach used by Kogelnik (53). The emphasis in this development is in understanding how the spatial properties (43) or temporal properties (36) of the grating affect the Bragg diffracted signal. However, this approach completely ignores the mechanisms creating the non-linear susceptibility which causes the spatially varying grating.

The approach used by References (41-42) yields important information about how the intrinsic properties of the material affect the steady state scattering efficiency. However, References (41-42) assume that the pump beams are counterpropagating and that the pump beams are exactly phase matched. In the first part of this chapter, the FWM scattering efficiency will be derived when the media is modeled as a two-level system as in Reference (41) but important extensions to the theory will be made. Instead of assuming counterpropagating pump beams, the assumption will be made that the pump beams intersect at crossing angle θ (a more common configuration in FWM energy migration studies). Furthermore, effects arising whenever the pump beams are not exactly phase matched will be explored. Thus the first part of this chapter will give information about how the pump beam properties and intrinsic properties of the material affect the steady state scattering efficiency.

The approach used in Reference (36) is much more useful in studying the temporal properties of the grating decay. In the second part of this chapter, the time evolution of the decay of the signal beam intensity is derived in a manner similar to Reference (36).

The last part of this chapter describes FWM data taken on $Nd_xLa_{1-x}P_5O_{14}$ crystals.

Derivation of Scattering Efficiency

The assumptions will be made that all beams are linearly polarized in the same direction, with the pump beam electric fields given by $E_2(\underset{\sim}{r},t)$ and $E_4(\underset{\sim}{r},t)$, the probe beam field as $E_1(\underset{\sim}{r},t)$, and the Bragg diffracted signal beam field as $E_3(\underset{\sim}{r},t)$.

If the z axis is taken to be along the pump beam with electric field E_4, then the configuration will be as shown in Figure IV-2.

If one makes the "parametric approximation" that the pump beams are undepleted in the media, then the four electric fields are given as

$$E_1(\underset{\sim}{r},t) = A_1(z)\,\ell^{i\omega t}\,\ell^{-i\underset{\sim}{k}_1\cdot\underset{\sim}{r}} = \ell^{i\omega t}\,E_1(\underset{\sim}{r})$$

$$E_2(\underset{\sim}{r},t) = A_2\,\ell^{i\omega t}\,\ell^{i\underset{\sim}{k}_1\cdot\underset{\sim}{r}} = \ell^{i\omega t}\,E_2(\underset{\sim}{r})$$

$$E_3(\underset{\sim}{r},t) = A_3(z)\,\ell^{i\omega t}\,\ell^{-i\underset{\sim}{k}_3\cdot\underset{\sim}{r}} = \ell^{i\omega t}\,E_3(\underset{\sim}{r})$$

$$E_4(\underset{\sim}{r},t) = A_4\,\ell^{i\omega t}\,\ell^{i\underset{\sim}{k}_3\cdot\underset{\sim}{r}} = \ell^{i\omega t}\,E_4(\underset{\sim}{r})\ .$$

In the configuration used, there is no incident signal beam (i.e., $A_3(L) = 0$) and the signal beam will be much weaker than the probe beam

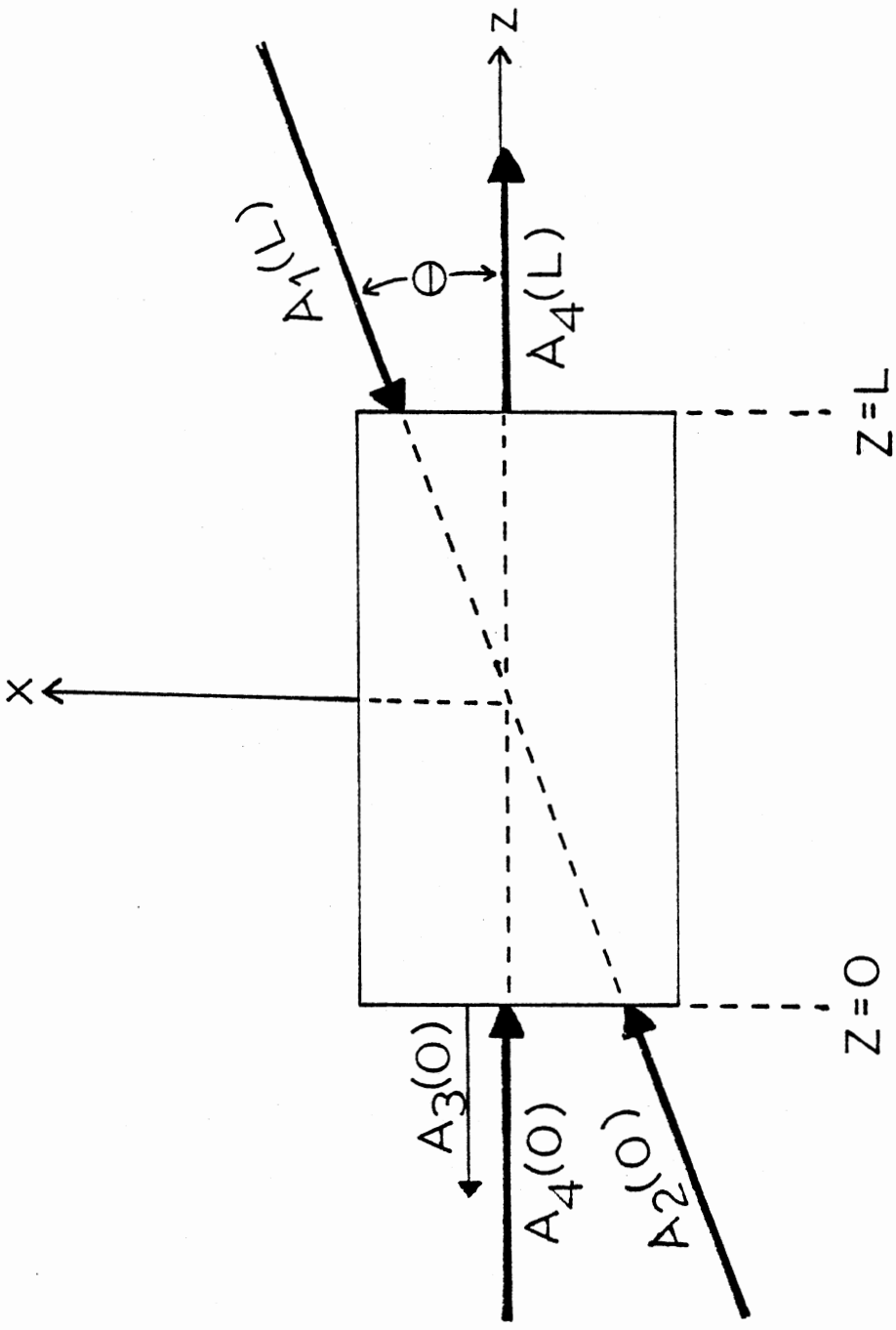

Figure IV-2. Four Wave Mixing Geometry

throughout the material. Since the probe beam is also much weaker than the pump beams,

$$|A_2|^2,\ |A_4|^2 >> |A_1|^2 >> |A_3|^2$$

and thus $|\frac{\Delta E}{E_o}| << 1$ where $E_o = E_2(\underset{\sim}{r}) + E_4(\underset{\sim}{r})$ and $\Delta E = E_1(\underset{\sim}{r}) + E_3(\underset{\sim}{r})$. The total electric field is then $E(\underset{\sim}{r},t) = \ell^{i\omega t}(E_o+\Delta E)$.

The wave equation that these fields must obey in the material is

$$\nabla^2 E - \varepsilon_o \mu_o \partial_t^2 E = \mu_o \partial_t^2 P \qquad \text{(IV-1)}$$

where ε_o is the permitivity constant, μ_o is the permeability constant, and P is the polarization. The polarization P may be expressed in terms of the susceptibility χ as

$$P(E) = \varepsilon_o \chi(E) E \ . \qquad \text{(IV-2)}$$

The media can now be modeled as a two-level system. As is shown in Appendix A, the susceptibility for a two-level system is given by

$$\chi(E) = -\frac{2\alpha_o}{k}\left(\frac{i+\delta}{1+\delta^2+|E/E_s|^2}\right) \qquad \text{(IV-3)}$$

where δ is the normalized detuning from line center, $|E_s|^2$ is the saturation intensity, and α_o is the line center small-signal field attenuation coefficient.

Using $|\frac{\Delta E}{E_o}| << 1$, one can expand $\chi(E)$ and $P(E)$ about E_o to first order in $|\frac{\Delta E}{E_o}|$ to obtain

$$\chi(E_o+\Delta E) = \chi(E_o)\left\{1 - \frac{(E_o \Delta E^* + E_o^* \Delta E)}{|E_s|^2(1+\delta^2)+|E_o|^2}\right\} \qquad \text{(IV-4)}$$

The polarization is given by (IV-2), and if one defines $I_s \equiv |E_s|^2(1+\delta^2)$, then to first order in $|\Delta E/E_o|$,

$$P(E_o+\Delta E) = \ell^{i\omega t}\varepsilon_o\chi(E_o)\ \{E_o+\Delta E - \frac{(E_o^2\Delta E^* + |E_o|^2\Delta E)}{I_s + |E_o|^2}\} . \qquad \text{(IV-5)}$$

Since $k^2 = |\underset{\sim}{k}_1|^2 = |\underset{\sim}{k}_3|^2$, the driving term $\mu_o\partial_t^2 P$ for Equation (IV-1) can be written as

$$\mu_o\partial_t^2 P = - k^2\ell^{i\omega t}\ \chi(E_o)\ \{E_o+\Delta E - \frac{(E_o^2\Delta E^* + |E_o|^2\ \Delta E)}{I_s + |E_o|^2}\} . \qquad \text{(IV-6)}$$

The left hand side of Equation (IV-1) now must be calculated.

The slowly varying envelope approximation,

$$|\frac{d^2Ai}{dz^2}| << |k\ \frac{dAi}{dz}|\ \ i = 1,3$$

implies that the field amplitude variation due to non-linear coupling is small over a wavelength.

E_1 and E_3 can be expressed as $E_1 = A_1(z)\ell^{i(k\cos\theta z + k\sin\theta z)}$

$$E_3 = A_3(z)\ell^{ikz}$$

so using the slowly varying envelope approximation,

$$\nabla^2 E - \varepsilon_o\mu_o\partial_t^2 E = 2ik\ell^{i\omega t}\ (\cos\theta\ell^{-i\underset{\sim}{k}_1\cdot\underset{\sim}{r}}\ \partial_z A_1(z) + \ell^{-i\underset{\sim}{k}_3\cdot\underset{\sim}{r}}\ \partial_z A_3(z)) . \qquad \text{(IV-7)}$$

Combining (IV-6) and (IV-7), the wave Equation (IV-1) becomes

$$2i(\cos\theta\ell^{-i\underset{\sim}{k}_1\cdot\underset{\sim}{r}}\ \partial_z A_1(z) + \ell^{-i\underset{\sim}{k}_3\cdot\underset{\sim}{r}}\ \partial_z A_3(z)) = - k\chi(E_o)$$

$$\{E_o + \Delta E - \frac{[E_o^2 \Delta E^* + |E_o|^2 \Delta E]}{I_s + |E_o|^2}\} . \qquad \text{(IV-8)}$$

One may write out $|E_o|^2$ as

$$|E_o|^2 = |A_2|^2 + |A_4|^2 + A_2 A_4^* \ell^{i(\underset{\sim}{k}_1 - \underset{\sim}{k}_3)\cdot \underset{\sim}{r}} + A_2^* A_4 \ell^{-i(\underset{\sim}{k}_1 - \underset{\sim}{k}_3)\cdot \underset{\sim}{r}} .$$

The intensities of the pump beams are given by $I_2 = |A_2|^2$ and $I_4 = |A_4|^2$, so if one defines

$$\zeta \equiv A_2 A_4^* \ell^{i(\underset{\sim}{k}_1 - \underset{\sim}{k}_3)\cdot \underset{\sim}{r}} ,$$

then

$$|E_o|^2 = I_2 + I_4 + \zeta + \zeta^* .$$

Along the z axis, ζ is given by $\zeta(z) = A_2 A_4^* \ell^{ik(1-\cos\theta)z}$, so $\zeta(z)$ oscillates with z with oscillation wavelength $\lambda_{os} = \frac{\lambda}{1-\cos\theta}$; and thus $|E_o|^2$ has an interference term that oscillates with z with oscillation wavelength λ_{os}.

The only terms of interest on the right hand side of (IV-8) are those that satisfy the phase matching condition; i.e., those terms that synchronously drive $\nabla^2 E - \varepsilon_o \mu_o \partial_t^2 E$ as either $\ell^{i(\omega t - \underset{\sim}{k}_3 \cdot \underset{\sim}{r})}$ or $\ell^{i(\omega t - \underset{\sim}{k}_1 \cdot \underset{\sim}{r})}$.

Rewriting (IV-8) and numbering the terms, (IV-8) becomes

$$[\cos\theta \ell^{-i\underset{\sim}{k}_1 \cdot \underset{\sim}{r}} \partial_z A_1(z) + \ell^{-i\underset{\sim}{k}_3 \cdot \underset{\sim}{r}} \partial_z A_3(z)] = \qquad \text{(IV-9)}$$

$$\alpha_o |E_s|^2 (1 - i\delta) \{ \underbrace{\frac{E_o}{I_s + |E_o|^2}}_{\text{term (i)}} + \underbrace{\frac{\Delta E}{I_s + |E_o|^2}}_{\text{term (ii)}}$$

$$- \frac{E_o^2 \Delta E^*}{(I_s + |E_o|^2)^2} - \frac{|E_o|^2 \Delta E}{(I_s + |E_o|^2)^2}\} . \qquad \text{(IV-9)}$$

term (iii) term (iv)

Terms (i), (ii), (iii), and (iv) must now each in turn be examined to determine which of these satisfy the phase matching condition.

Since $E_o = A_2 \ell^{i\tilde{k}_1 \cdot \tilde{r}} + A_4 \ell^{i\tilde{k}_3 \cdot \tilde{r}}$, term (i) is clearly not synchronous with the left hand side of (IV-9) and thus term (i) is not phase matched.

Since $\Delta E = A_1(z) \ell^{-i\tilde{k}_1 \cdot \tilde{r}} + A_3(z) \ell^{-i\tilde{k}_3 \cdot \tilde{r}}$, term (ii) clearly is phase matched although the amplitude of this term will be modulated by the oscillatory behavior of $|E_o|^2$ which appears in the denominator.

E_o^2 may be written explicitly as

$$E_o^2 = A_2^2 \ell^{2i\tilde{k}_1 \cdot \tilde{r}} + A_4^2 \ell^{2i\tilde{k}_3 \cdot \tilde{r}} + 2A_2 A_4 \ell^{i(\tilde{k}_1 + \tilde{k}_3) \cdot \tilde{r}}$$

and ΔE^* may be written out explicitly as $\Delta E^* = A_1^*(z) \ell^{i\tilde{k}_1 \cdot \tilde{r}} + A_3^*(z) \ell^{i\tilde{k}_3 \cdot \tilde{r}}$ thus

$$E_o^2 \Delta E^* = \{A_1^* A_2^2 \ell^{3i\tilde{k}_1 \cdot \tilde{r}} + A_3^* A_2^2 \ell^{i(2\tilde{k}_1 + \tilde{k}_3) \cdot \tilde{r}}$$

$$+ A_1^* A_4^2 \ell^{i(2\tilde{k}_3 + \tilde{k}_1) \cdot \tilde{r}} + A_3^* A_4^2 \ell^{3i\tilde{k}_3 \cdot \tilde{r}}$$

$$+ 2A_1^* A_2 A_4 \ell^{i(2\tilde{k}_1 + \tilde{k}_3) \cdot \tilde{r}} + 2A_3^* A_2 A_4 \ell^{i(2\tilde{k}_3 + \tilde{k}_1) \cdot \tilde{r}}\} .$$

Since none of these terms are synchronus with the left hand side of (IV-9), term (iii) is not phase matched.

Term (iv) may be explicitly written out as

$$- \frac{|E_o|^2 \Delta E}{(I_s + |E_o|^2)^2} = - (I_s + |E_o|^2)^{-2} \{(I_2 + I_4)\Delta E$$

$$+ A_1 A_2 A_4^* \ell^{-i\underset{\sim}{k}_3 \cdot \underset{\sim}{r}} + A_3 A_2^* A_4 \ell^{-i\underset{\sim}{k}_1 \cdot \underset{\sim}{r}}$$

$$+ [(A_2^* A_4 \ell^{-i(\underset{\sim}{k}_1 - \underset{\sim}{k}_3)\cdot \underset{\sim}{r}}) A_1 \ell^{-i\underset{\sim}{k}_1 \cdot \underset{\sim}{r}}]$$

$$+ [(A_2 A_4^* \ell^{i(\underset{\sim}{k}_1 - \underset{\sim}{k}_3)\cdot \underset{\sim}{r}}) A_3 \ell^{-i\underset{\sim}{k}_3 \cdot \underset{\sim}{r}}]\} .$$

The first three terms in this expression are obviously phase matched although they are modulated by $(I_s + |E_o|^2)^{-2}$.

The last 2 terms in square brackets must be looked at more closely. The fourth term is

$$- [\frac{(A_2^* A_4 \ell^{-i(\underset{\sim}{k}_1 - \underset{\sim}{k}_3)\cdot \underset{\sim}{r}})}{(I_s + |E_o|^2)^2}] A_1 \ell^{-i\underset{\sim}{k}_1 \cdot \underset{\sim}{r}}$$

The quantity above in the square bracket can be thought of as modulating the phase matched term $A_1 \ell^{-i\underset{\sim}{k}_1 \cdot \underset{\sim}{r}}$.

Notice that since the exponent in the square bracket above has the same fourier component as the oscillatory part of $|E_o|^2$, this term will not necessarily average to zero.

Similarly, the last term on the right hand side of the expression for

$$- \frac{|E_o|^2 \Delta E}{(I_s + |E_o|^2)^2}$$

is

$$- \left[\frac{(A_2 A_4^* \ell^{i(\underset{\sim}{k}_1 - \underset{\sim}{k}_3)\cdot\underset{\sim}{r}})}{(I_s + |E_o|^2)^2}\right] A_3 \ell^{-i\underset{\sim}{k}_3\cdot\underset{\sim}{r}} .$$

The quantity in this square bracket modulates the phase matched term $A_3 \ell^{-i\underset{\sim}{k}_3\cdot\underset{\sim}{r}}$, and the exponent in the square bracket has the same fourier component as the oscillatory portion of $|E_o|^2$, so this term also will not necessarily average to zero.

Equation (IV-9) may therefore be rewritten as

$$\left[\cos\theta \ell^{-i\underset{\sim}{k}_1\cdot\underset{\sim}{r}} \partial_z A_1(z) + \ell^{-i\underset{\sim}{k}_3\cdot\underset{\sim}{r}} \partial_z A_3(z)\right] =$$

$$\frac{\alpha_o |E_s|^2 (1-i\delta)}{(I_s + |E_o|^2)^2} \{(I_s + |E_o|^2)(A_1 \ell^{-i\underset{\sim}{k}_1\cdot\underset{\sim}{r}} + A_3 \ell^{-i\underset{\sim}{k}_3\cdot\underset{\sim}{r}})$$

$$- (I_2 + I_4)(A_1 \ell^{-i\underset{\sim}{k}_1\cdot\underset{\sim}{r}} + A_3 \ell^{-i\underset{\sim}{k}_3\cdot\underset{\sim}{r}}) \qquad \text{(IV-10)}$$

$$- A_1 A_2 A_4^* \ell^{-i\underset{\sim}{k}_3\cdot\underset{\sim}{r}} - A_3 A_2^* A_4 \ell^{-i\underset{\sim}{k}_1\cdot\underset{\sim}{r}}$$

$$- \zeta^* A_1 \ell^{-i\underset{\sim}{k}_1\cdot\underset{\sim}{r}} - \zeta A_3 \ell^{-i\underset{\sim}{k}_3\cdot\underset{\sim}{r}}\} .$$

The terms with $\ell^{-i\underset{\sim}{k}_1\cdot\underset{\sim}{r}}$ behavior are

$$\cos\theta\ \partial_z A_1(z) = \frac{\alpha_o |E_s|^2 (1-i\delta)}{(I_s + |E_o|^2)^2} \{[I_s + \zeta(z)] A_1(z) - A_2^* A_4 A_3(z)\}. \qquad \text{(IV-11)}$$

But the signal beam $A_3(z)$ will be much weaker than the probe beam $A_1(z)$, and since

$$\frac{|A_2^* A_4|}{|I_s+\zeta|} \leq 1,$$

one can neglect the last term in (IV-11) to obtain

$$\cos\theta\ \partial_z A_1(z) = \frac{\alpha_o |E_s|^2 (1-i\delta)}{(I_s + |E_o|^2)^2} \{(I_s + \zeta(z))A_1(z)\} \qquad \text{(IV-12)}$$

and the terms from (IV-10) with $\ell^{-i\underset{\sim}{k}_3 \cdot \underset{\sim}{r}}$ dependence are

$$\partial_z A_3(z) = \frac{\alpha_o |E_s|^2 (i-i\delta)}{(I_s + |E_o|^2)^2} \{(I_s + \zeta^*(z))A_3(z) - A_2 A_4^* A_1(z)\}. \qquad \text{(IV-13)}$$

Equations (IV-12) and (IV-13) describe the non-linear interactions in the media.

Along the z axis, $\zeta(z)$ and $\zeta^*(z)$ may be written

$$\zeta(z) = A_2 A_4^* \ell^{ik(1-\cos\theta)z}$$

$$\zeta^*(z) = A_2^* A_4 \ell^{-ik(1-\cos\theta)z} .$$

Now define phases ϕ_2 and ϕ_4 as

$$\phi_2 \equiv \arctan\left(\frac{\mathrm{Im}(A_2)}{\mathrm{Re}(A_2)}\right) \qquad \text{(IV-14)}$$

$$\phi_4 \equiv \arctan\left(\frac{\mathrm{Im}(A_4)}{\mathrm{Re}(A_4)}\right) \qquad \text{(IV-15)}$$

where $\mathrm{Re}(x) = \frac{x+x^*}{2}$, $\mathrm{Im}(x) = \frac{x-x^*}{2i}$; then

$$A_2 = |A_2| \ell^{i\phi_2}$$

$$A_4 = |A_4| e^{i\phi_4} .$$

The phase mismatch of the two pump beams Δ is given as $\Delta = \phi_2 - \phi_4$ and $\zeta(z)$ and $\zeta^*(z)$ become

$$\zeta(z) = |A_2 A_4| e^{i(k(1-\cos\theta)z+\Delta)} \qquad \text{(IV-16)}$$

$$\zeta^*(z) = |A_2 A_4| e^{-i(k(1-\cos\theta)z+\Delta)} . \qquad \text{(IV-17)}$$

The oscillatory behavior of $|E_o|^2$ can be shown more explicitly by defining the parameters

$$D_o \equiv I_s + I_2 + I_4$$

and

$$a \equiv |A_2 A_4| .$$

Equations (IV-12) and (IV-13) can then be expressed as

$$\partial_z A_3(z) = \alpha_o |E_s|^2 (1-i\delta) \left\{ \frac{\left[I_s + a e^{-i[k(1-\cos\theta)z+\Delta]}\right] A_3(z)}{\left[D_o + 2a\cos(k(1-\cos\theta)z+\Delta)\right]^2} - \frac{(a e^{i\Delta}) A_1(z)}{\left[D_o + 2a\cos(k(1-\cos\theta)z+\Delta)\right]^2} \right\} \qquad \text{(IV-18)}$$

$$\partial_z A_1(z) = \frac{\alpha_o |E_s|^2 (1-i\delta)}{\cos\theta} \left\{ \frac{\left[I_s + a e^{i[k(1-\cos\theta)z+\Delta]}\right] A_1(z)}{\left[D_o + 2a\cos(k(1-\cos\theta)z+\Delta)\right]^2} \right\} . \qquad \text{(IV-19)}$$

These equations can be simplified somewhat by defining β as

$$\beta = k(1-\cos\theta) \ .$$

Equations (IV-18) and (IV-19) may then be expressed as

$$\partial_z A_1(z) + P(z)A_1(z) = 0 \qquad \text{(IV-20)}$$

and

$$\partial_z A_3(z) + P(z)A_3(z) = Q(z) \qquad \text{(IV-21)}$$

where

$$P(z) = -\frac{\alpha_o |E_s|^2 (1-i\delta)}{\cos\theta} \left\{\frac{\left[I_s + a\ell^{i(\beta z+\Delta)}\right]}{\left[D_o+2a\cos(\beta z+\Delta)\right]^2}\right\} \qquad \text{(IV-22)}$$

and

$$P(z) = -\alpha_o |E_s|^2 (1-i\delta) \left\{\frac{I_s+a\ell^{-i(\beta z+\Delta)}}{\left[D_o+2a\cos(\beta z+\Delta)\right]^2}\right\} \qquad \text{(IV-23)}$$

and

$$Q(z) = -\frac{\alpha_o |E_s|^2 (1-i\delta) a\ell^{i\Delta} A_1(z)}{\left[D_o+2a\cos(\beta z+\Delta)\right]^2} \ . \qquad \text{(IV-24)}$$

The solutions to (IV-20) and (IV-21) fall into 2 categories, depending on whether or not $\zeta(z)$ and $\zeta^*(z)$ oscillate very rapidly over distances where $A_1(z)$ and $A_3(z)$ change appreciably.

Case I (θ is Not Small)

If θ is not small then $A_1(z)$ and $A_3(z)$ do not change appreciably over

$$\lambda_{os} = \frac{\lambda}{1-\cos\theta} .$$

Since for Case I $\zeta(z)$ and $\zeta^*(z)$ oscillate many times over distances where $A_1(z)$ and $A_3(z)$ change significantly, the quantities $P(z)$, $\mathcal{P}(z)$, and $Q(z)$ can be averaged over an oscillation wavelength λ_{os}.

$$\langle P(z)\rangle = -\frac{\alpha_o|E_s|^2(1-i\delta)}{\cos\theta}\left(\frac{1}{\lambda_{os}}\right)\int_o^{\lambda_{os}} dz\left\{\frac{I_s+a\cos\beta z+ia\sin\beta z}{(D_o+2a\cos\beta z)^2}\right\}$$

$$\langle P(z)\rangle = -\frac{\alpha_o|E_s|^2(1-i\delta)}{2\pi\cos\theta}\int_o^{2\pi} du\left\{\frac{I_s+a\cos u+ia\sin u}{(D_o+2a\cos u)^2}\right\}$$

$$\langle P(z)\rangle = -\frac{\alpha_o|E_s|^2(1-i\delta)}{\pi\cos\theta}\left\{I_s\int_o^{\pi}\frac{du}{(D_o+2a\cos u)^2} + a\int_o^{\pi}\frac{\cos u\,du}{(D_o+2a\cos u)^2}\right\}$$

$$\langle P(z)\rangle = -\frac{\alpha_o|E_s|^2(1-i\delta)}{\cos\theta}\left\{\frac{D_oI_s-2a^2}{(D_o^2-4a^2)^{3/2}}\right\} .$$

The complex absorption coefficient ξ can be defined as

$$\xi \equiv -\cos\theta\,\langle P(z)\rangle$$

or

$$\xi = \alpha_o|E_s|^2(1-i\delta)\left\{\frac{D_oI_s-2a^2}{(D_o^2-4a^2)^{3/2}}\right\} . \qquad \text{(IV-25)}$$

Equation (IV-20) can then be approximated as

$$\partial_z A_1(z) + \langle P(z)\rangle A_1(z) = 0$$

or

$$\partial_z A_1(z) - \xi \sec\theta \, A_1(z) = 0$$

which has solution

$$A_1(z) = A_1(L) \ell^{\xi \sec\theta (z-L)} \tag{IV-26}$$

where $A_1(L)$ is the incident probe beam amplitude.

One sees from comparing (IV-22) to (IV-23) that

$$\langle \mathcal{P}(z) \rangle = \cos\theta \langle P(z) \rangle$$

$$\langle \mathcal{P}(z) \rangle = - \xi \tag{IV-27}$$

and (IV-21) may be approximated as

$$\partial_z A_3(z) - \xi A_3(z) = \langle Q(z) \rangle . \tag{IV-28}$$

Remembering that $A_1(z)$ varies slowly over a distance λ_{os}, one can use (IV-24) to obtain

$$\langle Q(z) \rangle = - \alpha_o |E_s|^2 (1-i\delta) a \ell^{i\Delta} A_1(z) \langle (D_o + 2a\cos(\beta z + \Delta))^{-2} \rangle$$

$$\langle Q(z) \rangle = - \frac{\alpha_o |E_s|^2 (1-i\delta) a \ell^{i\Delta} A_1(z)}{\pi} \int_o^{\pi} (D_o + 2a\cos u)^{-2} du$$

$$\langle Q(z) \rangle = - \alpha_o |E_s|^2 (1-i\delta) a \ell^{i\Delta} A_1(z) \left\{ \frac{D_o}{(D_o^2 - 4a^2)^{3/2}} \right\} .$$

One can simplify (IV-28) by defining

$$\rho \equiv - \alpha_o |E_s|^2 (1-i\delta) a \ell^{i\Delta} \left\{ \frac{D_o}{(D_o^2 - 4a^2)^{3/2}} \right\}$$

so (IV-28) becomes

$$\partial_z A_3(z) - \xi A_3(z) = \rho A_1(L)\, \ell^{\xi \sec\theta (z-L)} \quad . \tag{IV-29}$$

Using the boundary condition that there is no incident signal beam, i.e., $A_3(0) = 0$, the solution to (IV-29) is

$$A_3(z) = \frac{\rho A_1(L)}{\xi(\sec\theta - 1)} \{\ell^{\xi \sec\theta (z-L)} - \ell^{\xi (z-L)}\} \quad . \tag{IV-30}$$

One quantity of interest is the signal beam intensity as it exists the media $|A_3(0)|^2$, since this is an experimentally measurable quantity.

$$|A_3(0)|^2 = |\rho/\xi|^2 \frac{|A_1(L)|^2}{(\sec\theta - 1)^2} \{\ell^{-2\xi_R L} + \ell^{-2\xi_R \sec\theta L} - 2\ell^{-\xi_R (1+\sec\theta) L} \cos[\xi_i (1-\sec\theta) L]\} \tag{IV-31}$$

where $\xi_R = \frac{\xi + \xi^*}{2}$, or

$$\xi_R = \frac{\alpha_o}{(1+\delta^2)} \left\{ \frac{(1 + \frac{I_2}{I_s} + \frac{I_4}{I_s}) - \frac{2I_2 I_4}{I_s^2}}{[(1 + \frac{I_2}{I_s} + \frac{I_4}{I_s})^2 - \frac{4I_2 I_4}{I_s^2}]^{3/2}} \right\} \tag{IV-32}$$

and

$$\xi_i = \frac{\xi - \xi^*}{2i} = -\delta \xi_R \tag{IV-33}$$

and

$$|\frac{\rho}{\xi}|^2 = \frac{D_o^2 a^2}{(D_o I_s - 2a^2)^2}$$

or

$$\left|\frac{\rho}{\xi}\right|^2 = \frac{\left(\frac{I_2 I_4}{I_s^2}\right)\left(1 + \frac{I_2}{I_s} + \frac{I_4}{I_s}\right)^2}{\left[\left(1 + \frac{I_2}{I_s} + \frac{I_4}{I_s}\right) - \frac{2I_2 I_4}{I_s^2}\right]^2} . \qquad \text{(IV-34)}$$

Thus (IV-31) may be written as

$$|A_3(0)|^2 = \left\{\frac{\left(\frac{I_2 I_4}{I_s^2}\right)\left(1 + \frac{I_2}{I_s} + \frac{I_4}{I_s}\right)^2}{\left[\left(1 + \frac{I_2}{I_s} + \frac{I_4}{I_s}\right) - \frac{2I_2 I_4}{I_s^2}\right]^2}\right\} \times \left(\frac{|A_1(L)|^2}{(\sec\theta - 1)^2}\right) \qquad \text{(IV-35)}$$

$$\times \left\{\ell^{-2\xi_R L} + \ell^{-2\xi_R \sec\theta L} - 2\ell^{-\xi_R(1+\sec\theta)L} \cos[\xi_i(1-\sec\theta)L]\right\}$$

where ξ_R and ξ_i are given explicitly by (IV-32) and (IV-33). Normally in a degenerate FWM experiment the two pump beams and the probe beam are obtained by splitting one laser beam into three parts. When this is the case, one sees from (IV-35) that the output Bragg diffracted signal beam intensity will vary as the cube of the laser power.

A good measure of the "scattering efficiency" η of the four wave mixing process is the ratio of the exiting signal beam $|A_3(0)|^2$ to the exiting probe beam in the absence of the pump beam interactions.

Using (IV-25) and (IV-26), one obtains

$$|A_1(0)|^2\big|_{E_o=0} = |A_1(L)|^2 \, \ell^{-\left(\frac{2\alpha_o}{1+\delta^2}\right)L} .$$

So the scattering efficiency η is given by

$$\eta = \left\{ \frac{(\frac{I_2 I_4}{I_s^2})(1 + \frac{I_2}{I_s} + \frac{I_4}{I_s})^2}{[(1 + \frac{I_2}{I_s} + \frac{I_4}{I_s}) - \frac{2I_2 I_4}{I_s^2}]^2} \right\} \left[\frac{\frac{2\alpha_o L}{\ell^{1+\delta^2}}}{(\sec\theta - 1)^2} \right] \left\{ \ell^{-2\xi_R L} + \ell^{-2\xi_R \sec\theta L} \right.$$

$$\left. - 2\ell^{-\xi_R(1+\sec\theta)L} \cos[\xi_i(1-\sec\theta)L] \right\} . \qquad \text{(IV-36)}$$

The dependence of the scattering efficiency η on crossing angle θ can be clarified somewhat whenever $|\xi L(1-\sec\theta)|$ is small.

This will usually be true since the experiment does not work well if:

(i) $|\xi L|$ is large since if $|\xi L|$ is large the beams are essentially extinguished in the crystal.

(ii) θ is very large since the output Bragg diffracted signal beam intensity decreases with increasing θ.

Thus if $|\xi L(1-\sec\theta)|$ is small, then to first order in $|\xi L(1-\sec\theta)|$, (IV-36) becomes

$$\eta = |\rho|^2 L^2 \ell^{-2\xi_R L} \frac{2\alpha_o L}{\ell^{1+\delta^2}} (1 + \xi_R L(1-\sec\theta)) \qquad \text{(IV-37)}$$

where

$$|\rho|^2 = (\frac{\alpha_o^2 I_s^2}{1+\delta^2}) \{\frac{a^2 D_o^2}{(D_o^2 - 4a^2)^3}\}$$

or

$$|\rho|^2 = \frac{\alpha_o^2}{1+\delta^2} \left\{ \frac{\left(\frac{I_2 I_4}{I_s^2}\right)\left(1 + \frac{I_2+I_4}{I_s}\right)^2}{\left[\left(1 + \frac{I_2+I_4}{I_s}\right)^2 - \frac{4 I_2 I_4}{I_s^2}\right]^3} \right\} .$$

Equation (IV-37) shows that the scattering efficiency η decreases with increasing crossing angle θ.*

It is now of interest to calculate the scattering efficiency η when the pump intensity is well below saturation intensity, i.e., when $\left|\frac{I_1 + I_2}{I_s}\right| << 1$.

Assuming that $\left|\frac{I_2 + I_4}{I_s}\right| << 1$, then to first order in $\frac{(I_2 - I_4)}{I_s}$, $|\rho|^2$ and ξ_R become

$$|\rho|^2 = \frac{\alpha_o^2}{1+\delta^2} \left(\frac{I_2 I_4}{I_s^2}\right)\left(1 - \frac{4(I_2+I_4)}{I_s}\right)$$

and

$$\xi_R = \frac{\alpha_o}{1+\delta^2} \left(1 - 2\,\frac{(I_2 + I_4)}{I_s}\right)$$

so that (IV-37) becomes

$$\eta = \left\{\left(\frac{\alpha_o^2 L^2}{1+\delta^2}\right)\left(\frac{I_2 I_4}{I_s^2}\right)\left[1 + \frac{4(I_2+I_4)}{I_s}\left(\frac{\alpha_o L}{1+\delta^2} - 1\right)\right]\right. \qquad \text{(IV-38)}$$

---

*In thick samples, there will be another effect that will decrease the output signal intensity with increasing crossing angle θ. In thick samples, as θ is increased, the beam overlap volume in the sample may decrease, which is not taken into account in this development.

$$x \left[1 + \frac{\alpha_o L}{1+\delta^2}\left(1 - \frac{2(I_2+I_4)}{I_s}\right)\right.$$

$$\left. x \quad (1-\sec\theta)\right]\}. \qquad \text{(IV-38)}$$

To lowest order in $\frac{(I_2 + I_4)}{I_s}$, (IV-38) becomes

$$\eta_{\substack{\text{well below} \\ \text{saturation}}} = \frac{\alpha_o^2 L^2}{1+\delta^2}\left(\frac{I_2 I_4}{I_s^2}\right)\left(1 + \frac{\alpha_o L}{1+\delta^2}(1-\sec\theta)\right) . \qquad \text{(IV-39)}$$

Experimentally, one usually works with crossing angles large enough that Case I applies and Equation (IV-36), (IV-37), or (IV-39) will be applicable. However, it is of interest to derive the scattering efficiency for very small angles in certain limiting cases to discover what new effects should be expected at very small crossing angles.

Case II (θ is Small)

If θ is very small, then $A_1(z)$ and $A_3(z)$ do change appreciably over $\lambda_{os} = \frac{\lambda}{1-\cos\theta}$; and thus $P(z)$, $\bar{P}(z)$, and $Q(z)$ cannot be averaged over λ_{os}.

Equations (IV-20) and (IV-21) cannot be solved for exactly in this case, since $P(z)$, $\bar{P}(z)$, and $Q(z)$ cannot be averaged.

Equations (IV-20) and (IV-21) will be approximately solved for in the case where the pump beams are well below saturation intensity, i.e., for the case that $\frac{a}{I_s}$ is small.

One can now define α as

$$\alpha = \frac{\alpha_o(1-i\delta)}{(1+\delta^2)}\left(1 + \frac{I_2 + I_4}{I_s}\right)^{-2}$$

and to first order in $\frac{a}{I_s}$; (IV-22) becomes

$$P(z) = -\alpha\{1 - \frac{3a}{I_s}\cos(\beta z+\Delta) + \frac{ia}{I_s}\sin(\beta z+\Delta)\} . \qquad \text{(IV-40)}$$

The solution to Equation (IV-20) is then

$$A_1(z) = C_1 \exp\{\alpha z - \frac{3a}{\beta I_s}\sin(\beta z+\Delta) - \frac{ia}{\beta I_s}\cos(\beta z+\Delta)\} \qquad \text{(IV-41)}$$

C_1 is a constant which is determined from boundary conditions to be given by

$$C_1 = A_1(L) \exp\{-\alpha[L - \frac{3a}{\beta I_s}\sin(\beta L+\Delta) - \frac{ia}{\beta I_s}\cos(\beta L+\Delta)]\} . \qquad \text{(IV-42)}$$

Equation (IV-41) then becomes

$$A_1(z) = A_1(L) \exp\{\alpha(z-L) - \frac{2\alpha a}{\beta I_s}[3\sin(\frac{\beta(z-L)}{2})\cos(\frac{\beta(z+L)}{2} + \Delta) - i\sin(\frac{\beta(z+L)}{2} + \Delta)\sin(\frac{\beta(z-L)}{2})]\} . \qquad \text{(IV-43)}$$

To first order in a/I_s, Equation (IV-24) becomes

$$Q(z) = -\alpha \ell^{i\Delta}(\frac{a}{I_s})A_1(z)(1 - \frac{4a}{I_s}\cos(\beta z+\Delta)) \qquad \text{(IV-44)}$$

and since $|A_3(z)| << |A_1(z)|$, $P(z)$ may be approximated as $P(z) \approx -\alpha$ so that Equation (IV-21) may be approximated as

$$\partial_z A_3(z) - \alpha A_3(z) = Q(z) \qquad \text{(IV-45)}$$

with solution

$$A_3(z) = \ell^{\alpha z}(C_2 + \int Q(z)\ell^{-\alpha z}dz)$$

or

$$A_3(z) = C_2\ell^{\alpha z} - \frac{\alpha\ell^{i\Delta}\ell^{\alpha z}aC_1}{I_s}\int dz\{(1 - \frac{4a}{I_s}\cos(\beta z+\Delta))$$

$$x \quad \exp[-\frac{\alpha a}{\beta I_s}(3\sin(\beta z+\Delta)+i\cos(\beta z+\Delta))]\} \qquad \text{(IV-46)}$$

where C_1 is given by (IV-42) and C_2 is a constant that remains to be determined using boundary conditions.

To perform the integration indicated in Equation (IV-46), one needs to expand the exponent inside the integral in powers of a/I_s. Since the factor a/I_s in the exponent is multiplied by a factor of α/β, it is important to briefly examine magnitude of $|\alpha/\beta|$ to be sure that it is not large. This parameter can be rewritten as

$$\frac{\alpha}{\beta} = \frac{\alpha L}{\beta L} = \frac{\alpha L}{k(1-\cos\theta)L}.$$

The beams are approximately attenuated as $\ell^{-\alpha L}$ as they pass through the crystal, so $|\alpha L|$ must be of order unity or smaller or else the beams are so severely attenuated through the crystal that the Bragg diffracted signal beam will be negligible.

Furthermore, $|k(1-\cos\theta)L|$ will be ≥ 1 for typical sample dimensions unless than angle is too small to be experimentally realizable.

Thus taking $|\alpha/\beta| \lesssim 1$ will be a good assumption for almost any meaningful experimental configuration.

Expanding the exponent inside the integral from Equation (IV-46) and keeping terms first order in a/I_s, (IV-46) becomes

$$A_3(z) = C_2 \ell^{\alpha z} - \frac{\alpha \ell^{i\Delta} \ell^{\alpha z} a C_1}{I_s} \int dz \{1 - \frac{3a\alpha}{\beta I_s} \sin(\beta z+\Delta)$$

$$- \frac{a}{I_s} (4 + \frac{i\alpha}{\beta}) \cos(\beta z+\Delta) \}. \qquad \text{(IV-47)}$$

Performing the integration, this becomes

$$A_3(z) = C_2 \ell^{\alpha z} - \frac{\alpha \ell^{i\Delta} \ell^{\alpha z} a C_1}{I_s} \{z + \frac{3a\alpha}{\beta^2 I_s} \cos(\beta z+\Delta) - \frac{a}{\beta I_s} (4 + \frac{i\alpha}{\beta}) \sin(\beta z+\Delta) \}. \qquad \text{(IV-48)}$$

One can use the boundary condition $A_3(L) = 0$ to obtain

$$C_2 = \frac{\alpha \ell^{i\Delta} a C_1}{I_s} \left[L + \frac{3a\alpha}{\beta^2 I_s} \cos(\beta L+\Delta) - \frac{a}{\beta I_s} (4 + \frac{i\alpha}{\beta}) \sin(\beta L+\Delta) \right] . \qquad \text{(IV-49)}$$

One can then substitute (IV-49) into (IV-48) to obtain

$$A_3(z) = \frac{\alpha a C_1 \ell^{i\Delta} \ell^{\alpha z}}{I_s} \{(L-z) - \frac{6a\alpha}{\beta^2 I_s} \left[\sin(\frac{\beta(L+z)}{2} + \Delta) \sin(\frac{\beta(L-z)}{2}) \right]$$

$$- \frac{2a}{\beta I_s} (4 + \frac{i\alpha}{\beta}) \left[\sin(\frac{\beta(L-z)}{2}) \cos(\frac{\beta(L+z)}{2} + \Delta) \right] \} . \qquad \text{(IV-50)}$$

One can expand (IV-42) to first order in a/I_s to obtain

$$C_1 = A_1(L) \ell^{-\alpha L} \{1 + \frac{a\alpha}{\beta I_s} \left[3\sin(\beta L+\Delta) + i\cos(\beta L+\Delta) \right] \} \qquad \text{(IV-51)}$$

One can now substitute (IV-51) into (IV-50) to obtain to first order in a/I_s

$$A_3(z) = \frac{\alpha a A_1(L) \ell^{i\Delta} \ell^{\alpha(z-L)}}{I_s} \{(L-z) \left[1 + \frac{a\alpha}{\beta I_s} (3\sin(\beta L+\Delta) + i\cos(\beta L+\Delta)) \right] \qquad \text{(IV-52)}$$

$$- \frac{6a\alpha}{\beta^2 I_s}\left[\sin\left(\frac{\beta(L+z)}{2} + \Delta\right)\sin\left(\frac{\beta(L-z)}{2}\right)\right] \qquad \text{(IV-52)}$$

$$- \frac{2a}{\beta I_s}\left(4 + \frac{i\alpha}{\beta}\right)\left[\sin\left(\frac{\beta(L-z)}{2}\right)\cos\left(\frac{\beta(L+z)}{2} + \Delta\right)\right]\} \ .$$

At the output face z = o,

$$A_3(O) = \frac{\alpha a A_1(L)\ell^{i\Delta}\ell^{-\alpha L}}{I_s}\{L + \frac{a\alpha L}{\beta I_s}(3\sin(\beta L+\Delta) + i\cos(\beta L+\Delta)) - \frac{6a\alpha}{\beta^2 I_s}$$

$$x\ \left[\sin\left(\frac{\beta L}{2} + \Delta\right)\ x\ \sin\left(\frac{\beta L}{2}\right)\right] - \frac{2a}{\beta I_s}\left(4 + \frac{i\alpha}{\beta}\right)\sin\left(\frac{\beta L}{2}\right)\cos\left(\frac{\beta L}{2} + \Delta\right)]\} \ . \qquad \text{(IV-53)}$$

The output intensity of the Bragg scattered signal beam will be equal to $|A_3(O)|^2$, and to first order in $|a/I_s|$, this is given by

$$|A_3(O)|^2 = L|\alpha|^2\left(\frac{I_2 I_4}{I_s^2}\right)|A_1(L)|^2\ell^{-2\alpha_R L}\{L + \frac{2aL}{\beta I_s}[3\alpha_R \sin(\beta L+\Delta) - \alpha_i\cos(\beta L+\Delta)]$$

$$- \frac{12a\alpha_R}{\beta^2 I_s}\sin\left(\frac{\beta L}{2} + \Delta\right)\sin\left(\frac{\beta L}{2}\right) \qquad \text{(IV-54)}$$

$$- \frac{4a}{\beta I_s}\left(4 - \frac{\alpha_i}{\beta}\right)\left[\sin\left(\frac{\beta L}{2}\right)\cos\left(\frac{\beta L}{2} + \Delta\right)\right]\}$$

where

$$\alpha_R = \frac{\alpha+\alpha^*}{2} = \left(\frac{\alpha_o}{1+\delta^2}\right)\left(1 + \frac{I_2 + I_4}{I_s}\right)^{-2}$$

and

$$\alpha_i = \frac{\alpha-\alpha^*}{2i} = -\delta\alpha_R \ .$$

Equation (IV-54) is the expression for the output Bragg scattered signal beam to first order in $\frac{|A_2A_4|}{I_s}$ for CASE II (small angles).

Examining this result more closely, one can see from Equation (IV-54) that all of the terms in (IV-54) that are first order in $\frac{|A_2A_4|}{I_s}$ all vary sinusoidally with the phase mismatch Δ of the two pump beams.

If the 2 pump beams are within the coherence length of each other, then the phase mismatch Δ will be given by

$$\Delta = (\frac{2\pi}{\lambda})(\Delta L)$$

where ΔL is the difference in path length between the two pump beams. Thus the component of $|A_3(O)|^2$ which is first order in $\frac{|A_2A_4|}{I_s}$ will be exceptionally sensitive to vibration and to the precise alignment of the pump beams. Thus at very small angles, Equation (IV-54) predicts the observed Bragg scattered signal beam to have a component that oscillates very rapidly due to vibrations or minor adjustments superimposed on an "envelope signal" that is insensitive to vibrations and precise alignments.

Remembering that the "scattering efficiency" η of the four wave mixing process is the ratio of the exiting signal beam $|A_3(O)|^2$ to the exiting probe beam in the absence of the pump interactions $|A_1(O)|^2|_{E_o=O}$, one obtains from (IV-43) that

$$|A_1(O)|^2|_{E_o=O} = |A_1(L)|^2 \, \ell^{-\frac{2\alpha_o L}{1+\delta^2}} .$$

Using (IV-54), the scattering efficiency η for the small angles of CASE II to first order in $|A_2A_4|/I_s$ is

$$\eta = L|\alpha|^2 \left(\frac{I_2 I_4}{I_s^2}\right) \ell^{\frac{2\alpha_o L}{1+\delta^2}} \ell^{-2\alpha_R L} \{L + \frac{2aL}{\beta I_s}[3\alpha_R \sin(\beta L+\Delta) - \alpha_i \cos(\beta L+\Delta)]$$

(IV-55)

$$- \frac{12a\alpha_R}{\beta^2 I_s} \sin(\frac{\beta L}{2} + \Delta)\sin(\frac{\beta L}{2}) - \frac{4a}{\beta I_s}(4 - \frac{\alpha_i}{\beta})[\sin(\frac{\beta L}{2})\cos(\frac{\beta L}{2} + \Delta)\} .$$

Transient Behavior

When the pump beams are chopped, two processes can contribute to the decay of the sinusoidal excited state population grating. The grating can decay because of the decrease in the excited state population by normal fluorescence decay and because of exciton migration from the peak to the valley regions of the grating. Whenever the exciton motion is diffusive, the density of excited states is given by (36)

$$\partial_t n(x,t) = D\, \partial_x^2 n(x,t) - \frac{n(x,t)}{\tau} \qquad \text{(IV-56)}$$

where x is along the direction of the grating wavevector, D is the diffusion coefficient, and τ is the fluorescence decay time. If it is assumed that n(x,t) initially has a sinusoidal spatial distribution, the solution to (IV-56) is

$$n(x,t) = \frac{\ell^{-t/\tau}}{2}\{1 + \ell^{-k_g^2 Dt}\cos(kgx)\} \qquad \text{(IV-57)}$$

where k_g is the magnitude of the grating wavevector. The depth of the grating Δn is given by

$$\Delta n = n(x=0,t) - n(x = \frac{\Lambda}{2},t) = \ell^{-\frac{K}{2}t} \qquad \text{(IV-58)}$$

where K is the decay constant given by

$$K = 2(k_g^2 D + \frac{1}{\tau}) \quad . \tag{IV-59}$$

The magnitude of the grating wavevector k_g is given by

$$k_g = \frac{2\pi}{\Lambda} = \pi/\sin(\theta/2) \quad .$$

For small θ, k_g may be approximated as

$$k_g \approx \frac{2\pi}{\theta} \quad .$$

Since the scattering efficiency is proportional to Δn (43), the Bragg scattered signal beam intensity $I_s(t)$ may be written as

$$I_s(t) \propto I_p [I_w \Delta n]^2$$

or

$$I_s(t) \propto I_p I_w^2 \ell^{-Kt} \tag{IV-60}$$

where I_p is the incident probe beam intensity and I_w is the pump beam intensity. Thus the Bragg diffracted signal beam should decay exponentially with decay constant

$$K = 2(\frac{\pi^2}{\sin^2(\frac{\theta}{2})} D + \frac{1}{\tau}) \tag{IV-61}$$

which for small angles becomes

$$K = \frac{2}{\tau} + \frac{8\pi^2}{\theta^2} D \quad . \tag{IV-62}$$

Data and Interpretation

The experimental configuration used is as shown in Figure IV-3. The 5145Å line of an argon laser is used because it falls on the edge of one of the Nd^{3+} absorption bands.

The laser beam is sent through a one meter focal length lens and is then split into three beams. The weak probe beam (beam 3 in Figure IV-3) is split off using a variable beam splitter. The two pump beams (beams 1 and 2 in Figure IV-3) are split off using a 50-50 beam splitter. The path lengths of the pump beams 1 and 2 must be the same within the coherence length, but the probe beam 3 path length is purposely made much different to discourage gratings formed from the interference of the probe beam with one of the pump beams.

The probe beam 3 is aligned counterpropagating to the pump beam 2. The probe beam then Bragg diffracts off of the holographic grating in the sample so that the Bragg diffracted signal beam (beam 4 in Figure IV-3) counterpropagates back along the pump beam 1. This signal beam is then picked off using a beam splitter, and is directed into a photomultiplier tube.

To analyze the transient behavior of the grating decay, one then chops the pump beams and then observes the decay of the Bragg scattered signal beam 4 using a boxcar integrator and x-y recorder.

The samples studied using this technique were $Nd_xLa_{1-x}P_5O_{14}$ at room temperature where $x = 0.2$, $x = 0.6$, and $x = 1.0$.

The most stable data were obtained for crossing angle $\theta \gtrsim 2^\circ$, because of the small angle instabilities predicted by Equation (IV-54). The signal was found to have two components. One component was exceptionally sensitive to vibrations and to the exact alignment of the

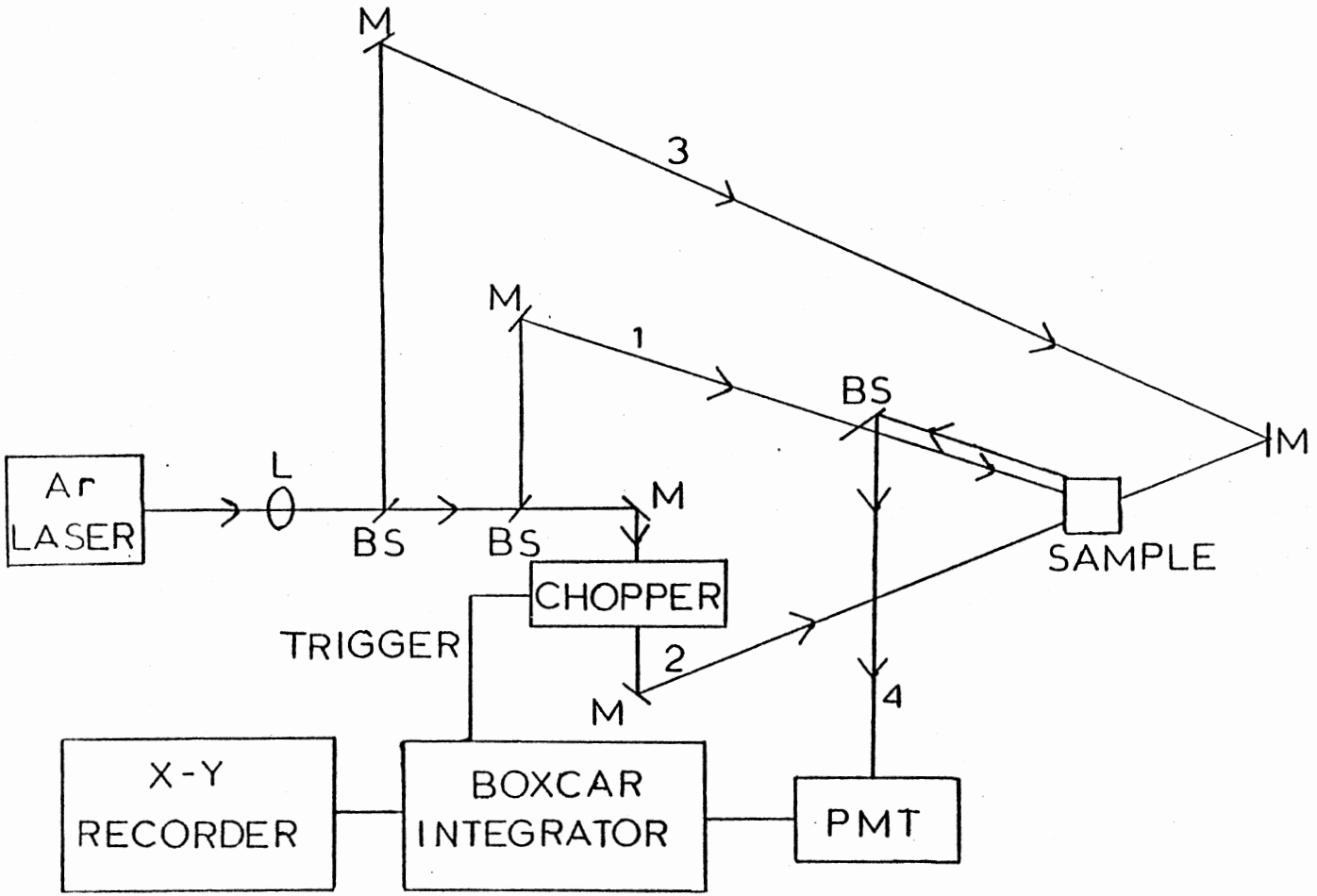

Figure IV-3. Four Wave Mixing Experimental Configuration. Beams 1 and 2 are the Pump Beams, Beam 3 is the Probe Beam, and Beam 4 is the Bragg Diffracted Signal Beam

experiment, and underwent many oscillations whenever slight alignment changes were made. This component was superimposed on another much stabler component. This type of behavior is explained directly following Equation (IV-54) on page 79.

Experimentally, in all three samples, double exponential decay was observed. The fast decay component had a decay constant K that was independent of θ^2 and did not extrapolate to twice the fluorescence decay rate, contrary to the predictions of Equation (IV-62). This shows that the fast decay component is due to scattering off a complex index of refraction grating due to an optical Kerr effect which does not result from excited state absorption. It is not particularly surprising that other mechanisms create an optical Kerr effect in a birefringent, ferroelastic crystal such as $Nd_xLa_{1-x}P_5O_{14}$, and these mechanisms will be studied more closely in future experiments where the sample will be taken to low temperatures.

However, the slower component of the double exponential decay had a decay constant K that followed the predictions of Equation (IV-62) very closely and thus could be identified as an excited state population grating. It is the decay constant K of this slower component that will be focused on here.

The decay constant K versus θ is given in Table IV-I and K versus θ^2 is plotted in Figure IV-4. With each sample, it is seen that the decay constant K varies linearly with θ^2 as is predicted by Equation (IV-62), and in each case the decay constant extrapolates nicely to twice the fluorescence decay rate (shown by the shaded points) as θ^2 approaches zero which also agrees with Equation (IV-62). The fluorescence decay times are explicitly listed in Table IV-III.

By calculating the slope of the theoretical fit to the data (shown

TABLE IV-1

GRATING DECAY CONSTANT VS. PUMP BEAM CROSSING ANGLE FOR $Nd_xLa_{1-x}P_5O_{14}$

x	θ	K(Sec.)
0.2	1°	6759
0.2	5°	6868
0.2	8.7°	7194
0.2	9.4°	7227
0.2	12°	7429
0.6	3°	11765
0.6	5°	12101
0.6	7.9°	12953
1.0	2°	15949
1.0	7.3°	18215
1.0	8.7°	19531

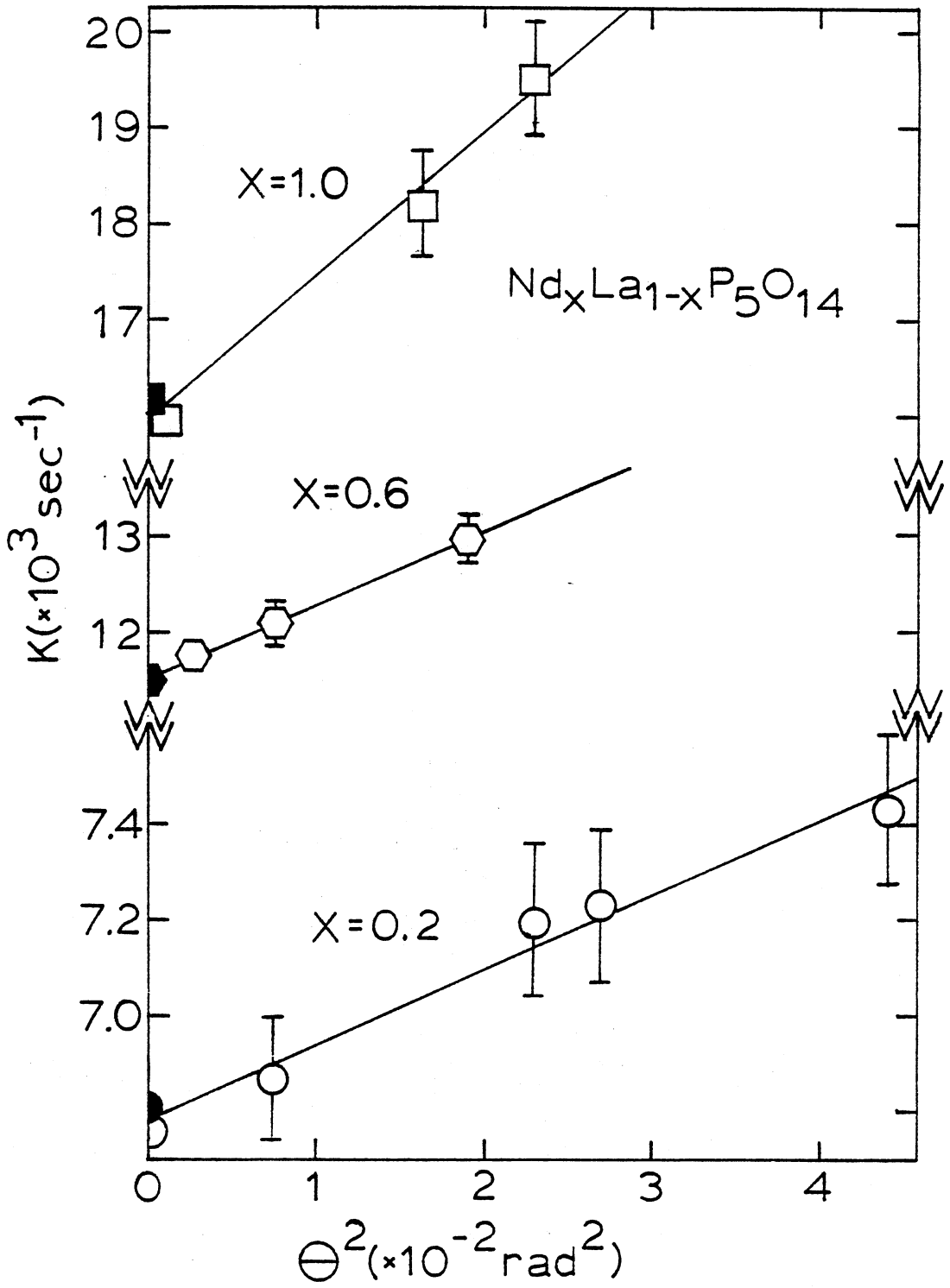

Figure IV-4. Decay Constant Vs. θ^2. The Rectangles are for NdP_5O_{14}, the Hexagons are for $Nd_{.6}La_{.4}P_5O_{14}$, and the Circles are for $Nd_{.2}La_{.8}P_5O_{14}$. The Respective Shaded Points are Double the Fluorescence Decay Rate for Each Sample

by the solid lines in Figure IV-4) one can directly calculate the diffusion constant D using Equation (IV-62). Table IV-II lists the calculated diffusion constants for the three samples. These diffusion constants are for energy migration approximately along the crystallographic a direction. It was much more difficult to take data along other crystallographic directions, but in the $Nd_{.2}La_{.8}P_5O_{14}$ sample (which gave the best data) the diffusion constant along the crystallographic b direction was found to be the same as along the crystallographic a direction within experimental error.

TABLE IV-II

CONCENTRATION DEPENDENCE OF THE DIFFUSION PARAMETERS

$Nd_xLa_{1-x}P_5O_{14}$			
X	τ(μs)	$D(\frac{cm^2}{sec})$	L_x(μm)
0.2	294	5.2×10^{-7}	0.18
0.6	174	2.5×10^{-6}	0.30
1.0	124	5.1×10^{-6}	0.36

The exciton migration length L_x is defined as the average distance an exciton travels before fluorescence decay occurs, and can be approximated as

$$L_x = \sqrt{2D\tau} \ .$$

The values for this exciton migration length are listed in Table IV-II.

An important part of understanding energy migration in these crystals is identifying the microscopic nature of the interaction causing the exciton migration. To identify this interaction, one needs to identify the concentration dependence of the diffusion constant.

The diffusion constant for an exciton undergoing an incoherent random walk resulting from an electric dipole-dipole interaction can be approximated as (1)

$$D = [\frac{1}{2}(\frac{4\pi}{3} N_{so})^{4/3} \frac{R_o^6}{\tau_o}]X^{4/3} \qquad \text{(IV-64)}$$

where R_o is the critical interaction distance, τ_o is the intrinsic fluorescence lifetime of the Nd ion, N_{so} is the sensitizer concentration for NdP_5O_{14}, and X is the normalized sensitizer concentration (X = 1 for NdP_5O_{14}).

Figure IV-5 shows a plot of D versus $X^{4/3}$. It can be seen from Figure IV-5 that the diffusion constant D varies linearly with $X^{4/3}$, showing that the microscopic interaction responsible for the exciton migration is an electric dipole-dipole interaction. Using τ_o = 350 μs and $N_{so} = 4 \times 10^{21}$ cm^{-3}, by calculating the slope of the theoretical fit to the data (shown as the solid line in Figure IV-5), one obtains from Equation (IV-64) that $R_o = 45\text{Å}$. This electric dipole-dipole interaction has sufficiently long range to overcome any anisotropy in the crystal, which explains why the diffusion constant is the same along the crystallographic a and b directions.

Now that the existence of long range energy diffusion in $Nd_xLa_{1-x}P_5O_{14}$ has been demonstrated, to obtain more information about the

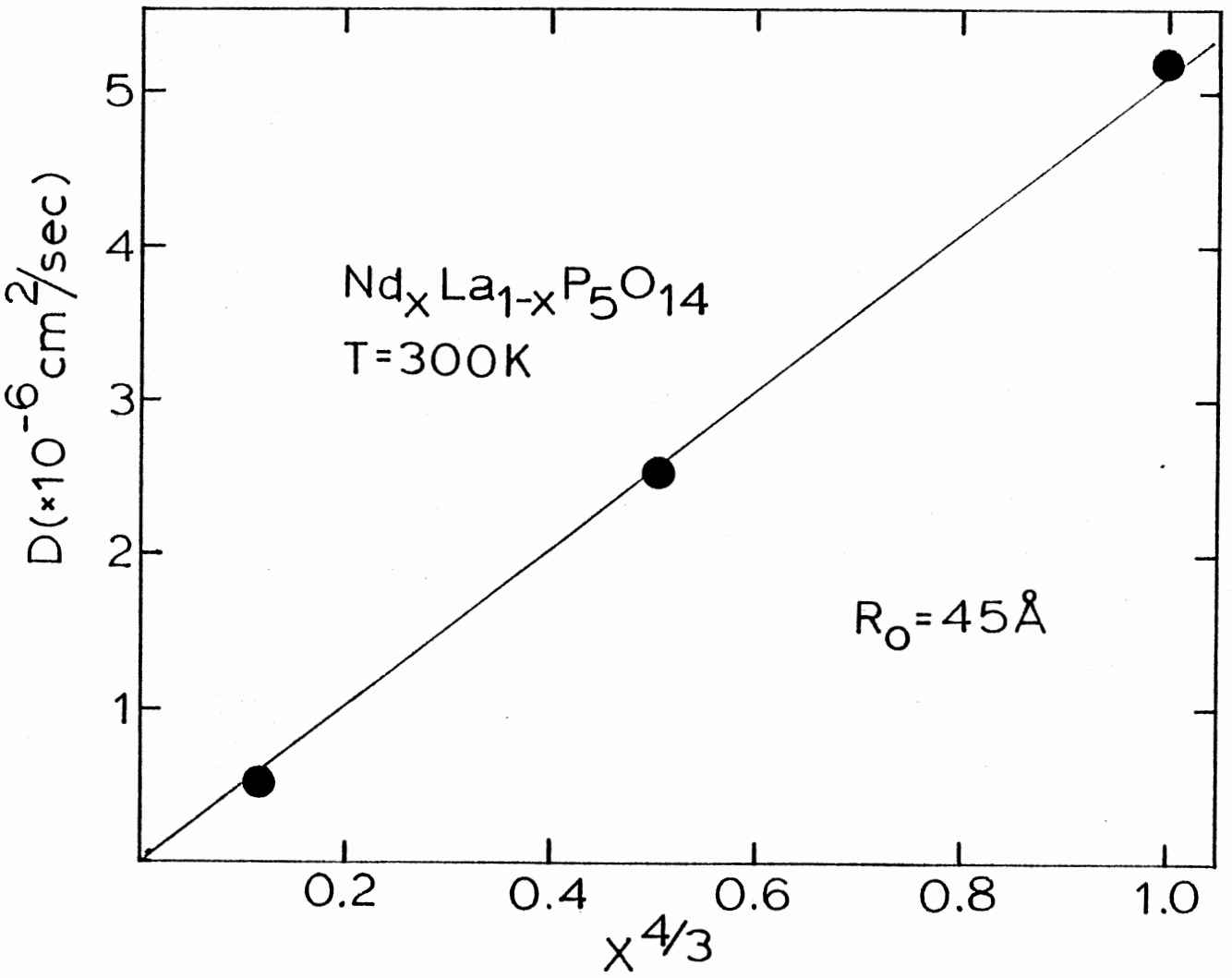

Figure IV-5. Concentration Dependence of the Diffusion Constant

quenching one needs to look at the concentration dependence of the quenching rate W_Q, which is given by

$$W_Q = (\tau)^{-1} - (\tau_o)^{-1} \qquad \text{(IV-65)}$$

where τ is the fluorescence decay time and τ_o is again the intrinsic fluorescence lifetime of the Nd ion.

Again taking τ_o = 350 μs, the fluorescence lifetime τ and quenching rate W_Q versus concentration are listed in Table IV-III and are plotted in Figure IV-6.

TABLE IV-III

FLUORESCENCE LIFETIMES AND QUENCHING RATES VS. CONCENTRATION FOR $Nd_xLa_{1-x}P_5O_{14}$

X	τ(μs)	$W_Q(sec^{-1})$
0.01	333.5	141
0.1	320.5	263
0.2	293.7	548
0.6	174.1	2887
1.0	123.9	5214

At high concentrations, the quenching rate varies linearly with concentration as is shown in Figure IV-6. This linear dependence of quenching rate with concentration, together with the very long exciton migration lengths shown in Table IV-I, demonstrate that the dominant quenching mechanism in the higher concentration $Nd_xLa_{1-x}P_5O_{14}$ crystals (and most importantly in NdP_5O_{14}) is an exciton diffusion and trapping mechanism.

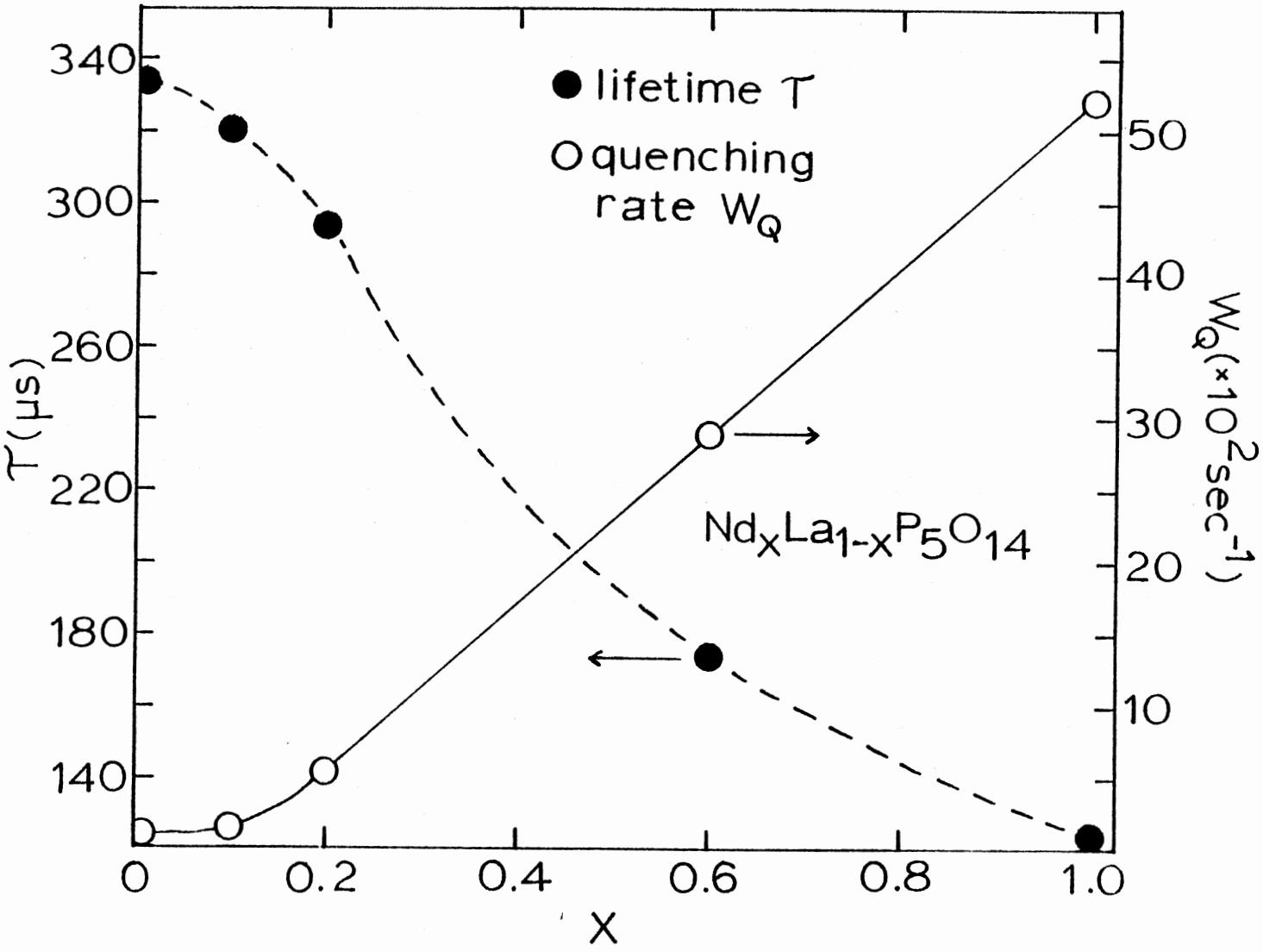

Figure IV-6. Concentration Dependence of Fluorescence Lifetime and Quenching Rate

At low concentrations, the quenching rate no longer varied linearly with concentration as can be seen in Figure IV-6.

In Figure IV-7, the quenching rate is plotted vs. concentration (empty circles) and the square of the concentration (shaded circles) for the three samples with lowest concentration. It is seen that for these low concentration samples, the quenching rate varies approximately quadratically with concentration, which is consistent with an ion-pair cross relaxation quenching mechanism.

Thus to summarize, at high concentrations the dominant quenching mechanism is clearly exciton diffusion to traps, and at low concentrations the data is more consistent with a ion-pair cross relaxation quenching mechanism.

This is consistent with the interpretation of the quenching mechanisms at high and low concentrations in materials such as $Nd_xLa_{1-x}Cl_3$ (44).

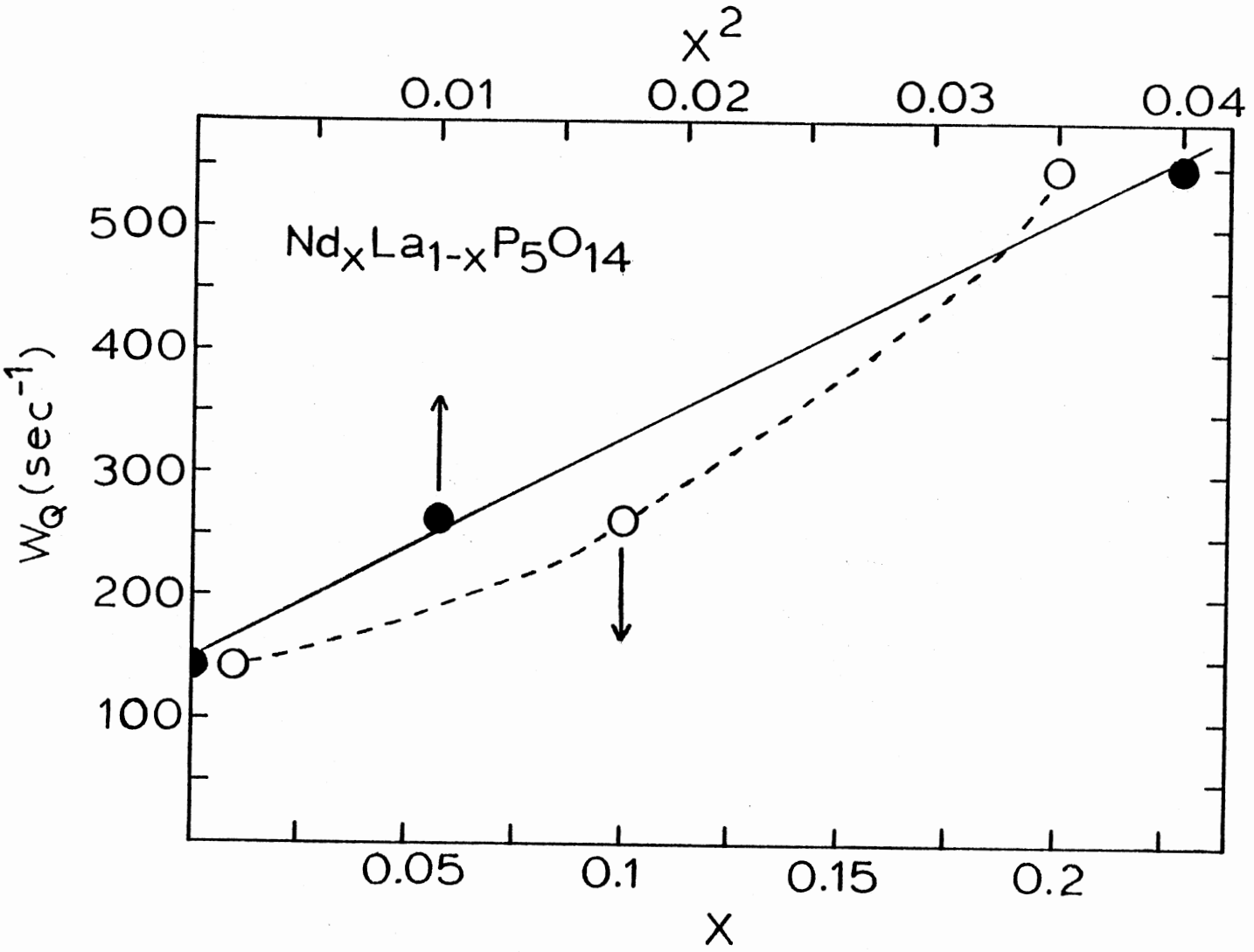

Figure IV-7. Concentration Dependence of Quenching Rate. Empty Circles Show W_Q Vs. X and Shaded Circles Show W_Q Vs. X^2

CHAPTER V

SUMMARY AND CONCLUSIONS

In Chapter II it was shown that when choosing the appropriate energy transfer model for a given situation, one needs to carefully consider the limits of applicability for each model as derived in Chapter II. For a given model to be valid, not only must this model give a good fit to data, but the fitting parameters obtained from this fit must be consistent with the assumptions made in deriving the model.

The Yokota-Tanimota theory is valid whenever there is a uniform lattice of sensitizers and whenever the sensitizer-sensitizer interaction is small compared to the sensitizer-activator interaction. These were found to be invalid assumptions in the systems of interest.

The Chow-Powell theory is valid for a uniform lattice of sensitizers whenever the sensitizer-sensitizer interaction is large compared to the sensitizer-activator interaction. These were found to be valid assumptions for the $Y_{.84}Yb_{.1}Ho_{.06}F_3$ system, and thus the Chow-Powell theory best characterizes this system.

The Soos-Powell theory assumes a uniform distribution of sensitizers and accounts for direct sensitizer-activator interaction through the concept of activator induced host trapping regions, and is especially useful in dealing with activators of large size where the point trapping approximation is not valid. The Soos-Powell theory was found to be the appropriate theory for characterizing Anthracene in Fluorene.

The Burshtein theory indirectly assumes a uniform distribution of

sensitizers (through the assumption of an average hopping time), and is most important in the intermediate region where neither the Chow-Powell theory nor the Yokota-Tanimoto theory is valid since there is some problem in the interpretation of the relevant physical fitting parameters of the Burshtein theory. The Burshtein theory was found to be the appropriate theory for characterizing $Tb_3Al_5O_{14}$.

In systems such as $Y_3Ga_5O_{12}:Nd^{3+}$ (0.25%) and $YVO_4:Nd^{3+}$(3%) where the sensitizers are a low concentration impurity, the uniform lattice approximation is invalid and these systems were found to be more appropriately modeled using a numerical Monte Carlo simulation. The Monte Carlo model gives significantly different results than a model that assumes a uniform distribution of sensitizers such as the Burshtein model. The Monte Carlo technique described in Chapter II has the advantage of correctly accounting for the ability of the exciton to interact with all other ions in the lattice at each step in the random walk. This technique also does not require large computer core, so it can be inexpensively run on a small lab computer such as the LSI-11. However, this technique does not distinguish between excitons on initially excited sites and all other sites, which is important in interpreting fluorescence line-narrowing data. Analyzing line-narrowing data requires more conventional Monte Carlo techniques that generate specific lattice geometries; but these techniques only consider first or second nearest neighbor interactions and they require enormous computer core requiring expensive run time on large computers.

Important information in future theoretical work could be obtained by specifically considering the distribution of active ions on a lattice through the lattice parameters.

The site selection spectroscopy work on $LiNbO_3:Eu^{3+}$ showed that

energy transfer occurs between the sensitizer and the activator transitions. This energy transfer can be modeled as being due to a constant transfer rate between two transitions pumped by exponentially decaying pumping functions. The constant energy transfer rate was found to be due to energy transfer between sensitizer-activator pairs at a fixed distance apart.

The FWM work in Chapter IV describes the first observation of energy diffusion in an inorganic material using FWM techniques. At room temperature, the diffusion was found to be long range with an average exciton migration length of 0.36 microns in NdP_5O_{14}. The microscopic interaction causing this diffusion was found to be an electric dipole-dipole interaction, with a critical interaction distance $R_o = 45\text{Å}$. The concentration quenching mechanism in the $Nd_xLa_{1-x}P_5O_{14}$ samples was found to be dominated by an exciton diffusion and trapping mechanism at high concentrations (most importantly in the pure NdP_5O_{14} sample). At low concentrations, the data was more consistent with an ion-ion cross relaxation quenching mechanism.

The steady-state FWM scattering efficiency was also derived in Chapter IV for the configuration of interest, by modeling the medium as a two-level system. This yielded information about the mechanisms responsible for the formation of the grating, what parameters are important in the FWM process, and how the FWM scattering efficiency depends on these parameters. Furthermore, the existence of instabilities when the pump beam crossing angle is small was theoretically explained.

Because of the demonstration of long range energy diffusion in $Nd_xLa_{1-x}P_5O_{14}$, the next important step is to extend these experiments to low temperatures to search for the existence of coherent exciton motion.

REFERENCES

1. Förster, T., Ann. Physik 2, 55 (1948); Z. Naturforsch 49, 321 (1949).

2. Dexter, D. L., J. Chem. Phys. 21, 836 (1953).

3. Inokuti, M., Hirayama, F., J. Chem. Phys. 43, 1978 (1965).

4. Förster, T., Ann. Phys. 2, 55 (1948).

5. Trlifaj, M., Chzech. J. Phys. 5, 463 (1955); 6, 533 (1956); 8, 510 (1958).

6. Chandrasekhar, S., Rev. Mod. Phys. 15, 1 (1943).

7. Knox, R. S., Theory of Excitons, Academic Press, New York, 1963.

8. Burshtein, A. I., Sov. Phys. JETP 35, 882 (1972).

9. Spitzer, F., Principles of Random Walk, Van Nostrand, Princeton, 1964; Rosenstock, H. B., SIAM J. Applied Math. 9, 169 (1961); Rudemo, R., SIAM J. Appl. Math. 14, 1293 (1966); Montroll, E. W., Weiss, G. H., J. Math. Phys. 2, 167 (1965).

10. Soos, Z. G., Powell, R. C., Phys. Rev. B 6, 4035 (1972).

11. Yokota, M., Tanimoto, O., J. Phys. Soc. Japan 22, 779 (1967).

12. Chow, H. C., Powell, R. C., Phys. Rev. B 21, 3785 (1980).

13. Merkle, L. D., Doctoral Dissertation, Department of Physics, Oklahoma State University, 1978.

14. Watts, R. K. and H. J. Richter, Phys. Rev. B 6, 1584 (1972).

15. Powell, R. C., J. Luminescence 6, 285 (1973); R. C. Powell and W. D. Trumbly, Physics Letters 57A, 87 (1976).

16. Van der Ziel, J. P., L. Kopf, and L. G. Van Uitert, Phys. Rev. B 6, 615 (1972).

17. Watts, R. K., J. Chem. Phys. 64, 902 (1976).

18. Lyo, S. K., J. Phys. C 12, L83 (1979).

19. Knuth, D. E., The Art of Computer Programming, Vol. 2, (Addison-Wesley, Mass., 1969), p. 30.

20. Merkle, L. D. and R. C. Powell, Phys. Rev. B 20, 75 (1979).

21. Sardar, D. and R. C. Powell, J. Appl. Phys. 51, 2829 (1980).

22. Holstein, T., S. K. Lyo, and R. Orbach, Phys. Rev. Lett. 36, 891 (1976).

23. Powell, Richard C. and Edwin E. Freed, J. Chem. Phys. 70, (10), 4681, May, 1979.

24. Weber, M. J., 'Handbook of Lasers', R. J. Pressley, Editor, Chemical Rubber Co., 1971, pp. 371-417.

25. Weber, H. P., Opt. Quantum Electron 7, 431 (1975).

26. Plättner, R. D., W. W. Krühler, W. K. Zwicker, T. Kovats, and S. R. Chinn, J. Crystal Growth 49, 274 (1980).

27. Singh, S., D. C. Miller, J. R. Potopowicz, and L. K. Shick, J. Appl. Phys. 46, 1191 (1975).

28. Strek, W., C. Szafranski, E. Lukowiak, Z. Mazurak, and B. Jerowska-Trzebiatowska, Phys. Stat. Sol. A 41, 547 (1977).

29. Tofield, B. C., H. P. Weber, T. C. Damen, and P. F. Liao, J. Solid State Chem. 12, 207 (1975).

30. Blätte, M., H. G. Danielmeyer, and R. Ulrich, Appl. Phys. 1, 275 (1973).

31. Liao, P. F., H. P. Weber, and B. C. Tofield, Solid State Comm. 16, 881 (1973).

32. Flaherty, J. M. and R. C. Powell, Phys. Rev. B 19, 32 (1979).

33. Auzel, F., D. Meichenin, and J. C. Michel, J. Luminescence 18/19, 97 (1979).

34. Nettel, S. J., and A. Lempicki, Optics Comm. 30, 387 (1979).

35. Huber, G., J. P. Jeser, W. W. Krühler, and H. G. Danielmeyer, IEEE J. Quant. Elect. QE-10, 766 (1974).

36. Salcedo, J. R., A. E. Siegman, D. D. Dlott, and M. D. Fayer, Phys. Rev. Letters 41, 131 (1978).

37. Eichler, H. J., J. Eichler, J. Knof, and Ch. Noack, Phys. Stat. Sol. (a) 52, 481 (1979).

38. Hamilton, D. S., D. Heiman, J. Feinberg, and R. W. Hellwarth, Optics Letters 4, 124 (1979).

39. Liao, P. F., L. M. Humphrey, D. M. Bloom, and S. Geschwind, Phys. Rev. B 20, 4145 (1979); P. F. Liao and D. M. Bloom, Optics Letters 3, 4 (1978).

40. Yariv, A. and D. M. Pepper, Opt. Lett. 1, 16 (1977).

41. Abrams, R. L., and R. C. Lind., Opt. Lett. 2, 94 (1978); R. L. Abrams and R. C. Lind., Opt. Lett. 3, 205 (1978).

42. Liao, P. F. and D. M. Bloom, Opt. Lett. 3, 4 (1978).

43. Siegman, A. E., J. Opt. Soc. Am., 67, 545 (1977).

44. Voron'ko, Yu. K., et al., Sov. Phys. JETP 44, 251 (1976).

45. Chinn, S. R., H. Y-P. Hong, and J. W. Pierce, Laser Focus 12, 64 (1976).

46. Danielmeyer, H. G. and H. P. Weber, IEEE J. Quantum Electron 8, 805 (1972).

47. Danielmeyer, H. G., Festkörperprobleme 15, 253 (1975).

48. Lempicki, A., Opt. Commun. 23, 376 (1977).

49. Merkle, Larry D., Ian L. Spain, and Richard C. Powell, J. Phys. C: Solid State Phys., 14, (1981), 2027-2038.

50. Danielmeyer, H. G., J. Lumin. 12/13, 179 (1976).

51. Auzel, F., IEEE J. Quantum Elect. 12, 258 (1976).

52. Flaherty, J. M., R. C. Powell, Solid State Comm. 26, 503 (1978); Flaherty, J. M., Powell, R. C., Phys. Rev. B 19, 32 (1979); Powell, R. C., et al., J. Phys. Chem. Solids 41, 345 (1980).

53. Kogelnik, Herwig, The Bell System Technical Journal, Vol. 48, No. 9, 2909 (1969).

APPENDIX

DERIVATION OF SUSCEPTIBILITY χ FOR A TWO LEVEL MEDIA*

Consider an absorbing media which will be modeled as an array of two level atoms that can be characterized by dipole moment μ and longitudinal and transverse relaxation times t_1 and t_2, respectively. One can then derive the susceptibility χ, where $\underset{\sim}{P} = \varepsilon_o \chi(\underset{\sim}{E})\underset{\sim}{E}$.

Suppose that a quantum mechanical system is in state $\psi(\underset{\sim}{r},t)$. One can expand $\psi(\underset{\sim}{r},t)$ as $\psi(\underset{\sim}{r},t) = \sum_n C_n(t)U_n(\underset{\sim}{r})$ where $U_n(\underset{\sim}{r})$ are a complete orthonormal set of functions and $C_n(t)$ is the n^{th} time dependent expansion coefficient. An operator A has expectation value

$$\langle A \rangle = \sum_{nm} C^*_m A_{mn} C_n$$

where $A_{mn} = (U_m, AU_n)$.

The ensemble average $\overline{\langle A \rangle}$ is given by $\overline{\langle A \rangle} = \sum_{mn} \rho_{mn} A_{mn}$ where $\rho_{mn} = \overline{C^*_m C_n}$ or

$$\overline{\langle A \rangle} = \sum_n (\rho A)_{nn} = Tr(\rho A) . \qquad (A\text{-}1)$$

Now consider an ensemble of two-level atoms interacting with a time-harmonic electromagnetic field. The density matrix is a 2x2 matrix

---

*See A. Yariv, Quantum Electronics (Wiley, New York, 1975).

with elements ρ_{11}, ρ_{22}, ρ_{12}, $\rho_{21} = \rho_{12}^*$. The interaction hamiltonian $H'(t)$ is of the dipole type, and can be written as $H'(t) = -\mu E(t)$. Since the dipole transitions are between states of definite parity, $\mu_{11} = \mu_{22} = 0$; and the phases of $U_1(\underset{\sim}{r})$ and $U_2(\underset{\sim}{r})$ can be chosen such that $\mu_{22} = \mu_{21} = \mu$. One can then write the interaction hamiltonian as

$$H'(t) = \begin{pmatrix} 0 & -\mu E(t) \\ -\mu E(t) & 0 \end{pmatrix} .$$

The unperturbed hamiltonian H_o is given by

$$H_o = \begin{pmatrix} \varepsilon_1 & 0 \\ 0 & \varepsilon_2 \end{pmatrix}$$

where ε_2 is the energy of the excited state and ε_1 is the energy of the ground state.

Thus the hamiltonian H is given by

$$H = \begin{pmatrix} \varepsilon_1 & -\mu E(t) \\ -\mu E(t) & \varepsilon_2 \end{pmatrix} . \qquad \text{(A-2)}$$

The ensemble average $\overline{\langle\mu\rangle}$ of the dipole moment induced by $E(t)$ is given by

$$\overline{\langle\mu\rangle} = \mathrm{Tr}(\rho\mu) = \mu(\rho_{12}+\rho_{21}) = \mu(\rho_{21}+\rho_{21}^*) . \qquad \text{(A-3)}$$

The density matrix satisfies

$$\frac{d\rho}{dt} = \frac{-i}{\hbar}[H,\rho] . \qquad \text{(A-4)}$$

which becomes

$$\frac{d\rho}{dt} = \frac{-i}{\hbar}\begin{pmatrix} \mu E(t)(\rho_{21}-\rho_{21}^*) & -\mu E(t)(\rho_{22}-\rho_{11})-(\varepsilon_2-\varepsilon_1)\rho_{21}^* \\ \mu E(t)(\rho_{22}-\rho_{11})+(\varepsilon_2-\varepsilon_1)\rho_{21} & \mu E(t)(\rho_{21}-\rho_{21}^*) \end{pmatrix} . \quad \text{(A-5)}$$

Defining the resonant frequency $\omega_o = \frac{\varepsilon_2-\varepsilon_1}{\hbar}$, it follows from (A-5) that

$$\frac{d\rho_{21}}{dt} = -i\omega_o\rho_{21} + \frac{i\mu}{\hbar} E(t)(\rho_{11}-\rho_{22}) \quad \text{(A-6)}$$

$$\frac{d\rho_{22}}{dt} = \frac{i\mu E(t)}{\hbar} (\rho_{21}-\rho_{21}^*) \quad \text{(A-7)}$$

and using the normalization condition,

$$\frac{d}{dt} (\rho_{11}-\rho_{22}) = \frac{2i\mu}{\hbar} E(t)(\rho_{21}-\rho_{21}^*) . \quad \text{(A-8)}$$

The above equations of motion for the density matrix do not include collisional effects. When the perturbing field E(t) is turned off, one expects the off diagonal terms in the density matrix to vanish as the relative phase coherence among the eigenfunctions of the ensemble is lost via collisions. These collisions will conserve the average energy of each level, but cause a loss of information about the phases of the wavefunctions. The jth diagonal element of the density matrix represents the fraction of the systems in the ensemble that will give the answer E_j when the energy is measured. If one takes into account only collisions, these will be given by the Boltzmann factors, and the equilibrium density matrix ρ^{ℓ} is

$$\rho^{\ell} = \frac{1}{Q}\begin{pmatrix} \ell^{-\varepsilon_1/k_bT} & 0 \\ 0 & \ell^{-\varepsilon_2/k_bT)} \end{pmatrix}$$

where Q = partition function = $\ell^{-\varepsilon_1/k_bT} + \ell^{-\varepsilon_2/k_bT}$.

If the perturbing field is turned off, the density matrices will decay back to equilibrium with decay constant t^{-1} as

$$\frac{d\rho_{jk}}{dt} = -\frac{(\rho_{jk} - \rho^{\ell}_{jk})}{t_{jk}},$$

Because of the normalization condition, for a two-level system the relaxation times of the diagonal elements must be equal and is called the longitudinal relaxation time t_1. Since $\rho_{12} = \rho^*_{21}$, the off diagonal relaxation times are also equal and is called the transverse relaxation time t_2. The transverse relaxation time can be thought of as a phase coherence relaxation time.

After including collisional effects, (A-6) and (A-8) become

$$\frac{d\rho_{21}}{dt} = -i\omega_o\rho_{21} + \frac{i\mu}{\hbar}(\rho_{11}-\rho_{22})E(t) - \frac{\rho_{21}}{t_2} \qquad \text{(A-9)}$$

$$\frac{d}{dt}(\rho_{11}-\rho_{22}) = \frac{2i\mu E(t)}{\hbar}(\rho_{21}-\rho^*_{21}) - \frac{(\rho_{11}-\rho_{22}) - (\rho^{\ell}_{11}-\rho^{\ell}_{22})}{t_1}. \qquad \text{(A-10)}$$

If one assumes that the local perturbing field $E(t)$ is harmonic, $E(t) = E_o\cos\omega t$; then if $\omega \approx \omega_o$ the slowly varying variable $\sigma_{21}(t)$ may be defined as

$$\rho_{21}(t) = \sigma_{21}(t)\ell^{-i\omega t}. \qquad \text{(A-11)}$$

Substituting into (A-9), and throwing out the nonsynchronous term $\ell^{i\omega t}$ which averages to zero, Equation (A-9) becomes

$$\frac{d\sigma_{21}}{dt} = i(\omega-\omega_o)\sigma_{21} + \frac{i\mu E_o}{2\hbar}(\rho_{11}-\rho_{22}) - \frac{\sigma_{21}}{t_2} . \qquad \text{(A-12)}$$

Substituting (A-11) into (A-10) and throwing out the nonsynchronous terms $\ell^{2i\omega t}$ and $\ell^{-2i\omega t}$ which average to zero, one obtains

$$\frac{d}{dt}(\rho_{11}-\rho_{22}) = \frac{i\mu E_o}{\hbar}(\sigma_{21}-\sigma_{21}^*) - \frac{(\rho_{11}-\rho_{22}) - (\rho_{11}-\rho_{22})^{\ell}}{t_1} . \qquad \text{(A-13)}$$

To obtain the steady state solutions to the density matrix, the left hand side of (A-12) and (A-13) is set equal to zero. The precession frequency Ω is defined as

$$\Omega = \frac{\mu E_o}{2\hbar}$$

and the steady-state solutions to (A-12) and (A-13) are

$$\mathrm{Re}(\sigma_{21}) = \frac{-\Omega t_2^2(\rho_{11}-\rho_{22})^{\ell}(\omega-\omega_o)}{1 + 4\Omega^2 t_1 t_2 + t_2^2(\omega-\omega_o)^2} \qquad \text{(A-14)}$$

$$\mathrm{Im}(\sigma_{21}) = \frac{\Omega t_2(\rho_{11}-\rho_{22})^{\ell}}{1 + 4\Omega^2 t_1 t_2 + t_2^2(\omega-\omega_o)^2} \qquad \text{(A-15)}$$

$$\rho_{11}-\rho_{22} = (\rho_{11}-\rho_{22})^{\ell}\left\{\frac{1 + (\omega-\omega_o)^2 t_2^2}{1 + (\omega-\omega_o)^2 t_2^2 + 4\Omega^2 t_2 t_1}\right\} . \qquad \text{(A-16)}$$

If N is the density of active atoms or ions, then $\Delta N = N(\rho_{11}-\rho_{22})$ is the average density of the population difference between the two levels,

and $\Delta N^{\ell} = N(\rho_{11}-\rho_{22})^{\ell}$ is the population difference between the two levels at zero field. From (A-16),

$$\Delta N = \Delta N^{\ell} \{\frac{1 + (\omega-\omega_o)^2 t_2^2}{1 + (\omega-\omega_o)^2 t_2^2 + 4\Omega^2 t_2 t_1}\} .$$

The macroscopic polarization P is given by

$$P = N\overline{<\mu>} \quad \text{or, using (A-3),}$$

$P = N\mu(\rho_{21} + \rho_{21}^*)$ which can be expressed in terms of σ_{21} as

$$P = 2N\mu(\mathrm{Re}(\sigma_{21})\cos\omega t + \mathrm{Im}(\sigma_{21})\sin\omega t) .$$

Substituting in for $\mathrm{Re}(\sigma_{21})$ and $\mathrm{Im}(\sigma_{21})$, one may write the polarization as

$$P = \frac{\mu^2 \Delta N^{\ell} t_2}{\hbar} E_o [\frac{\sin\omega t + (\omega_o-\omega) t_2 \cos\omega t}{1 + (\omega-\omega_o)^2 t_2^2 + 4\Omega^2 t_2 t_1}] . \qquad \text{(A-17)}$$

One may now express the polarization in terms of the susceptibility χ as

$$P(t) = \varepsilon_o(\mathrm{Re}(\chi))E_o\cos\omega t - \varepsilon_o(\mathrm{Im}(\chi))E_o \sin\omega t ;$$

comparing with (A-17), it can be seen from observation that

$$\mathrm{Re}(\chi) = \frac{\mu^2 t_2 \Delta N^{\ell}}{\varepsilon_o \hbar} \{\frac{(\omega_o-\omega) t_2}{1 + (\omega-\omega_o)^2 t_2^2 + 4\Omega^2 t_1 t_2}\} \qquad \text{(A-18)}$$

and

$$\mathrm{Im}(\chi) = -\frac{\mu^2 t_2 \Delta N^{\ell}}{\varepsilon_o \hbar} \left\{ \frac{1}{1 + (\omega-\omega_o)^2 + 4\Omega^2 t_1 t_2} \right\} . \qquad \text{(A-19)}$$

Now let k be the magnitude of the wavevector at frequency ω. One can identify $\delta = (\omega-\omega_o)t_2$ as the normalized detuning from line center; $|E_s|^2 = \frac{\hbar^2}{t_1 t_2 \mu^2}$ as the line center saturation "intensity"; and $\alpha_o = \frac{\mu^2 \Delta N^{\ell} t_2 k}{2\varepsilon_o \hbar}$ as the line center small-signal field attenuation coefficient.

Using (A-18) and (A-19), one may write the two-level atom susceptibility χ as

$$\chi(E) = -\frac{2\alpha_o}{k} \frac{(i+\delta)}{(1 + \delta^2 + \frac{|\tilde{E}|^2}{|E_s|^2})} . \qquad \text{(A-20)}$$

VITA

Christopher Mark Lawson

Candidate for the Degree of

Doctor of Philosophy

Thesis: STUDIES OF SPECTRAL AND SPATIAL ENERGY TRANSFER IN SOLIDS

Major Field: Physics

Biographical:

Personal Data: Born in Tulsa, Oklahoma, April 4, 1954, the son of Oliver Roy and Wanda June Lawson. Married to Jean F. Lawson, with one child, Kristen M. Lawson.

Education: Graduated from Edison High School in Tulsa, Oklahoma, in May, 1972; received Bachelor of Science degree from Oklahoma State University in May, 1976; received Master of Science degree from University of Colorado, Boulder, Colorado, in May, 1979; completed requirements for the Doctor of Philosophy degree at Oklahoma State University in December, 1981.

Professional Experience: Graduate Teaching Assistant, Department of Physics, Purdue University, 1976-1977; Graduate Teaching Assistant, Department of Physics, University of Colorado, 1977-1978; Research Assistant, National Center for Atmospheric Research, 1978-1979; Research Assistant, Department of Physics, Oklahoma State University, 1979-1981; Lecturer, Physics Department, Oklahoma State University, 1981-1982.